Understanding and Development of Combined Acoustic and Magnetic Actuation of Ni_2MnGa Single Crystals

by

Ratchatee Techapiesancharoenkij

B.S. Materials Science and Engineering
Northwestern University, 2001
M.S. Materials Science and Engineering
Massachusetts Institute of Technology, 2004

Submitted to the Department of Materials Science and Engineering
in partial fulfillment of the requirements for the degree of

Doctor of Philosophy in Materials Science and Engineering

at the

MASSACHUSETTS INSTITUTE OF TECHNOLOGY

September 2007

Author ……...
Department of Materials Science and Engineering
July 30, 2007

Certified by ……...
Samuel M. Allen
POSCO Professor of Physical Metallurgy
Thesis Supervisor

Certified by ……...
Robert C. O'Handley
Senior Research Scientist
Thesis Supervisor

Accepted by ……..
Samuel M. Allen
POSCO Professor of Physical Metallurgy
Chairman, Departmental Committee on Graduate Students

Understanding and Development of Combined Acoustic and Magnetic Actuation of Ni_2MnGa Single Crystals

by

Ratchatee Techapiesancharoenkij

Submitted to the Department of Materials Science and Engineering
on July 30, 2007, in partial fulfillment of the requirements of the degree of
Doctor of Philosophy in Materials Science and Engineering

Abstract

Ni–Mn–Ga based ferromagnetic shape memory alloys (FSMAs) have emerged as a promising new class of active materials capable of producing a large (several %) magnetic-field-induced strain (MFIS). FSMAs still have several characteristic shortcomings that may limit their potential applications. A threshold field of 2 to 4 kOe must be overcome to initiate twin boundary motion and a larger field is required to achieve full actuation. The operating window of the stress output from FSMA actuators is narrow and limited to the range between 0.5 and 2 MPa. Outside the operating range, the strain output diminishes significantly. This thesis addresses these limitations and reports potential techniques to decrease the required threshold field and increase the stress and strain output of FSMA actuation.

The demagnetizing field due to magnetic poles on the surface of the sample is found to significantly influence the maximum field needed for full MFIS. The demagnetizing field decreases the effective internal field inside the FSMA sample; as a result, for a given external field, the magnetic driving force is reduced by the demagnetizing field. For a small demagnetization factor, full MFIS can be achieved at a field as low as 0.5 kOe. However, for a high demagnetization factor, full MFIS may require a field as high as 3.5 kOe. A phenomenological free energy model with an approximate magnetostatic term included properly describes this.

The application of an acoustic assist from a 33-mode piezoelectric stack is shown to improve MFIS of Ni-Mn-Ga single crystals by reducing the required threshold field and twinning-yield stress. Threshold field reductions of up to 1 kOe are observed, and the twinning-yield stress is reduced by up to 0.5 MPa. The piezo assist on FSMA actuation can be understood as a form of time varying stress waves that facilitate twin boundary motion. The stress-wave theory and FEM analyses, based on assumption of an elastic and isotropic material, are used to estimate the amplitude of stress waves. The stress values determined from the wave theory and FEM are comparable to the observed reduction in twinning-yield stress (0.6 to 2 MPa). The empirical stress wave amplitude is generally lower than the calculated one, because the actual stress waves generated in FSMA are limited by inelastic and anisotropic nature of the FSMA samples.

For FSMA samples with twin planes oriented 45^o to the elongation axis, longitudinal stress waves parallel to the elongation axis are the most effective type to facilitate twin boundary motion. Longitudinal stress waves impart uniaxial tensile/compressive stresses into the sample normal to its base, resulting in the maximum shear stresses along the 45^o twin planes. On the contrary, the transverse stress waves are the least effective type, because the resulting shear stresses along the twin planes are equal to zero. This is confirmed by the comparison of the effectiveness of the piezo-assist using the longitudinal 33-mode and transverse 15-mode piezo stacks. The maximum reduction of twinning-yield stress of 0.5 MPa is observed with the longitudinal piezo assist, while a maximum twinning stress reduction of only 0.05 MPa can be achieved by the transverse piezo assist.

For FSMA cyclic actuation, both operating stress and strain outputs of the FSMA actuation are significantly enhanced by the piezo-assisted effect. Without the piezo-assistance, the maximum reversible strain of the sample used here is 3% and appears only in the limited external stress range between 0.7 and 1 MPa. With the piezo-assistance, the maximum reversible strain increases to 4.5% and appears in a broader range of stress output between 0.4 and 1.2 MPa. The reduction in the twinning-yield stress due to the acoustic-assistance obviously improves the FSMA cyclic actuation performance; any magnetic energy not used to drive twin boundary motion can potentially be utilized to work against a larger external stress.

The magnetic stresses for a given magnetic field, calculated from the free energy model, appear to be larger than the empirical ones. The demagnetization effect is shown to be responsible for much of the deviation. The demagnetization effect reduces the internal field needed to move twin boundary and do external work.

Thesis Supervisor: Samuel M. Allen
Title: POSCO Professor of Physical Metallurgy

Thesis Supervisor: Robert C. O'Handley
Title: Senior Research Scientist

Acknowledgements

Throughout the course of my graduate study, I owe a great debt of gratitude to several people who provided me several kinds of assistances.

I would first like to thank my co-advisors, Samuel M. Allen and Robert C. O'Handley for their guidance and support. I first met Sam during the DMSE visiting weekend and he made me feel very welcome right away, which made my decision easier to come to MIT. Since then, he continued to embrace me with his kind and understanding manner throughout the years at MIT. Shortly after I completed my M.S. thesis under his supervision, he introduced me to Bob who was also an amazingly nice person. Bob's enthusiastic and innovative approach to supervision motivated me to enjoy both scientific and technological aspects of this work. The stories through his personal experiences, which he passed on during our occasional lunch, were also interesting and inspiring for a young researcher like me.

Many thanks to my thesis committee members, Yet-Ming Chiang and Krystyn Van Vliet for sparing their time and providing useful suggestions to make this thesis better.

My colleagues in the magnetic materials group graciously provided me various kinds of supports. My experimental data would not exist without the magical expertise of David Bono, the electronics wizard of DMSE. Bradly Peterson, Jorge Feutchwanger and Joshua Chambers helped me to become familiar with the lab, FSMAs, electronics, machining, etc. Jesse Simon for his resourceful insights on stress waves and piezoelectrics. Marc Richard, who was my first office mate at MIT, was also helpful with his expertise in materials characterizations, X-Ray diffraction and TEM analysis. Hiromasa Yabe and his wife for their Japanese-style courtesy and yummy dinner. Jari Kostamo, a visiting student from Finland, is my other electronic wizard whose expertise in electronics, Labview, and machining helped to expedite my last set of experimental work.

My UROP students, Christalee Bieber and Chun Li, should also be acknowledged for helping me to take some of the data in this thesis.

Technical staffs at MIT were also important to this work. Thanks to Xinlin Xie for helping me to prepare samples for heat treatment. Fred Cote, Mark Belanger and Anthony Calogero at the Edgerton student shop for kindly teaching me how to operate milling machines and being patient with my clumsiness. I can proudly see myself as not only a research scientist but also an engineer who can (somewhat) machine tools himself.

This work would not be successful without assistance from administrative staffs. Thanks to Jazy Ma, Bob's assistance, for her responsibilities on all the purchasing and paperwork errands. DMSE administrative officers, Kathleen Farrell, Angelita Mireles and Stephanie Bright, for their hard work to make sure that I would not miss any important deadlines.

My DMSE friends were always helpful and provided me several useful advices and assistance. Thanks to Nok, Lek, Albert, and Preston for keeping me a company during the first year; our productivity during study group, lunch/dinner break were sure a big reason all of us survived the core courses and the written exam. P'Kob, P'Jess,

P'Naan for all of their helps and preparing me for the oral qualification exams. N'Puye for helps on this thesis especially introducing me to EndNote©, N'Vee for interesting discussion on metallurgy during our gym time. P'Oy and P'Ya for their several useful advices.

Thai Students at MIT (TSMIT) have been a big part of my life at MIT. Every weekend was full of smiling and joy and worth the wait because of their creativity to throw all kinds of activities. Special thanks to: Kim, Ae, P'Paan, P'Tao and N'Pee for the fun time at Porter house; P'Bo for kindly taking me under her wing; P'Jazz for unsuccessfully mentoring me to become "smooth"; Tip, P'Peng, Mon, Gift and Moo+ for the fun and competitive time over late-night Settlers of Katan; Pun for the exclusive deals and discounts; Jane for entrusting my opinions and all the thoughtful gifts; P'Yong for many shrewd advices; Yeaw for all his assistances during my post ACL operation and helping to prepare fruits & snacks for my thesis defense. There are so much more of the names that I would like to acknowledge but too limited space. For every one of them, I am thankful for the memorable times and embracing me into the TSMIT family.

I would love to thank my Sunday soccer team for all the fun pick-up games and competitive moments in the IM games and DC Queen Cup. It's a shame that my tear-ACL right knee kept me from playing with them for the entire year. Hopefully, I would be able to play with them again after my rehabilitation.

I started my U.S. journey as a member of the Thai scholars '97 eleven years ago. We were just kids who barely graduated out of high school and had to take a new, massive challenge far away from our homes. Fortunately, we held on together to impressively get through the first suffering and overwhelming year of TOEFL, SAT, college applications and AP classes. I would like thank them all for every fun and youthful moment we shared together and all the moral supports we provided to each other. Special mentions to: E who is one of the toughest girls who could stand with my badmouth habit (and sometimes even found it funny); Oat who was my first ever roommate in the U.S. and whom I got along quite well from the very first day; Kaew, Pew, Ning and N'Pond whom I reunited again in Boston.

Thanks to the Thai government and Thai tax payers for the scholarship that opening the gate to the U.S. for me when I was only 17 years old.

Finally, I would love to thank my family and relatives: Ah Ma, Papa, Mama, A, Ple, Ly, Meaw, See~ E~, Soy~ Koe, Ying and White for being a big part of my life. Thanks to Sa Jek, Na~ Toy, and Na~ Kai for believing in a high-school kid in me and helping me to secure my journey to the U.S.

This work is financially supported by the Office of Naval Research's MURI grant N. N0014-01-0758.

Contents

List of Figures

LIST OF TABLES

CHAPTER 1

INTRODUCTION

Ni–Mn–Ga based ferromagnetic shape memory alloys (FSMAs) have emerged as a promising new class of active materials due to a large magnetic-field-induced strain (MFIS). FSMAs can also be driven at higher actuation frequency than conventional shape-memory alloys (SMAs), which require heat flow to induce a large transformation strain. The field-induced strain occurs via twin-boundary motion. The FSMA shape change requires that the magnetic anisotropy of the martensitic FSMAs be larger than the energy required for activating the twin-boundary motion. Moreover, the easy direction (*c*-axis) of magnetization changes across the twin boundary as is necessary to achieve a large MFIS.

The idea of obtaining MFIS from Ni–Mn–Ga alloys was first described by Ullakko [1, 2] and James [3] in 1996. Then, measurements conducted at MIT in 1996 by Ullakko, et al. demonstrated a field-induced free strain of 0.2% in single crystals of Ni_2MnGa in the martensitic phase under a magnetic field of 8 kOe at –8 ^{o}C [4, 5]. Since then, many efforts have been made to study the Ni–Mn–Ga FSMAs and develop them to be suitable for actual applications. The measured maximum strain output has increased from the first-reported 0.2% to increasingly larger strains [6-8] and finally 6% [9]. The near-theoretical strain of approximately 6% was measured under a quasi-static field of +/- 320 kA/m in a tetragonal martensitic $Ni_{49.8}Mn_{28.5}Ga_{21.7}$ single crystal [9, 10]. Cyclic strains were limited to 3% under AC fields at frequencies below 400 Hz [11]. In these cyclic-actuation experiments, Ni–Mn–Ga crystals were oriented and cut into square prisms, with the faces along <001>. Actuation is achieved by applying to the FSMA a

magnetic field (using an electromagnet) that is perpendicular to the longitudinal bias stress. The quasistatic field-induced strain of 10% was recently reported in seven-layered modulated orthorhombic martensitic Ni–Mn–Ga [12]. A pulsed field was applied to FSMAs to achieve 6% strains in 200 micro-seconds [13]. Ni–Mn–Ga FSMAs show much larger field-induced strain at low frequencies than do other active materials such as piezoelectrics or magnetostrictors.

1.1 Crystallographic Structures

Ni_2MnGa is an intermetallic compound with the Heusler structure [14]. The point group symmetry of the stoichiometric compound in austenite is $Fm\bar{3}m$ with $L2_1$ ordering as shown in Figure 1-1 [15]. Off-stoichiometric Ni_2MnGa alloys are generally used in experimental research on FSMAs because they can be operated at room temperature due to their higher martensite transformation temperature.

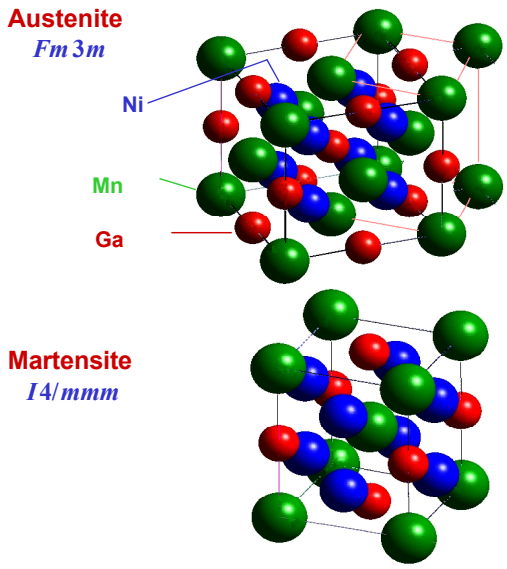

Figure 1-1: Structures of cubic austenite ($Fm\bar{3}m$) and tetragonal martensite ($I4/mmm$) of Ni_2MnGa. Nickel atoms (blue) are located in the interior tetragonal sites. Manganese atoms (green) are in the outer octahedral sites and gallium atoms (red) are at the corner positions [15].

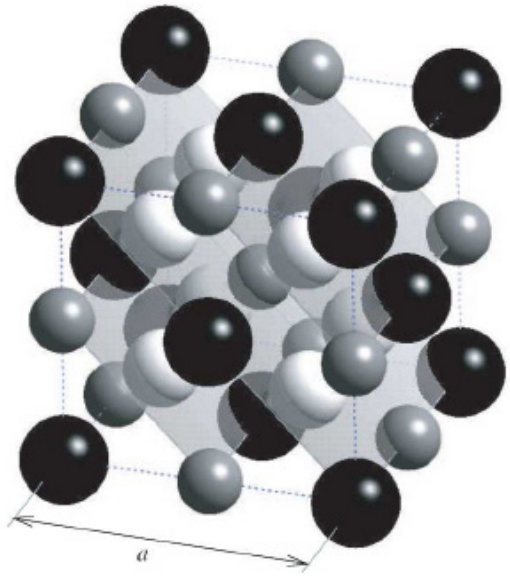

Figure 1-2: The crystal structure of cubic $Fm\underline{3}m$ Ni_2MnGa. The [110] planes shown in the picture can become twin planes in the martensitic phase [16].

Ni-Mn-Ga exhibits a martensitic transformation as it is cooled below the martensite start temperature (T_{Ms}) and completes the martensitic transformation at the martensite finish temperature (T_{Mf}). During the transformation, the lattice undergoes a cubic to tetragonal (or cubic to orthorhombic) distortion. For the martensitic structure shown in Figure 1-1, the transition is from cubic ($Fm\bar{3}m$) to tetragonal ($I4/mmm$) by shearing across {101} planes. Generally, different martensite structures are formed in Ni-Mn-Ga alloys depending on composition. For a 5-layer tetragonal martensite, the *c* axis contracts and the ratio of the *c* axis to the *a* axis is approximately 0.94. The (101) or (011) planes (Figure 1-2) in the cubic phase can become twin planes to accommodate the stress generated during the diffusionless transformation from austenite to martensite and the *c* axis becomes the easy axis for magnetization. Figure 1-3 illustrates the deformation due to a formation of twin planes in the martensitic cell [15]. As illustrated in Figure 1-3, the direction of the *c* axis changes across the twin boundary; the preferential direction of magnetization also changes because it is the *c* axis. The change of the magnetization easy axis across the twin boundary provides one of the requirements for the existence of MFIS [17]. For example, when applying an external magnetic field, the twin boundary

moves such that those twin variants that have their *c*-axis aligned with the field grow at the expense of those that have *c*-axis perpendicular to the field.

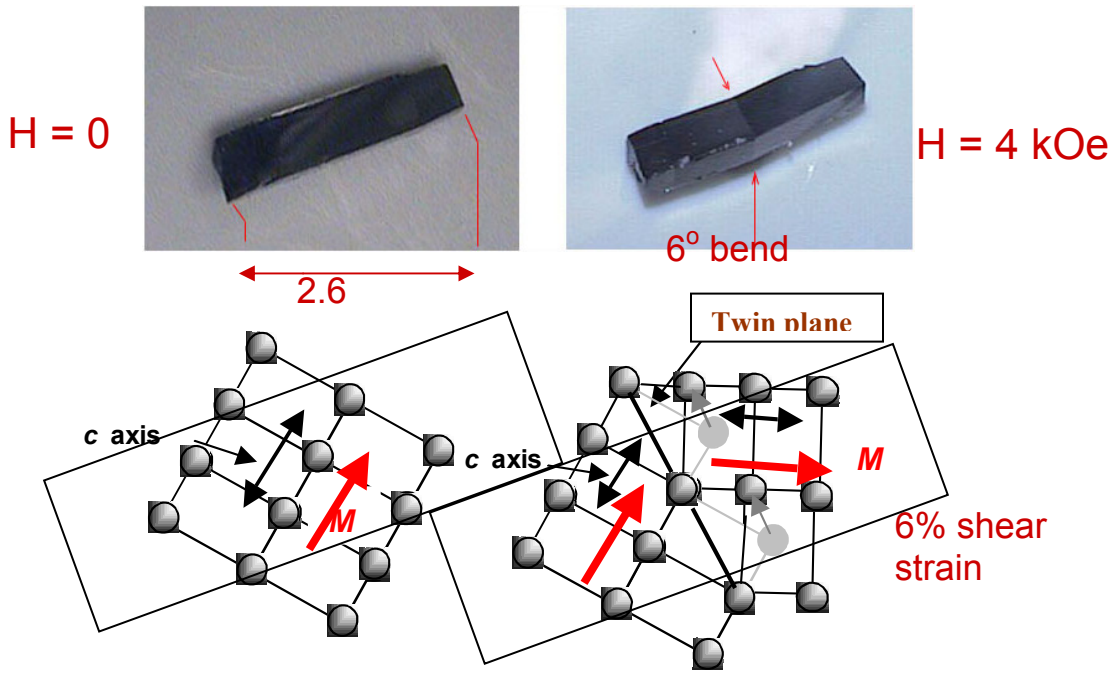

Figure 1-3: Illustration of the orientation of the martensitic unit cell (left) and the deformed martensitic cell due to the twin formation [15].

1.2 Research and Development on Magnetic-Field-Induced Strain of Ni_2MnGa FSMAs

With the initial state of the Ni–Mn–Ga sample having *c*-axis perpendicular to the field direction, the maximum field-induced strain under a static field actuation in a tetragonal crystal is $1 - c/a$ of a tetragonal crystal, which is 6% for a tetragonal martensitic Ni_2MnGa [18, 19]. Murray has reported a 6% one-time static strain in Ni–Mn–Ga that was achieved above a threshold magnetic field of 1–2 kOe [19].

Murray et al. also investigated the effect of an external-bias stress on MFIS of FSMAs under a static magnetic field [10] as shown in Figure 1-4. For low external stress (σ = 0.34 MPa), a full MFIS of 6% is achieved under the magnetic field of 800 kA/m. However, this external stress is too low to reset the FSMA sample back to zero strain and

the strain remains at 6%. For intermediate stress, between 0.78 – 1.62 MPa, large MFIS is achieved under an application of the magnetic field of 800 kA/m. Upon the removal of the magnetic field, the compressive stress is large enough to reset the sample partially (for 0.78 and 1.11 MPa) or fully (for 1.43 and 1.62 MPa). Stresses exceeding 1.63 MPa are too large for the magnetic field to fully actuate the sample and the reversible MFIS is small. It should be noted that the threshold field at which the onset of MFIS occurs increases with an increasing bias stress.

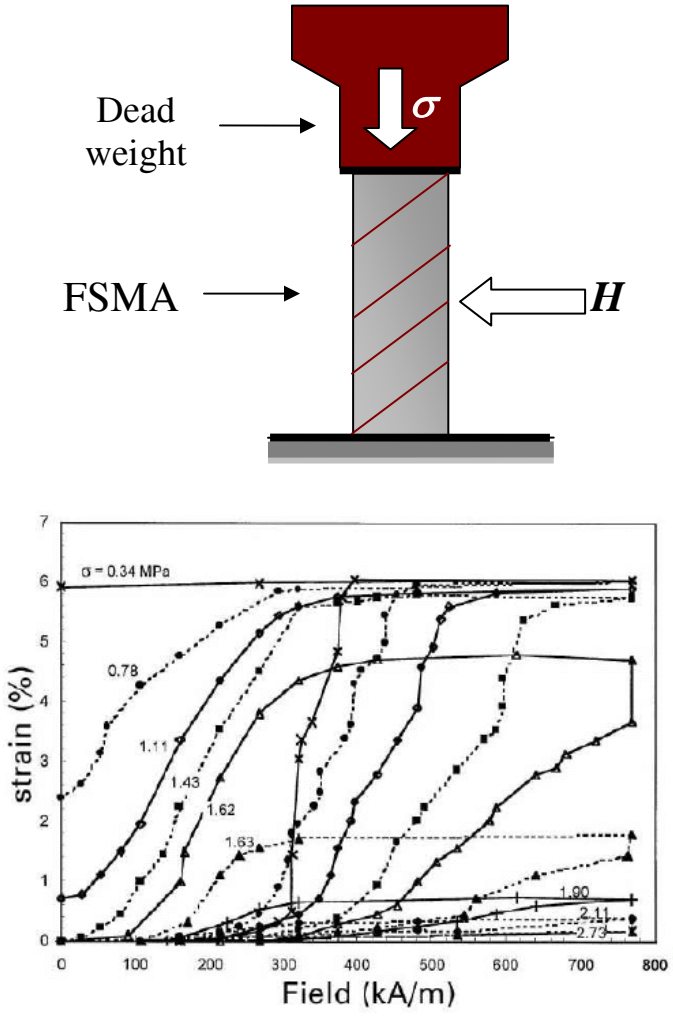

Figure 1-4: Upper figure: schematic of an experimental apparatus used to study quasi-static MFIS. Lower figure: MFIS as a function of the static magnetic field for a single crystal Ni-Mn-Ga sample under varying constant bias stresses [10].

Henry et al. studied the cyclic actuation of FSMA crystals driven by a magnetic field and using a spring to provide a variable bias stress [11]. The experimental apparatus for the cyclic actuation consists of a spring to exert a bias stress along the direction of actuation and a magnetic field applied perpendicular to the bias stress. The bias stress from the spring, which is compressed as the sample elongates due to the MFIS, enables a reset mechanism by compressing the FSMA sample when the field is reduced. An example of cyclic actuation data of Ni–Mn–Ga sample is shown in Figure 1-5. The data shows the maximum field-induced strain is achieved for intermediate bias stress values (between 1 and 2 MPa). However, the strain is reduced to 2.5–3% due to the bias stress from the spring as the sample is actuated. One reason for this reduced strain is the constraint put on the ends of the sample by the grips; this constraint can inhibit twin boundary motion in part of the sample length. For high bias stress (greater than 2.1 MPa), the MFIS vanishes, because the magnetic energy (limited by the anisotropy energy) is insufficient to overcome the bias stress as the sample extension increases the back stress from the bias spring. The FSMA sample responds with a small strain for low bias stress (less than 0.13 MPa) as the stress is insufficient to reset the sample once it has elongated.

The cyclic data of Figure 1-5 is smoother than the quasi-static data of Figure 1-4 and shows that a large threshold field of around 1–2.5 kOe is required to achieve cyclic FSMA actuation. A large threshold field would require large electromagnets to supply the fields sufficient to induce twin motion. The need for large electromagnets critically limits the use of FSMAs in many potential applications. Reducing the threshold field is critical to the development of FSMAs as competitive actuator materials.

Henry et al. also reported a large cyclic strain of Ni–Mn–Ga actuation over frequencies up to 500 Hz [11]. Beyond 500 Hz, the continuous actuation at 3% strain causes the sample to heat to above its martensite temperature in less than a minute unless active thermal controls are incorporated. The heating results from the irreversible processes in twin boundary motion. Consequently, the MFIS vanishes as temperature rises to near the austenite start temperature T_{As}.

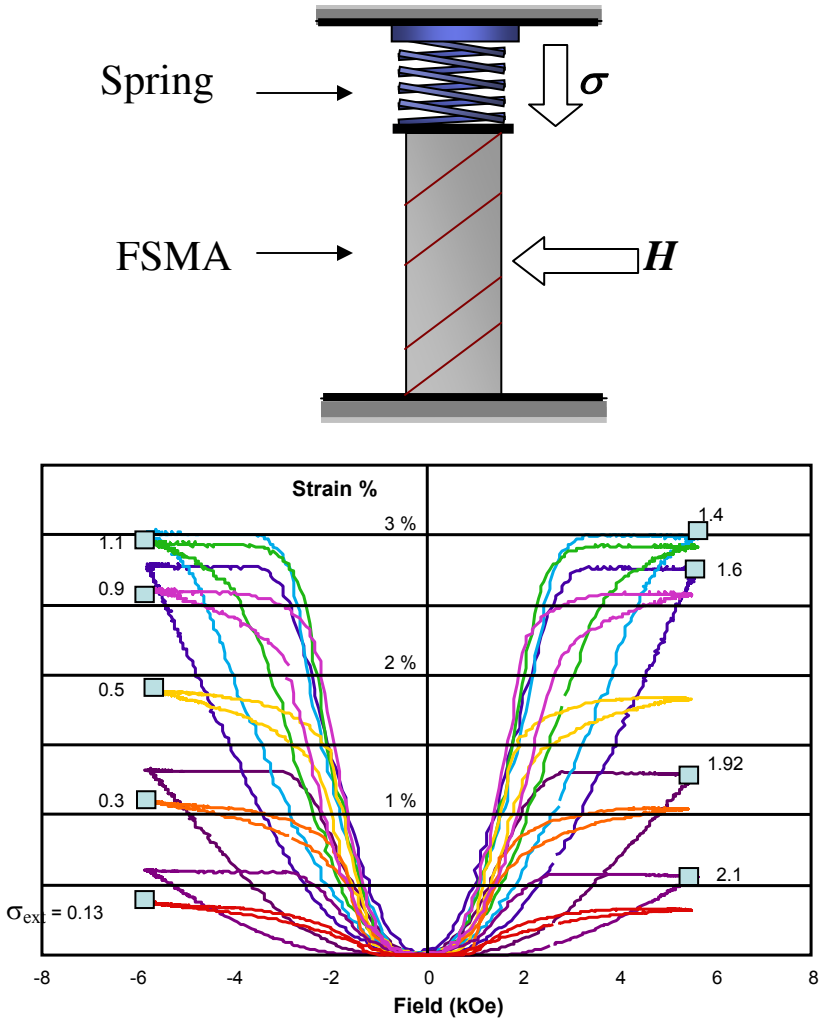

Figure 1-5: Upper figure: schematic of an experimental apparatus to study the cyclic actuation of FSMA. Lower figure: cyclic strain vs field at 1 Hz for different bias stresses in a Ni–Mn–Ga single crystal [11].

While FSMAs can exhibit strains up to 50 or 100 times greater than those of piezoelectric materials, they operate against smaller stresses. And, they have heating limitations (due to the large threshold field and hysteresis) similar to those of piezoelectric actuators.

In order to reduce the threshold field and the hysteresis loss due to twin boundary motion, the use of longitudinal acoustic waves from a piezoelectric actuator acting on the FSMAs has been proposed and demonstrated by Peterson et al. [20]. Waves traveling in the direction orthogonal to the applied field and at 45^{o} to the active twin planes would enhance atomic shear parallel to the twin boundaries and help promote twin-boundary

motion at a lower field. The preliminary results of MFIS of a Ni–Mn–Ga single crystal attached to a piezoelectric actuator show that higher strains can be achieved under a smaller field [20]. This shows that additional acoustic driving forces on the twin boundaries can enhance the MFIS performance of FSMAs. More details on the piezo-assisted actuation are presented below.

1.3 Mechanisms and Phenomenological Models of Magnetic Field-Induced Process in Ni–Mn–Ga

To achieve MFIS, the magnetic anisotropy of FSMAs must be larger than the energy required for twin boundary motion. Moreover, the easy direction (*c*-axis) of magnetization must change across the twin boundary to achieve high strains. As shown in Figure 1-6 [18], application of a magnetic field perpendicular to the easy axis of variant 2 causes the favorable variant 1 to grow. The twin boundary moves through the sample causing variant 1 to grow. The magnetic field imposes a pressure on the twin boundary due to the difference in magnetic free energy between the two variants. In variant 1, the magnetic easy axis is aligned along the field direction and the magnetic moments are stably oriented along the field direction. On the other hand, in variant 2, the magnetic easy axis is perpendicular to the field direction; therefore, the field-induced rotation of the magnetic moments away from the easy axis causes an increase in magnetic anisotropy energy. As shown in Figure 1-7, the free energy difference, $\Delta G = U_{\parallel}^{eq} - U_{\perp}^{eq}$, between the two variants increases with the increasing magnetic field [16]. The energy difference continues to increase until all the magnetic moments in the sample are oriented along the magnetic field at the anisotropy field, $H_a = 2K_u/M_s$, at which the maximum energy difference is attained. The maximum energy difference for MFIS in FSMAs is equal to K_u. Beyond H_a, the magnetic driving force remains the same at K_u; as a result, there is no extra benefit in applying a field higher than H_a.

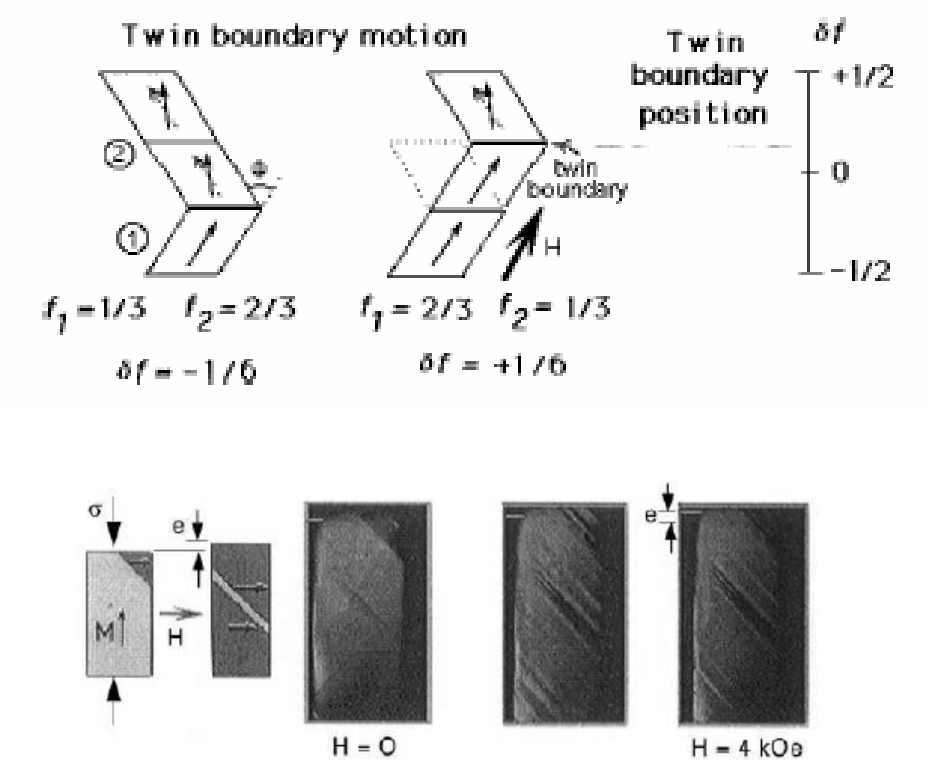

Figure 1-6: At the top, illustration of field-induced twin-boundary motion in a Ni-Mn-Ga single crystal with two variants separated by a mobile twin boundary. The parameters f_i (i=1,2) are the volume fraction of variant i. $\delta f = f - ½$ describes the displacement of the twin boundary from e=0 [17]. In the lower figure, three high-speed video frames showing the motion of twin boundaries under the static magnetic field [10].

Several models, varying by different physical interpretation of the driving forces of MFIS, have been proposed to describe MFIS in FSMAs. James and Wuttig [21] use a 'constrained theory of magnetostriction' to formulate a general micromagnetic model to predict strain versus field in a tetragonal martensite subject to an orthogonal magnetic field and uniaxial stress. O'Handley et al. [17, 18, 22] proposed a simple model to describe the MFIS of a single crystal with two variants using Zeeman, anisotropy, elastic and external stress energy. His model includes the effects of the magnetic anisotropy within the martensitic twins and also accounts for the nonlinearities observed in both $e(H)$ and $M(H)$ close to saturation. An alternative model, based on the magnetic torque, has recently been proposed by O'Handley [23]. In this model, the torque is maximum at $\frac{\sqrt{2}}{2} H_a$, whereas in the free energy model the energy difference between the variants

continues to increase until $H = H_a$. Likhachev and Ullakko [24-26] use experimental M-H and σ-ε data to generate analytical solutions for MFIS by differentiating a magnetization free energy expression to obtain the magnetic driving force.

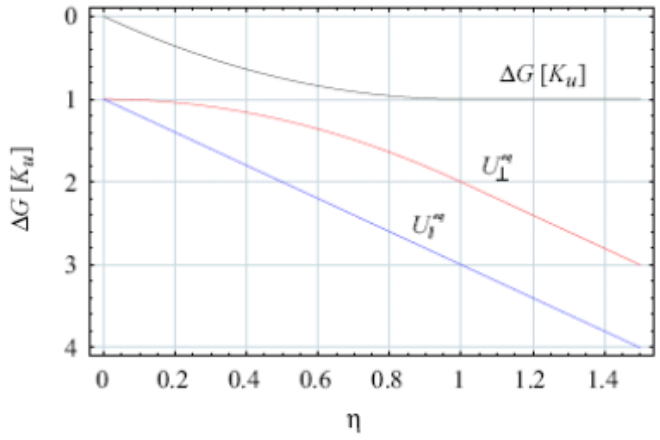

Figure 1-7: Free energy difference, $\Delta G = U_{\parallel}^{eq} - U_{\perp}^{eq}$, between the two twin variants: parallel ($U_{\parallel}^{eq}$) and perpendicular ($U_{\perp}^{eq}$) to the applied magnetic field. The reduced field η is equal to H/H_a, where H_a is the anisotropy field [16].

The phenomenological model developed by O'Handley considers a FSMA single crystal composed of two twin variants separated by a mobile twin boundary, as illustrated in Figure 1-6 above. The free energy expression may be shown as [17]:

$$g_i = -\mu_o M_i \cdot H + K_u \cos^2 \theta_i + \frac{1}{2} C_{eff} e^2 + \sigma \cdot e, \qquad \textbf{Equation 1-1},$$

where the subscript i corresponds to variant 1 or 2. The free energy expression above contains the Zeeman energy, $\mu_o M_i * H$, the magnetic anisotropy energy, $K_u \cos^2 \theta_i$ (θ_i is the angle between the magnetic field direction and the local magnetic moment in variant i), an internal restoring elastic energy, $C_{eff} e^2/2$, and an external-stress-induced energy, $\sigma * e$. The internal elastic energy density may be an elastic energy stored in unresponsive variants or a magnetostatic restoring energy density. C_{eff} is the effective stiffness of the martensite in the presence of mobile twin boundaries. The field-dependent strain is

expressed as a function of the volume fraction of each variant, f_i: $e(H) = e_o \delta f$, where $\delta f = f_1 - ½$ as shown in Figure 1-6 and e_o is the transformation strain, which is the crystallographic distortion in the martensitic transformation: $e_o = 1 - c/a$. The external stress is applied in a direction opposing the action of the magnetic field such that the field can be applied to actuate the sample while the stress serves to reset the sample.

The total free energy above can be minimized with respect to the twin-boundary displacement, δf, and with respect to the angles, θ_i. The latter gives $h = M_s H/(2K_u) = \cos \theta_2$. These two minimizations combine to give the expression of the field-induced strain as [17, 22]:

$$e(H) = e_o \delta f = \frac{2K_u h(1-\frac{h}{2}) - \sigma e_o}{C_{eff} e_o} = \frac{M_s H(1-h) + K_u h^2 - \sigma e_o}{C_{eff} e_o}, \qquad \textbf{Equation 1-2}.$$

As shown in Figure 1-8, Equation 1-2 indicates that, at small h, the field-induced strain is linearly proportional to H. The ratio of the balance between the Zeeman energies plus the external stress to the internal elastic energy, $C_{eff} e_o$, controls the strain at small h. A smaller magnitude of $C_{eff} e_o$ requires a lower magnetic field to achieve a given strain. As h approaches 1, H is large enough to rotate M_2, possibly without moving the twin boundary; the Zeeman energy difference across the twin boundary increases more slowly than linearly above $h = 0.2$ and is constant at K_u for $h > 1$. The maximum induced strain scales with $(K_u - \sigma e_o)/(C_{eff} e_o)$. A larger maximum field-induced strain is achieved with a decrease of $C_{eff} e_o$ and/or the threshold stress and an increase of K_u.

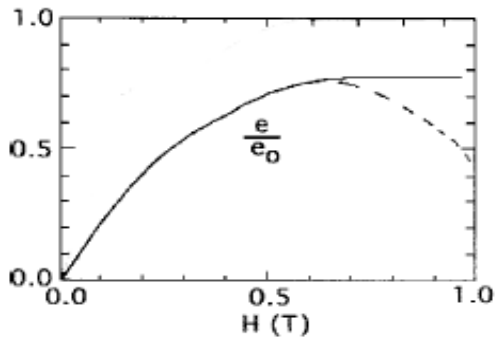

Figure 1-8: Reduced strain as a function of an applied magnetic field for $\mu_o M$ = 1.25 T, K_u = 3 x 10^5 J/m^3, Ce_o = 6.7 MPa and σ = 0 [17].

In O'Handley's magnetic-torque model [23], the magnetic-field-induced torque, defined as the angular derivative of the magnetic field energy, is postulated to be the driving force for the twin boundary motion. As illustrated in Figure 1-9, the clockwise magnetic-field-induced torque per unit volume acting on a twin variant 2, in which the magnetic easy axis is not aligned along the field direction, is given by:

$$\lambda = -\frac{\partial G_{\text{Zeeman}}}{\partial \theta} = -\frac{\partial\left(-M_s H \cos\theta_2\right)}{\partial \theta} = -2K_u h\sqrt{1-h^2} \qquad \textbf{Equation 1-3,}$$

where the standard definition, $h = H/H_a = \mu_o M_s H/2K_u$ and $\cos\theta_2 = h$ (derived from Equation 1-1 above), has been used [17]. This clockwise magnetic torque in variant 2 generates a mechanical clockwise torque on variant 2 shown in the right panel of Figure 1-9 (blue arc). If the sample were unconstrained, the crystal would rotate clockwise due to the magnetic torque on variant 2 such that the net moment aligns parallel to the field. If the sample is constrained, a counter-clockwise torque grows on variant 1 (red arrow in Figure 1-9) to balance the magnetic torque on variant 2. The torque on variant 2 (blue arc) promotes the motion of atoms in variant 2 in a wave-like motion along the twin plane, favoring growth of variant 1.

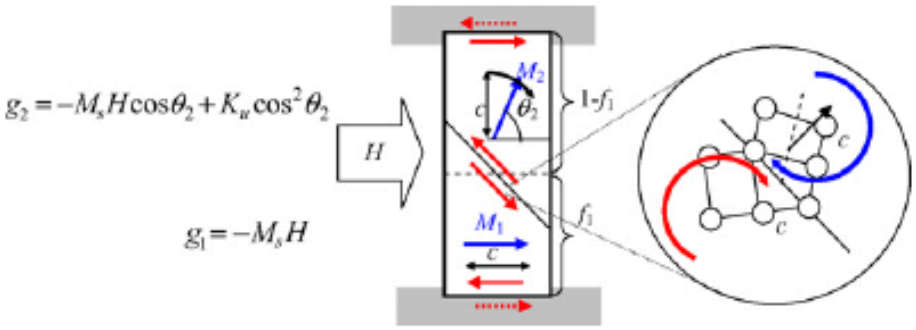

Figure 1-9: Illustration of a simple tetragonal martensite composed of two twin variants constrained at both ends. The magnetization directions in the sample is shown in blue arrows. The force couples for a free sample is indicated by the red arrows. The force couple due to constraints is shown in dotted red arrows. For the figure on the right, the magnetic-field-induced torque acting on a twin variant 2, whose the magnetic easy axis is not aligned with the magnetic field, is shown in blue and the mechanical torque on variant 1 due to the constraint is shown in red [23].

1.4 The Motion of Twin Boundaries and Twin Partial Dislocations

The model above describes the equilibrium behavior of FSMA actuation. It does not account for the kinetics of the twin boundary motion. The twin boundaries may possibly get trapped in metastable energy minima or pinned by defects; extra work not accounted in the model is required to move the pinned twin boundaries [16, 27, 28].

The motion of the twin boundaries occurs by the nucleation and movement of twin partial dislocations. The nucleation and motion of the twin partial dislocation may be driven by heating or cooling through the phase transformation temperature or by an applied stress or magnetic field [29, 30]. The driving forces for twin boundary motion included in Equation 1-1 also favor the motion of the partial dislocations. However, the driving force spent for the nucleation of the twinning dislocations is not considered in the model [16].

The energy spent in the nucleation of twinning dislocations also affects the motion of the twinning dislocations. The actual dislocation motion only occurs when a sufficient amount of successful nucleation attempts occurs [16]. Generally, the nucleation of a twinning dislocation requires much larger energy than that required for

dislocation movement [29]. The nucleation requires a typical stress of the order of 10 MPa [30, 31], which is larger than the maximum magnetic stress achievable in FSMAs by application of a magnetic field. It is more efficient to nucleate dislocations by an external stress and then move them by the application of the magnetic fields [30]. This is supported by the observation that a Ni-Mn-Ga single crystal needs to be *trained* by applying large external stress before a field-induced strain can be observed [16].

The nucleation can also be enhanced by thermal energy. The nucleation rate is exponentially proportional to $k_B T/(U_n - G)$, where U_n is the nucleation energy barrier and G is the nucleation driving force (e.g. an external stress or a magnetic field) [16]. Therefore, as temperature rises, a lower magnetic field or lower stress is required to nucleate the twin dislocations. As a result, in the *training* process of a Ni–Mn–Ga single crystal, an external compressive stress is applied on the crystal to nucleate dislocations during the austenitic-to-martensitic transformation.

Once nucleated, the partial dislocations can be pinned by defects and get trapped in a metastable energy well. This generates an energy barrier against dislocation motion. To overcome the barrier requires extra work. The rate at which attempts to overcome the barrier occur is important to the kinetics of the twin motion [16]. This is a thermally-activated process. The high mobility of the dislocations strongly enhances the twin motion. The average rate $\bar{\nu}$ at which a partial dislocation overcomes a pinning barrier of height $U_{barrier}$ has the form [16]:

$$\bar{\nu} = \nu_o e^{-(U_{barrier}+\Delta G)/(kT)}, \qquad \textbf{Equation 1-4,}$$

where ΔG is the driving force for the partial dislocation motion. Equation 1-4 shows that the rate, which is directly relevant to the average velocity of the dislocation motion, is enhanced by an increase of temperature. As the temperature rises, stronger atomic vibration enhances the mobility of the dislocations and, hence, the dislocations move from one energy minima to the other at a higher rate. Nucleation is also favored by lower stress or lower threshold magnetic field [30].

1.5 Defects in FSMAs

Through several experimental observations and reports [16, 28, 32], defects that cause twin-boundary pinning are believed to be responsible for the relatively high threshold field required to actuate FSMAs. The defect distributions, density and strength strongly influence the twin boundary mobility. It has been observed that single-crystal Ni–Mn–Ga samples of similar composition, cut from the same crystal boule, can have varying twinning stress and threshold field. The defects might be non-uniformly distributed inside the boule; therefore, the defect distributions and density can be varied in the samples from the same boule. As mentioned before, the large threshold field required for MFIS actuation is not due to the twin-boundary nucleation process, because the energy required to nucleate new twins is much higher than the maximum magnetic driving force [30]. With pre-existence of twin boundaries, the minimum stress needed to induce partial dislocation motion in the absence of impurities has to exceed the Peierls stress [30]. Ferreira has shown that the Peierls stress is smaller than the magnetic stress from a magnetic field of 8×10^6 A/m on a ferrous alloy containing twinned martensite plates. Rajasekhara later calculated the Peierls stress and the magnetic stress in Ni_2MnGa and confirmed that the magnetic stress from a very small field is sufficient to overcome the Peierls stress for twin-boundary motion [33]. However, the magnetic stress value might not be to sufficient to initiate dislocation motion in the presence of defects that interact with the dislocations and promote pinning [30].

Marioni [16, 28] observed the motion of individual twin boundaries and measured the defect strength distribution for a $Ni_{48.5}Mn_{26.2}Ga_{25.2}$ single crystal in a scale of K_u. Successively stronger magnetic-field pulses of 620 μs duration were applied to the crystal and the motion of individual twin boundaries was observed optically as shown in Figure 1-10. Twin boundaries were pinned at defects which were stronger than the applied magnetic pulse; and, when the pulse strength was increased, some twins overcame the pinning barriers and moved until they encountered a stronger pinning site. A distribution of defect strengths is shown in Figure 1-10(d); a large concentration of defects has

energies of 0.56 K_u. Defects stronger than K_u could not be quantified by his experimental method, because the maximum magnetic energy is limited by K_u.

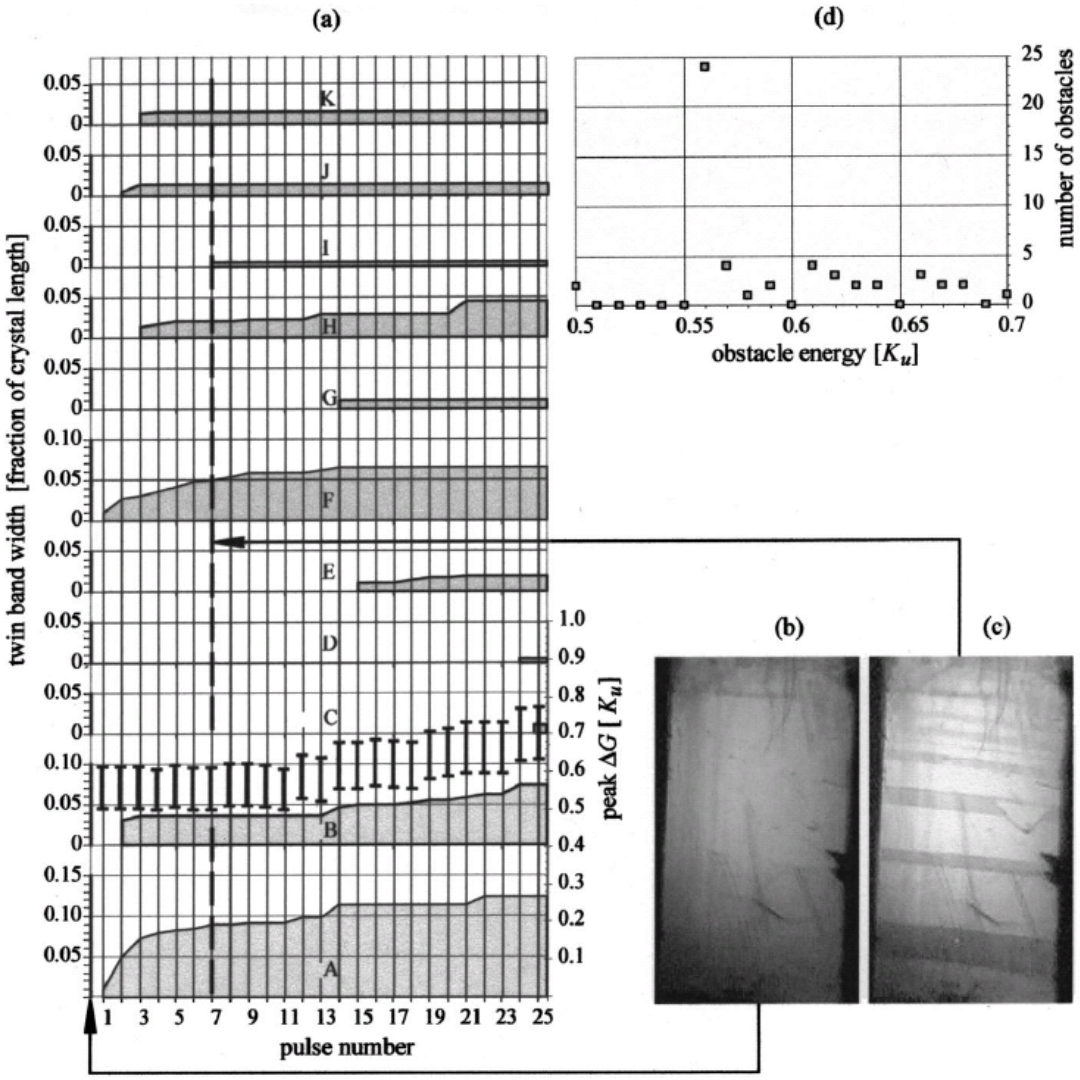

Figure 1-10: (a) Evolution of individual twin band thickness for a sequence of pulses without resetting. The individual twin bands are labeled by letters A – K. The superimposed uncertainty bars indicate the pulse strength in the scale of K_u. (b) Initial microstructure. (c) Intermediate microstructure (after pulse number 7); twin bands are visible. (d) The distribution of the defects strength [16, 28].

Richard [32] has studied the impurities and their interplay with the MFIS behavior in Ni–Mn–Ga single crystals through transmission electron microscopy (TEM)

observation and energy dispersive spectrometer (EDS) analysis. Sulfide inclusions were found throughout the samples of some single-crystal specimens. Sulfide inclusions ranged from 200 nm to 1 μm in size and seemed to be present throughout the sample thickness. The concentration of the sulfide inclusions was larger in the samples cut from the inactive single crystal boule (TL5) that did not show any MFIS as compared to the samples from the active crystal (TL8) that showed the maximum possible MFIS. The large number of sulfide inclusions may be responsible for the inactivity of crystal TL5. Ti-rich precipitates, ranging between 5 – 20 nm in size, were observed in the sample cut from the active single crystal (TL8). They were coherent and appeared in large clusters. The TL8 crystals are shown to exhibit the 6% MFIS; therefore, these precipitates may not significantly impede twin motion as they were small and coherent.

From the size of the defects observed in the TEM micrographs, Richard calculated the defect strength using the Orowan model [34, 35]. The dislocations would have to loop around the inclusions for twin boundary motion to occur. The stress required for a dislocation to loop around the inclusions is:

$$\tau = \frac{Gb}{l} \qquad \textbf{Equation 1-5,}$$

where G is the shear modulus, b the Burgers vector, and l the distance between pinning sites. The distance between two inclusions can be related to the volume fraction f and radius r of the inclusions as:

$$l = \frac{r}{\sqrt{f}} \qquad \textbf{Equation 1-6.}$$

From the equations above, the calculated defect strength for the sulfide inclusion in TL5 is equal to $1.58K_u$, which is larger than that measured by Marioni [28]. Clearly, the defect-pinning strength in TL5 is larger than the maximum magnetic energy for MFIS; therefore, it is not surprising that the crystal did not show magnetic-field-induced twin motion. The defect strength for sulfide inclusions in the TL8 sample is $0.50K_u$, which is consistent with the strength of the majority of the defects in the active crystal

measured by Marioni. The defect strength in TL8 is small enough that the magnetic energy could overcome the pinning resulting in the magnetic-field-induced twin motion.

1.6 Limitations of MFIS Actuation of FSMAs

FSMAs still have several characteristic shortcomings that may limit their potential applications. A threshold field of 2 to 4 kOe (depending on sample shape and condition) must be overcome to activate twin motion and a larger field is required to achieve full actuation. Such fields require an electromagnet that is large compared to the sample size and can account more than 95% of the total mass of the actuator device [36]. It is desirable in the design of an FSMA actuator to minimize the required size of the magnet.

In typical real-world applications, an actuator device will generally be required to actuate against opposing loads. A large stress output from the actuator is therefore desired. The operating window of the stress output from FSMA actuators is narrow and limited in the range between 1 – 1.5 MPa. Outside this operating range, the strain output diminishes significantly. As shown in Figure 1-4, although a 6% strain response can be achieved under a static field without constraint, MFIS decreases with the application of an external-resetting stress. Figure 1-5 shows that only up to 3% strains are achieved in AC-field experiments. A bias stress along the direction of elongation is commonly used in cyclic actuation to reset FSMA samples as H approaches zero. The magnetic energy that can be coupled into the material is limited by the anisotropy energy, $K_u \sim 1.5 \times 10^5$ J/m^3, and is insufficient to overcome an additional barrier from bias stresses greater than $K_u/\varepsilon_o \sim 1.5$ MPa [13, 18]. This limitation results in a reduction in an output strain relative to that of the unstressed state.

It is also reported that the sample temperature may increase above its martensite-to-austenite transition temperature in a short time in the cyclic actuation experiments when frequencies exceed a few tens of Hz, causing the MFIS to vanish [11]. This temperature increase is due to the large irreversibility in twin boundary motion. The temperature range of large actuation is presently limited between room temperature and 10–25 ^oC below the austenite-start temperature, T_{As}. Above the austenite-finish

temperature, T_{Af}, Ni_2MnGa becomes cubic austenite. Austenitic Ni_2MnGa shows no MFIS because there are no twin boundaries in austenite. It shows a small magnetostriction and has a magnetic anisotropy two to three orders of magnitude smaller than that of martensitic Ni_2MnGa.

1.7 Piezoelectric-Assisted, Field-Induced Strain in Ni_2MnGa Single Crystals

The limitations mentioned above are critical to the viability of FSMAs as alternative materials for actuators or sensors. Currently, some of these limitations are being addressed by the introduction of other driving forces (in addition to the magnetic field) to assist twin-boundary motion. The MFIS is due to the motion of the twin boundaries arising from atomic shear displacements along the twin boundaries. Thus, additional forces that would enhance the motion of the atoms along the shear direction would improve the twin-boundary mobility; the activation of twin motion might then require a lower threshold field.

To reduce the threshold field and achieve greater strain under a smaller field, Peterson et al. have developed the use of acoustic energy to assist a magnetic field in driving twin boundary motion in a Ni_2MnGa crystal [20, 37]. The experimental apparatus (Figure 1-11) of Peterson et al. consists of a piezoelectric actuator connected at the end of the FSMA crystal. The system incorporates a spring to exert a bias stress and provide a reset mechanism for the FSMA.

Figure 1-12 [20] shows the effect on offset magnetic-field drive of an FSMA at 1 Hz produced by a 1 kHz acoustic signal applied by a piezo stack actuator of varying amplitude (5, 35 and 55 V). The free displacements of a piezoelectric driven to 5, 35 and 55 V are 0.75 micron, 5.5 micron, and 8.7 micron respectively. The result indicates that the increase in amplitude of the acoustic input reduces the hysteresis and significantly enhances the strain output for the same peak-to-peak magnetic field. This shows that the larger amplitude compressive waves interact more strongly with the twin boundaries than do the smaller waves.

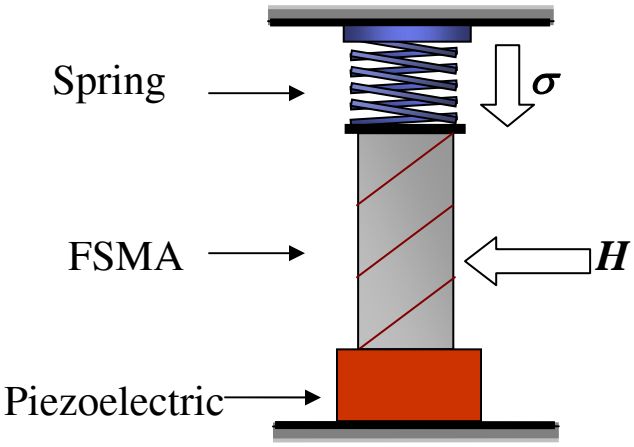

Figure 1-11: Schematic of experimental apparatus used for studying the effect of piezoelectric actuation on FSMAs.

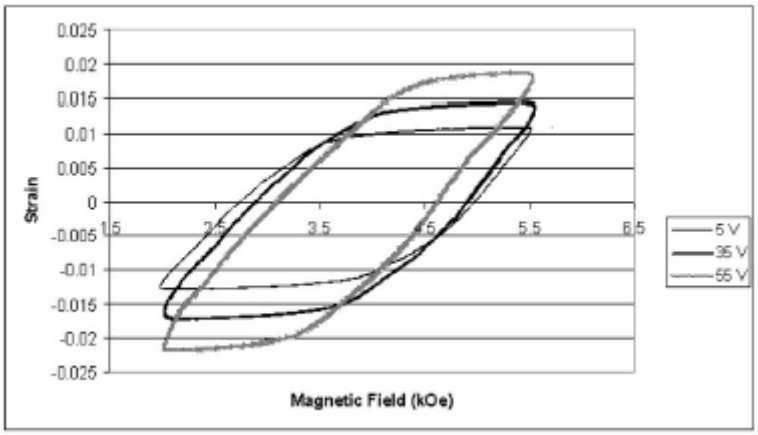

Figure 1-12: Magnetic-field-induced strain vs. magnetic field for 1 kHz piezoelectric actuation at varying piezoelectric displacements [20].

Figure 1-13 [20] shows the FSMA strain as a function of applied magnetic field for 40-V piezoelectric drive at frequencies between 30 Hz and 10 kHz. A small offset in the magnetic field was used to show differences in piezoelectric drive effects near and above the threshold field; the maximum field of the $H > 0$ side of the curve is slightly below the threshold field while the maximum field of the opposite side is slightly above the threshold field. The acoustic wave of the piezoelectric has the largest effect on the

output strain on the $H > 0$ side with a factor of 10 increase in the strain, while it has less effect on the $H < 0$ side, only doubling the strain output. The threshold field required to activate the twin boundary motion is also decreased slightly for higher frequency acoustic waves.

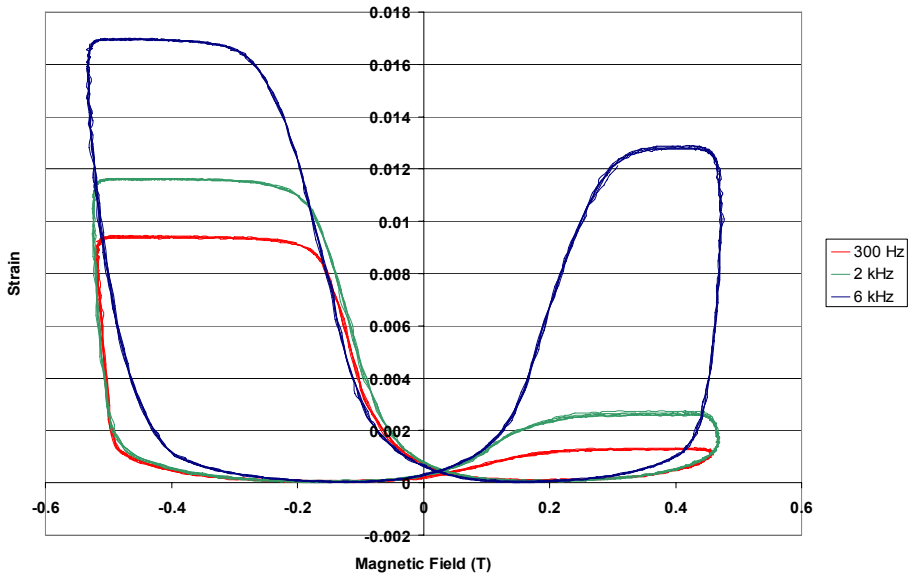

Figure 1-13: Magnetic-field-induced strain vs. magnetic field for constant piezoelectric displacement and varying frequency [20].

The results of acoustic-assisted MFIS show that the combination of piezoelectric and FSMA materials has the potential to enhance the output of hybrid Ni_2MnGa-based devices. To make such devices, it is important to understand better the effect of the acoustic-assisted actuation and to be able to construct a phenomenological model to explain the effect. Peterson et al. [38] propose a double-well potential model to explain the effect of piezoelectric actuation on MFIS. According to the model, the twin boundary motion is believed to be the result of atomic jumps between two equivalent sites on one side of the twin boundary (Figure 1-14). The two stable positions can be described by a double-well potential with the energy barrier present near the twin boundary, as shown in Figure 1-14a. An applied magnetic field or stress shifts the relative height of the two potential wells as illustrated in Figure 1-14b. When the applied field or stress is above a

threshold value, the atoms move to the well with the lowest energy and result in twin boundary motion. The piezoelectric actuation provides a longitudinal wave that resolves as a shear stress across a twin boundary. The resolved-shear stress from the piezoelectric actuation is thought to induce coordinated motions of the atoms in the potential well and thus make jumps into the lower-energy well more likely.

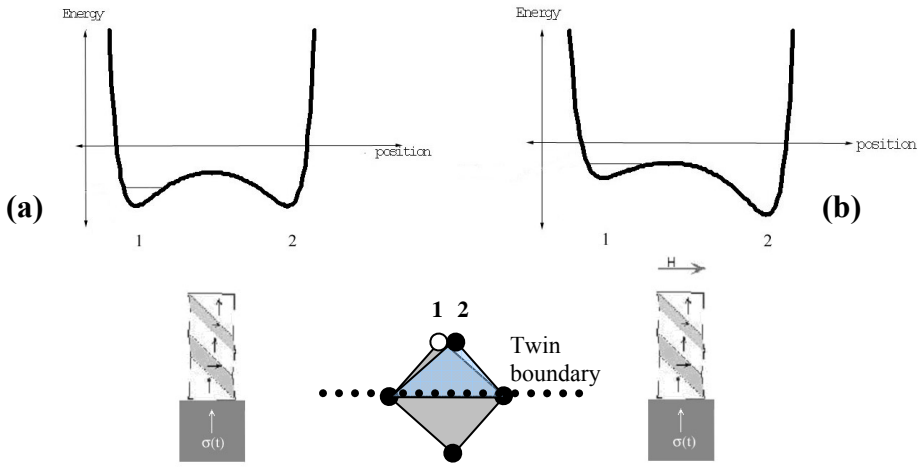

Figure 1-14: (a) Double well potential for the equivalent atomic positions 1 and 2 across a twin plane in the absence of an external field or stress and (b) a double well potential for the atomic position 1 and 2 shifted by an applied field or stress such that the position 2 is more favorable with lower energy [38].

Peterson et al. [37] also investigated the piezo-assist effect at varying FSMA actuation frequencies. The maximum piezo-assist effect reportedly occurred at FSMA actuation frequencies below 50 Hz. At higher frequencies, the dynamic response of the FSMA system became the limiting factor reducing the piezo-assist effect.

In addition to testing the piezo-assist effect on the in-house FSMA systems, Peterson et al. [37] tested the effect of piezo-assist with a commercially-available FSMA actuator from Adaptamat, Finland. The Adaptamat actuator (Figure 1-15) was modified by including a piezoelectric stack in series with the FSMA crystal along the actuation direction. Shown in Figure 1-16, the piezo assist increases the cyclic displacement of the actuator throughout the entire drive frequencies. Consistent with the results from the in-house actuator, the effect is largest at low magnetic drive frequencies.

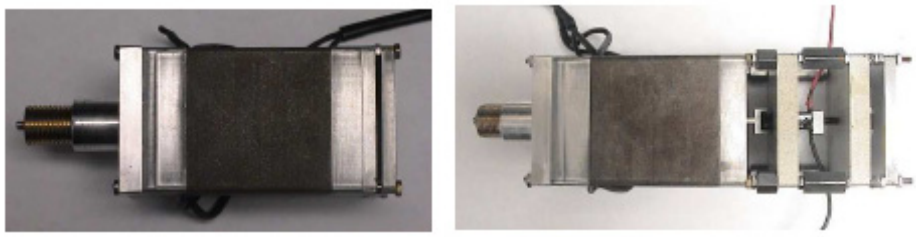

(a) (b)

Figure 1-15: Adaptamat actuators: (a) as-received actuator and (b) modified actuator including a piezoelectric stack on the right [37].

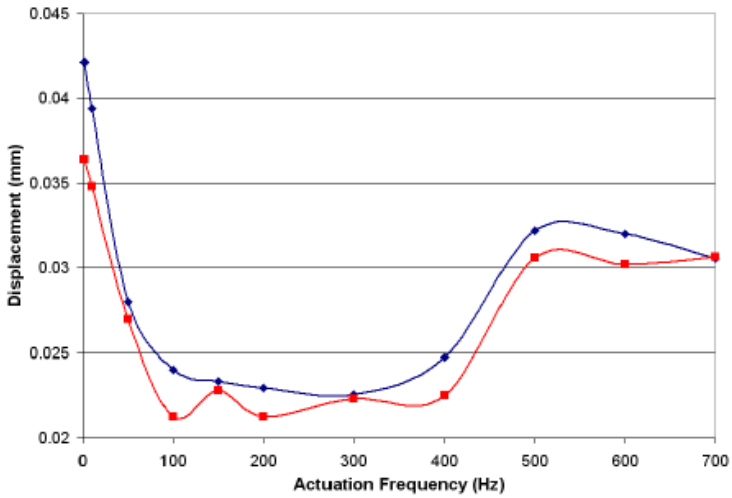

Figure 1-16: Cyclic displacement of the modified Adaptamat actuator as a function of FSMA actuation frequency without piezo assist (red squares) and with a 12 kHz and 15 V_{rms} piezo assist (blue circles) [37].

1.8 Acoustic-Induced Actuation in Ni–Mn–Ga Single Crystals

Chambers et al. [36, 39] have demonstrated that twin-boundary motion in an FSMA single crystal can be induced by using a piezoelectric stack to apply a series of asymmetric acoustic pulses without the necessity to apply a magnetic field. To compress the FSMA sample, the acoustic pulses expanded the piezoelectric stack rapidly (in about 30 microseconds) to transmit to the FSMA a compressive stress wave with magnitude higher than twinning-yield stress and recoil the stack slowly (in about 10 ms) resulting in

a tensile stress wave much lower than twinning-yield stress. The FSMA can also be extended by inverting the pulses applied to the piezoelectric stack in order to apply a tensile stress wave greater than the twinning-yield stress on the FSMA. As shown in Figure 1-17, the top panel shows the acoustic-induced strain over time and the lower panel shows the drive voltage across the piezoelectric stack over the same period of time. During the first 20 s, pulses of a sharp-rise voltage are triggered manually to send compressive stress pulses to a Ni-Mn-Ga single crystal (initially in the extended state). The small, stepwise compressive strain was induced accordingly. Then, series of pulses triggered at a repetition rate of 7.5 Hz were applied across the piezo stack to generate consecutive compressive stress waves in the crystal. The displacement of the piezoelectric stack after each pulse is a few microns while the extension of the FSMA after several pulses is a few tenths of a millimeter. For free actuation, acoustic-induced strain of 3% was achieved in 30 s, while 1% strain was achieved in under 1 s. This experiment suggests that the stress produced by the steeper asymmetric piezo drive exceeds the yield stress for twin-boundary motion.

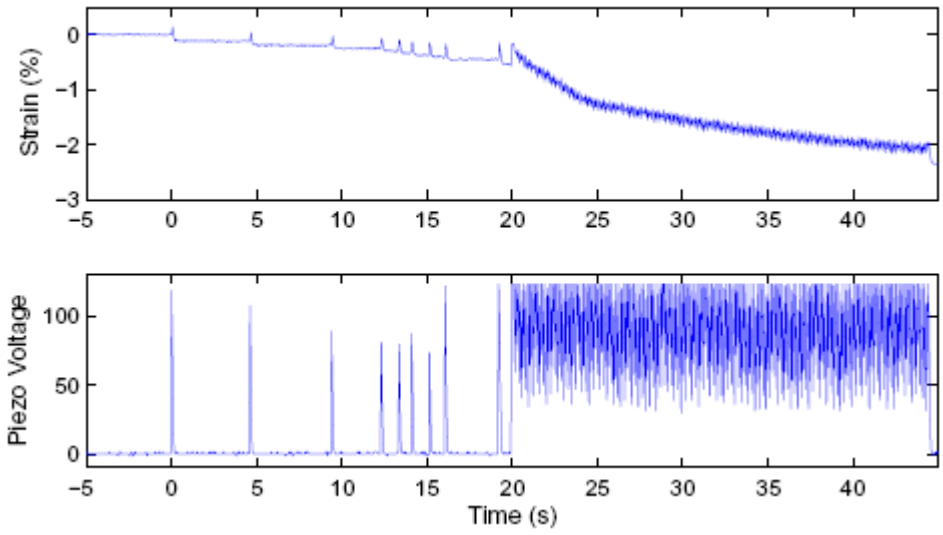

Figure 1-17: Acoustic-induced strain-vs-time (top) and Drive voltage across the piezoelectric stack over the same period of time (bottom). The crystal was fully extended before the measurement. The acoustic pulses were first manually triggered and then sent at a period of 7.5 Hz [36].

Building on the work by Chambers et al., Simon et al. [40] developed a transverse-acoustic actuation of Ni–Mn–Ga single crystals to acoustically induce shear strains of up to 5% in 2.5 s at a pulse repetition rate of 100 Hz, achieving over 3% strain within the first second. [110]-cut Ni_2MnGa single crystals were used by Simon instead of the [100]-cut Ni_2MnGa single crystals typically used in all the work mentioned above. [110]-cut single crystals contain twinning planes parallel to the base of the crystals, while [100]-cut single crystals have twinning planes oriented approximately 45 degree to the base. With the [110]-cut single crystals, a single 15-mode piezoelectric stack can generate series of shear stress pulses directly in the crystals, inducing atomic-shear motion along the twinning planes. The resulting deformation of the [110]-cut crystal is a shearing of the crystal so that its top surface shifts to the right or left of direct alignment over its base.

1.9 Demagnetizing Fields and Factors

Different applied field strengths are required to magnetize a ferromagnetic sample along the sample's long-axis direction as opposed to the short-axis direction, as illustrated in Figure 1-18 [41]. To achieve the same magnetization value, it requires a greater external magnetic field applied along the short direction than the field applied along the long direction.

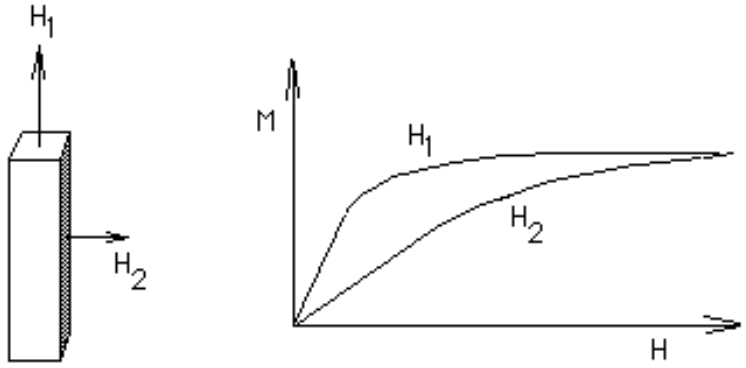

Figure 1-18: Magnetization-vs-an applied magnetic field curves for a polycrystalline ferromagnetic sample with field applied in different directions [41].

The shape-anisotropic behavior of magnetization is due to the "demagnetizing" field [41, 42]. Consider a polycrystalline ferromagnetic sample (Figure 1-19) under the application of an external magnetic field normal to the sample's surfaces. The external field H_{ext} acts on the sample to produce a magnetization in the sample along the same direction. The sample magnetization results in magnetic N or S poles on the surfaces normal to H_{ext}. These uncompensated magnetic poles give rise to a dipole field, H_d, that opposes the external field. This part of the dipole field that is inside the sample is the demagnetizing field H_d. The demagnetizing field acts against the external field such that the internal field H_i, to which M responds, is smaller than H_{ext}. The internal field may be written:

$$H_{int} = H_{ext} + H_d, \qquad \textbf{Equation 1-7.}$$

So far, M is assumed to be normal to the surfaces. Generally, $H_d = -M \bullet n$, where n is the unit vector normal to the surface. The demagnetizing field is a function of position and magnetization orientation inside a sample. For an arbitrarily-shaped sample, H_d for a given direction of M is approximately:

$$H_d = -NM, \qquad \textbf{Equation 1-8,}$$

where N is the demagnetizing factor. In general, N is a tensor function of sample shape. For a very long cylinders and the magnetization parallel to the long axis, N is zero. For a plane thin film with flat ends and M normal to the surfaces, $N = 1$. For an ellipsoid, N is a diagonal tensor and the diagonal elements correspond to the principal symmetry axes of the ellipsoid: N_x, N_y and N_z and the sum of these diagonal elements is equal to 1: $N_x + N_y + N_z = 1$ (in SI units). For a spherical sample, each diagonal element equals 1/3; the magnetization response along any direction of a sphere is identical. Clearly, it is easier to magnetize ferromagnetic samples along their long directions because the surface poles are further apart. A plot of demagnetizing factor as a function of the ratio of long axis to short axis with the magnetic field applied along the length axis for samples with various shapes are shown in Figure 1-20.

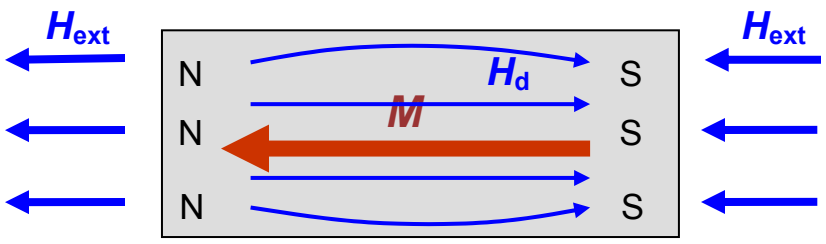

Figure 1-19: Diagram of a polycrystalline ferromagnetic sample under an application of an external magnetic field. Magnetization M is shown as the red arrow. Demagnetizing field H_d acts to oppose the external field.

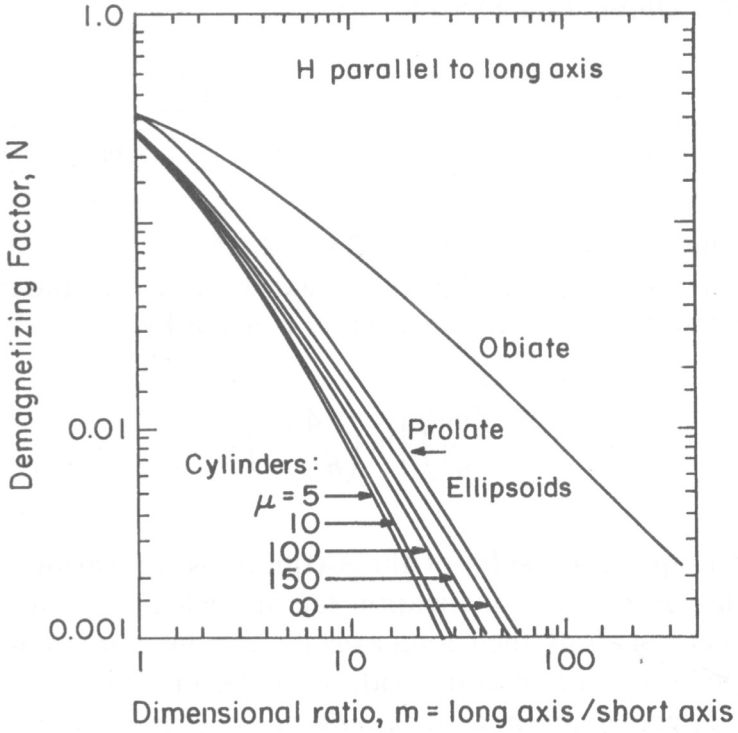

Figure 1-20: Demagnetizing factors for ellipsoids and cylinders with field applied parallel to long axis, with aspect ratios closer to unity [43].

Thus, it is important for actuator design to minimize sample demagnetizing factor so that a smaller external field is required for actuation. This cannot be done without other consequences for actuation.

1.10 Motivation and Goals of Thesis

This thesis aims to address the limitations of FSMAs' actuation that potentially limit their viability in practical applications. To improve the performance of FSMA actuators, this work is focused on the two major areas: (1) reducing the threshold field and thus the hysteresis for FSMA actuation and (2) increasing the stress output from the actuator while maintaining a large strain output.

Acoustic-assisted magnetic-field induced actuations of Ni–Mn–Ga single crystals have shown promising results to reduce the threshold fields. Peterson [37] has studied the benefits and limitations of piezo-assisted drive on the threshold and strain under dynamic actuation of Ni-Mn-Ga single crystals. However, dynamic FSMAs actuators require the FSMA samples to actuate under constrained conditions with bias stresses that may exhibit characteristics not related to the MFIS but rather due to system characteristics, such as frequency-dependent responses of a bias spring. These constraints may become limiting factors to the FSMAs actuation. The magnitudes of the piezo-assist effect directly on the FSMAs actuation may be understood better without constraints and under static loading conditions. As a result, to complement the study by Peterson, this thesis work considers three simple categories of relevant phenomena. First, the piezo effect on the magnetic response under a static magnetic field and no external stress is measured and analyzed. Second, the piezo-assist effect on the qausi-static mechanical response of FSMAs without bias magnetic field is studied by measuring the reduction in the twinning-yield stress due to the piezo drive actuation. Finally, the magneto-mechanical response of the FSMA actuation with and without piezo assist is studied.

Demagnetization effects may also play a significant role on MFIS. Magnetization is a critical part of the MFIS process; the magnetization energy is considered in all the widely-accepted phenomenological models for FSMAs. It is likely that the ease of magnetization has a major impact on the magnetic driving force responsible for twin boundary motion. To date, the demagnetization effect on MFIS is

not known to be seriously considered by any researchers in FSMAs-relevant fields. In this work, the effect of the demagnetizing field will be thoroughly explored.

Specifically, the goals of this thesis can be summarized as following;

(1) Study the demagnetization effect on the MFIS of Ni-Mn-Ga single crystals.

(2) Study the piezo-assist effect on the magnetic and mechanical responses of Ni-Mn-Ga single crystals under quasi-static conditions. For the magnetic response, MFIS as a function of a quasi-static magnetic field is to be measured. For the mechanical response, the compressive strain and stress data are measured from FSMA samples.

(3) Study the piezo-assist effect on the magneto-mechanical response of Ni-Mn-Ga single crystals. This category will allow us to investigate the effect of piezo-assist impact on the stress output of the FSMA actuation.

1.11 Thesis Overview

Chapter 2 describes the preparation and heat treatment for the Ni–Mn–Ga samples used in this work. The experimental apparatuses and procedures conducted throughout this work are also explained.

The demagnetization effect on the threshold field is reported and discussed in Chapter 3. The magnetic field is applied along two different directions: the samples' length and width, noted as longitudinal and transverse fields accordingly. The magnitude of the demagnetizing field is different for the two field directions. The experimental data demonstrate the demagnetization effect on the MFIS. Consequently, the phenomenological free energy model, discussed in Section 1.3, must be modified by incorporation of the demagnetizing field to adequately explain the empirical observations. This is done also in Chapter 3.

The piezo-assist effect on FSMA actuation is presented in Chapter 4. The characterization of the piezo-assist effect on the pure magnetic and mechanical responses of FSMA actuations is described in this chapter. The data on the reduction of the threshold field and the mechanical twinning-yield stress is shown first. The theory of stress waves is discussed to facilitate understanding of the resonant frequencies of the

longitudinal and transverse modes that may be generated by the piezo-assist actuation. The yield stress data are subsequently interpreted using the knowledge from stress-wave theory to explain the piezo-assist effect on FSMA actuation. Finally, the finite-element method (FEM) is used to analyze and model the stress waves generated in the FEM assemblage equivalent to the sample setup.

Chapter 5 shows the experimental results for the magneto-mechanical responses of the FSMA actuation. The Ni–Mn–Ga samples were magnetically actuated with an AC field and compressively reset by a constant bias stress to obtain cyclic strain of FSMA actuation. The piezo-assist effect on the stress output of FSMA actuation is reported and discussed.

Finally, the results and contributions from this thesis work are summarized and conclusions are drawn in Chapter 6. Future recommendations building on to this work are also mentioned.

CHAPTER 2

EXPERIMENTAL PROCEDURES

2.1 Sample Preparation

Off-stoichiometry, tetragonal Ni_2MnGa single crystals are used throughout this work. The single crystals, grown by the Bridgeman method, were supplied by Ames Laboratory in Ames, Iowa [44]. The as-cast single-crystal boules, approximately 25 mm in diameter and 75 mm in length, were homogenized at 1350 ^{o}C for one hour; as a result, the composition throughout the crystal boules is relatively uniform. However, the presence of a slight variation in composition along the length of the boules can still be observed (a 1% increase in Mn content in the growth direction is typical).

The crystal boules were oriented by Laue diffraction and cut using spark-erosion EDM into rectangular prismatic samples with faces parallel to the austenitic {100} planes. The Ni–Mn–Ga cut samples were lightly polished down to 400 grit paper such that {202} twin planes are discernible. They were wrapped with tantalum wires and encapsulated in quartz ampules under argon atmosphere. The encapsulation helped prevent the samples' surface oxidation during heat treatment. The tantalum wires protected the samples from touching quartz and, hence, prohibited direct diffusion of silicon into the samples.

During the heat treatment, the samples were slowly heated and held at 900 ^{o}C for 24 hours. They were then slowly cooled to 500 ^{o}C, and held there for 2 hours to allow for $L2_1$ ordering. They were then cooled and held at 200 ^{o}C until being removed from the furnace. After removal from the furnace and breaking the quartz capsule, the samples

were air-cooled to room temperature with a constant compressive stress of approximately 10 MPa applied along the long axis. The external load ensured that, during the martensitic transformation, the crystals formed a single-variant state with the *c*-axis parallel to the loading direction.

After the heat treatment, the samples were "trained" to activate the twin boundary motion. First, a large compressive stress was applied along the length direction and subsequently a stress perpendicular to the length direction was applied. This mechanical stress cycling was repeated until the large strain due to stress-induced twin motion was observed. Care must be taken that the compressive stress transverse to the sample length is always applied to the same set of opposing faces. It should be noted that a large mechanical stress was required before field-induced twin motion could be achieved, which suggests that the magnetic stress is only able to induce twin-boundary motion but cannot nucleate twins.

The samples tested in this work were cut from two different boules, labeled as TL8 and TL9. The compositions of the two crystals are shown in Table 2-1. Two samples, used in this work, were taken from the TL8 boule: TL8-1A and TL8-3C; both samples should have similar composition. Sample TL9-1A was the only one from the TL9 boule used in this work. All three single-crystal samples were active exhibiting MFIS. The dimensions of samples are shown in Table 2-2.

Table 2-1: Nominal composition (at%) of the crystal boules from which the samples tested in this work were cut.

Crystals	**Ni**	**Mn**	**Ga**
TL8	50.3	28.2	21.5
TL9	50.2	29.6	20.2

Table 2-2: Dimensions of the samples used in this work.

Sample	Length (mm)	Width (mm)	Thickness (mm)	Cross Section (mm^2)
TL8-1A	16.3	3.4	2.2	7.04
TL8-3C	17.2	3.8	2.3	8.74
TL9-1A	16.3	4.5	2.2	9.9

2.2 FSMA Magnetic Response Measurement

To study the effect on the threshold field of demagnetization and acoustic assist, the magnetic-field-induced strain (MFIS) of FSMA actuation under a quasi-static magnetic field is measured. The diagram and photograph of this apparatus are shown in Figure 2-1. A commercial PZT (lead zirconate titanate) 33-mode piezoelectric stack, model TS18-H5-104 from Piezo Systems, Inc. (specifications and displacement data shown in Table 2-3 and Figure 2-2), was used to provide longitudinal stress waves to the FSMA samples. The 33-mode piezo stack was attached to an aluminum base with Loctite© 840 superglue recommended for metal-to-metal or metal-to-ceramic bonding. A Ni–Mn–Ga single crystal sample was then glued, using the same superglue, to the piezo stack; the superglue bond ensured that the stress wave from the piezo actuation was efficiently transmitted into the FSMA sample. The aluminum base with the piezo stack and the sample was attached to a rectangular aluminum frame. A capacitance probe was attached to the frame at the opposite side and a grounded-copper plate was glued to the sample. An ADE model 3800 capacitance gauge was used to measure the distance between the grounded plate and the probe.

The frame with all the parts attached was inserted in the gap between the adjustable electromagnet poles. The electromagnet, powered by LakeShore Model 647 electromagnet power supply, generated a maximum magnetic field of approximately 10 kOe. The sample frame could be rotated 90^o such that the magnetic field direction is oriented either along the sample's length or width directions for a longitudinal field or a transverse field correspondingly.

MFIS response was characterized with the following procedures:

1. For longitudinal-field actuation, the sample was initially expanded longitudinally (contracted, laterally) by an application of 8-kOe transverse field. Vice versa, for a transverse-field measurement, the sample was initially contracted longitudinally by an application of 8-kOe longitudinal field.
2. The piezo drive peak-to-peak voltage $V_{p\text{-}p}$ and frequency were set to the desired values. The $V_{p\text{-}p}$ ranged from 0 to 50 V and frequency from 0 to 20 kHz. The piezo stack was driven at 10% duty cycle: it was driven at the desired $V_{p\text{-}p}$ for 60 μs and dormant for the remainder of a 600 μs repetition period). This was to prevent the piezo stack from heating up, which would affect the FSMA sample properties.
3. The quasi-static magnetic field was applied in 0.1-kOe incremental steps. The magnetic field magnitude and the sample's corresponding displacement were measured with a Hall probe and a capacitance proximity gauge, respectively.
4. After the saturation MFIS was achieved, the field was reduced in a 0.5-kOe step. A coarse step was used for decreasing field because there was no mechanical resetting and the full strain was expected to remain unaffected by a reduction of the field.
5. The piezo drive was turned off after the completion of measurement.

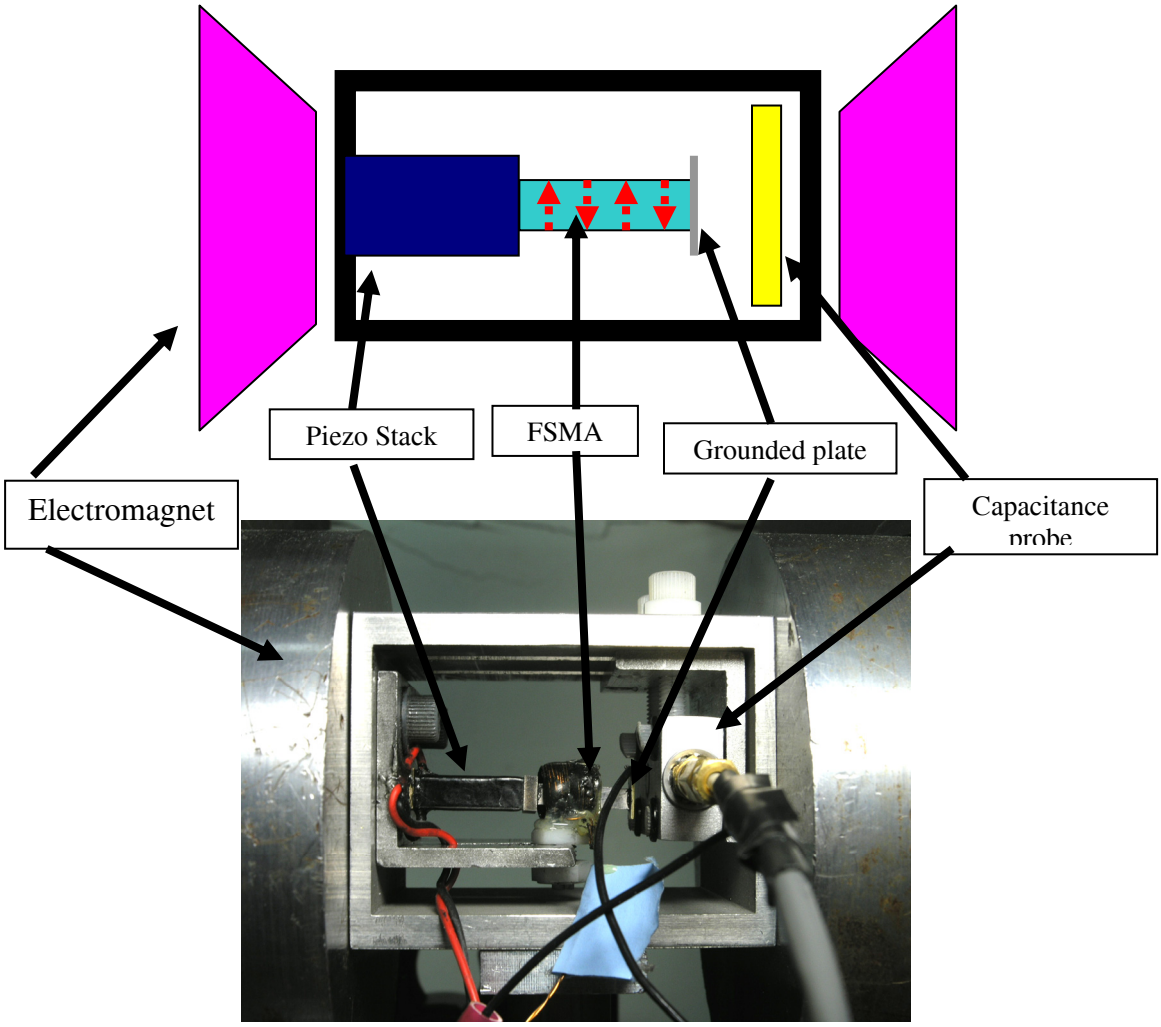

Figure 2-1: Diagram and photograph of the experimental apparatus for the MFIS measurement.

Table 2-3: Specifications for the piezoelectric stack actuator model TS18-H5-104 from Piezo Systems, Inc [45].

Dimension	0.2 x 0.2 x 0.72 inches
Compressive Strength	8.8×10^8 N/m^2
Young's Modulus	8.8×10^8 N/m^2
Stiffness	5.8×10^7 N/m^2
Poisson's Ratio	0.34
Density	7,900 kg/m^3
Capacitance	1,600 nF
Free Deflection	14.5 micron
Blocked Force	840 N

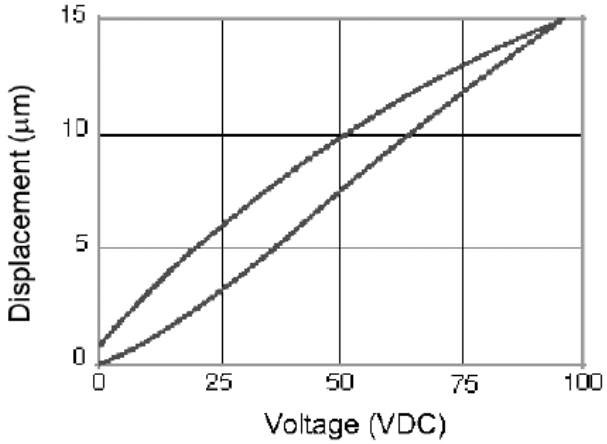

Figure 2-2: Free displacement as a function of applied voltage for a piezo stack actuator model TS18-H5-104 from Piezo Systems, Inc. [45].

2.3 FSMA Mechanical Response Measurement

The apparatus for the measurement of mechanical response of a single crystal FSMA is shown in Figure 2-3. A pneumatic piston cylinder, MMQ TB10-35D from SMC corporation, was used to apply a compressive load to an FSMA sample. The frictionless design of the cylinder allowed low breakaway pressure (< 0.5 psi) to initiate a push rod motion. The cylinder was pressurized with compressed nitrogen gas, controlled by a precision gas regulator from Marh BelloFram. The pressure regulator could control the pressure as precise as 0.1 psi, ranging between 2 to 100 psi. Pressure of 10 psi inside the cylinder exerted a force of 1 lb. A maximum force from this setup is 100 psi, which approximately corresponds to a stress of 4.5 MPa for a cross-sectional area of 10 mm^2, which exceeds the required twinning stress for typical FSMA single crystals. An Entran PS-30 load cell, ranging from 0 to 28 lb, was placed in line between the cylinder's push rod and the sample to measure the force exerted on the sample. A grounded copper plate was placed between the push rod and the load cell; it extended out beyond the edge of the sample. A stationary capacitance probe was attached to the main frame slightly above the copper target, allowing measurement of sample displacement. The sample was compressed along its length on top and glued to the piezo stack on the bottom. The piezo stack was attached to a removable aluminum base. During the measurement, the base,

with the piezo stack and the sample attached, was firmly held (by tightened screws) at the base of the main frame.

The measurement procedure was the following:

1. Before the measurement, the sample, attached to the piezo stack and the aluminum based, was magnetically expanded along its length by a transverse field of 8 kOe.
2. The aluminum base with the piezo stack and the sample was then attached to the main setup with a compressive load applied along its length on top of the sample.
3. The piezo stack was driven to the desired $V_{p\text{-}p}$ and frequency at a 10% duty cycle (the piezo-drive procedure and duty cycle are similar to the magnetic-response measurement).
4. The pressure in the cylinder was then slowly increased at an approximate rate of 3 kPa/s. After the full compressive strain is achieved, the pressure was slowly reduced to zero. During loading and unloading, the force and the displacement were simultaneously collected by a LabView software program via a LabView USB-DAQ interface to a computer.
5. The piezo drive was turned off after completion of the measurement.

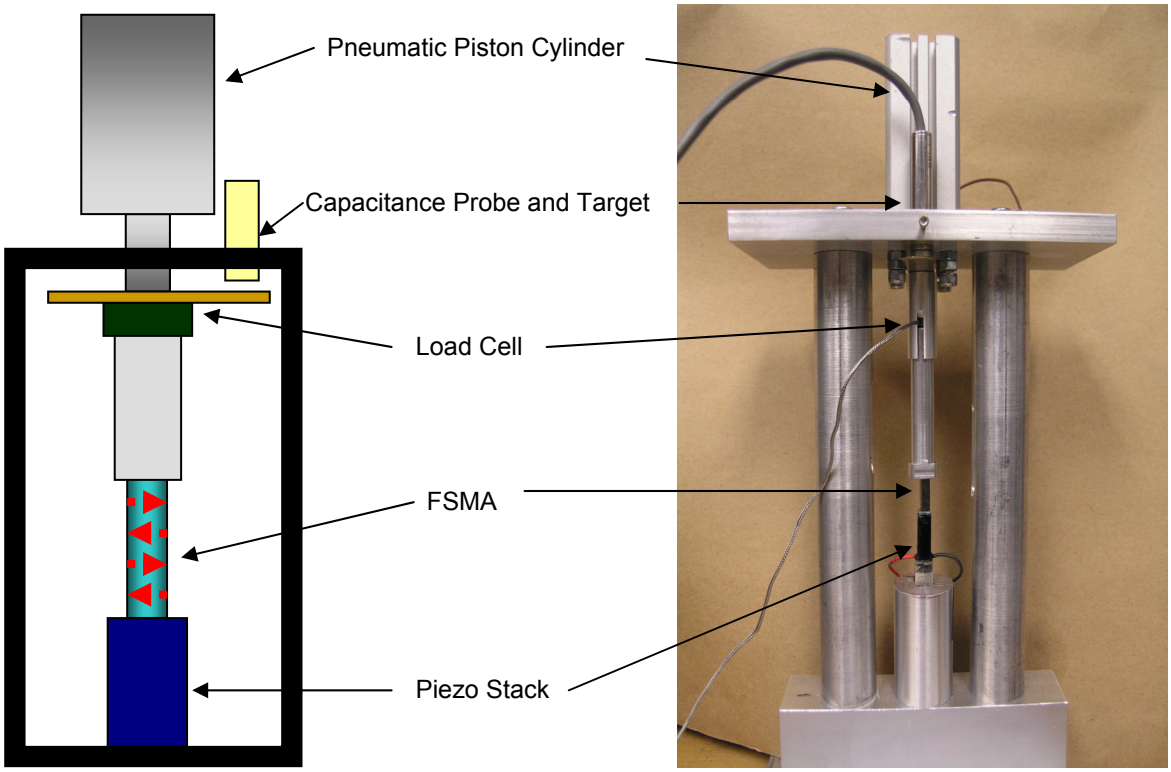

Figure 2-3: Experimental apparatus for the measurement of the magnetic response of the Ni-Mn-Ga single crystal samples.

2.4 FSMA Magneto-Mechanical Response Measurement

In this experiment, data of strain versus magnetic field under a constant bias stress were measured. The magneto-mechanical response apparatus (Figure 2-4) was a modification of the mechanical-response apparatus. The setup for an application of mechanical stress was identical to the one shown in the previous section. The *X*1 inductance-coil magnet, also used by Henry [11] and Peterson [37], was used for producing an AC magnetic field. The specifications for *X*1 magnet are shown in Table 2-4.

The experimental process is as follows:

1. The FSMA sample was initially compressed by a 3 MPa stress.

2. The bias stress was set to a desired level and kept constant throughout the field/strain cycle. This is different than the variable stress applied by the spring in Henry's measurements, Figure 1-5.
3. The piezo stack was driven to the desired values of $V_{p\text{-}p}$ and frequency at a 10% duty cycle (as in the previous two experiments).
4. The *X*1 magnet was driven to trigger two cycles of a 0.05 Hz AC magnetic field starting from zero to 5 kOe. The magnitude of the field and the displacement were simultaneously collected using a LabView USB DAQ interface and LabView software program.
5. After the data collection was completed, the piezo drive and the bias stress were reset to zero.

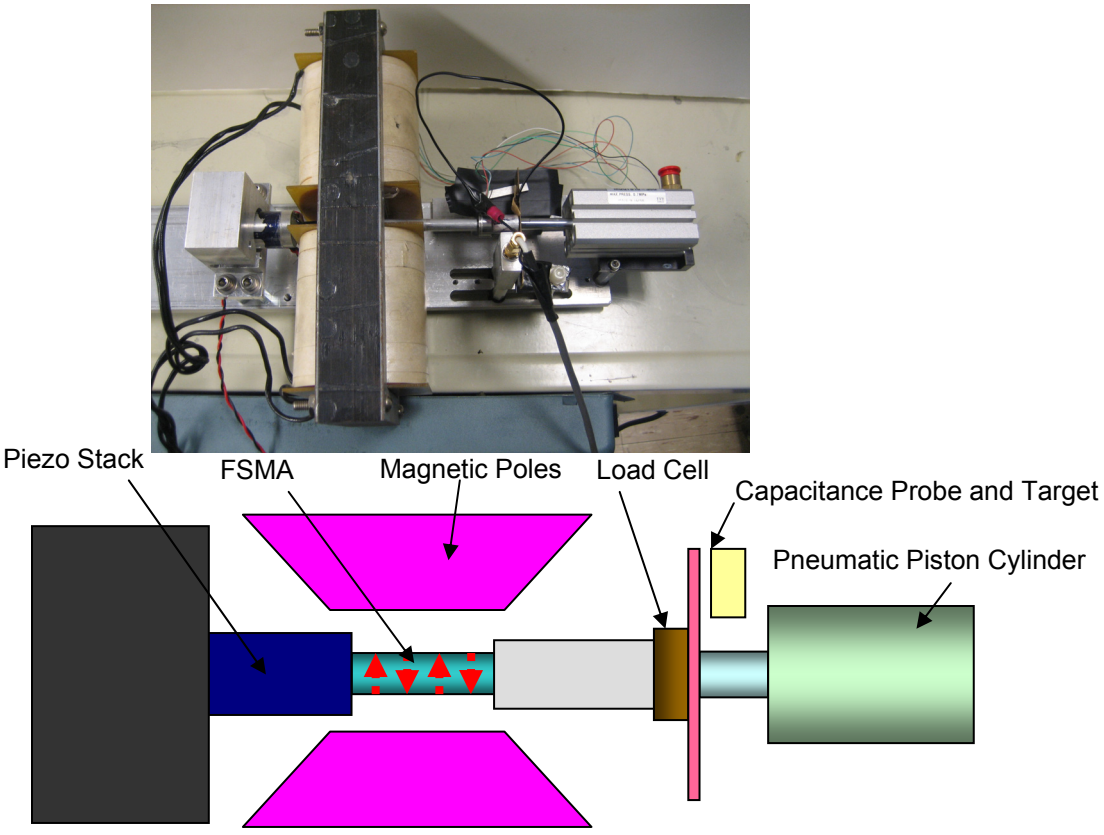

Figure 2-4: Experimental apparatus for the measurement of the magneto-mechanical response of the FSMA actuation.

Table 2-4: *X*1 magnet specifications [11].

Wire Gauge	18
Turns per coil	1000
Resistance in parallel	4.4 ohm
Inductance in parallel at 60 Hz	117.7 mH
Gap Volume	5.4 cm^3
Maximum Current	14 A
Maximum Field	9 kOe

CHAPTER 3

DEMAGNETIZATION EFFECTS

3.1 Experimental Results

The magnetic field induced strain (MFIS) was measured for the Ni–Mn–Ga single crystal samples under two different orientations of an applied field. First, the field was applied along the sample's length direction, called a longitudinal field. Second, the field was applied along the sample's width direction, called a transverse field.[1] Before applying a longitudinal field, the initial state of the samples was set by applying an 8-kOe field across their width to ensure the crystal easy axis of the dominant variant is perpendicular to the sample length. Before applying a transverse field, the intial state of the samples was set by applying a 8-kOe field along their length to insure a dominant *c* axis orientation along the sample length. For both field orientations, the field-induced strain is measured along the sample length direction. As a result, MFIS is negative under a longitudinal field and positive under a transverse field.

Magnetostatic theory dictates that the magnetic field inside a magnetic sample H_i is reduced from the external applied field H_{ext} by a shape-dependent counter action arising from the induced magnetic surface charges $M \bullet n$ on the sample surface, $H_i = H_{ext} - NM(H)$, where N is a demagnetizing factor. This reduced internal field requires that a greater field be applied to achieve a given state of magnetization inside the sample. Accordingly, the shape anisotropy during a longitudinal field application should be much

[1] Here, the width direction must be the same as that used in training the sample.

smaller than that under a transverse field. In the other words, if the crystallographic magnetic anisotropy (K_u) is excluded from the consideration, it is more difficult to magnetize samples along the samples' width than along the samples' length.

The plots of MFIS-vs.-field for sample TL8-1A are shown in Figure 3-1. The two fields induce the same magnitude of MFIS, ε = 0.05, but of different signs. The maximum strain measured for this sample is lower than the theoretical martensitic strain, ε_o = 0.06. It is likely that the variant rearrangement does not fully complete. A small fraction of unfavorable variants may still remain. Some of the defect-related barriers impeding twin motion might exceed the maximum magnetic stress provided by the anisotropy energy. As a result, some twin boundaries could not move past the barriers even under very high magnetic field. Specifically, for this sample, a volume fraction of the unfavorable variants of approximately 0.18 was not rearranged; hence, a strain of only 0.05 was realized though the theoretical martensitic strain of 0.06, results.

As expected, the transverse field extends the sample in the strain measurement direction, while the longitudinal field contracts the sample length. It can be observed that MFIS can be obtained more easily when the field is applied along the sample length. Under a longitudinal field, MFIS increases abruptly to full strain once the threshold field of 1 kOe is achieved. On the other hand, with the transverse field, MFIS starts to show up after the threshold field of 1 kOe is reached and then slowly increases and reaches maximum at the field of 3.5 kOe.

The same MFIS measurement was performed on sample TL8-3C. The sample dimensions and chemical composition, shown in Chapter 2, differ slightly from those of TL8-1A. A plot of MFIS-vs.-magnetic field for the sample is shown in Figure 3-2. The maximum MFIS from this sample is approximately 0.045, which is smaller than the maximum MFIS of sample TL8-1A in both directions. Apparently, a volume fraction of approximately 25% of the unfavorable variants still remained due to defect-related twin-boundary pinning. The threshold fields are different for the two field directions. The threshold filed for the longitudinal direction is 1.7 kOe, while that for the transverse direction is 2.4 kOe. Both threshold fields are larger than those of sample TL8-1A. For the longitudinal field, MFIS grows abruptly to maximum after the field is equal to the

threshold field, as is the case in sample TL8-1A. For the transverse field, the MFIS evolution under an applied field is slightly different from TL8-1A. MFIS actually increases abruptly to 0.03 once the threshold field is achieved. Then, after the abrupt rise, it gradually increases with the increasing field similar to the MFIS behavior in TL8-1A. This suggests that the most active twin boundary in TL8-3C is more strongly pinned in its initially set state than is that in TL8-1A.

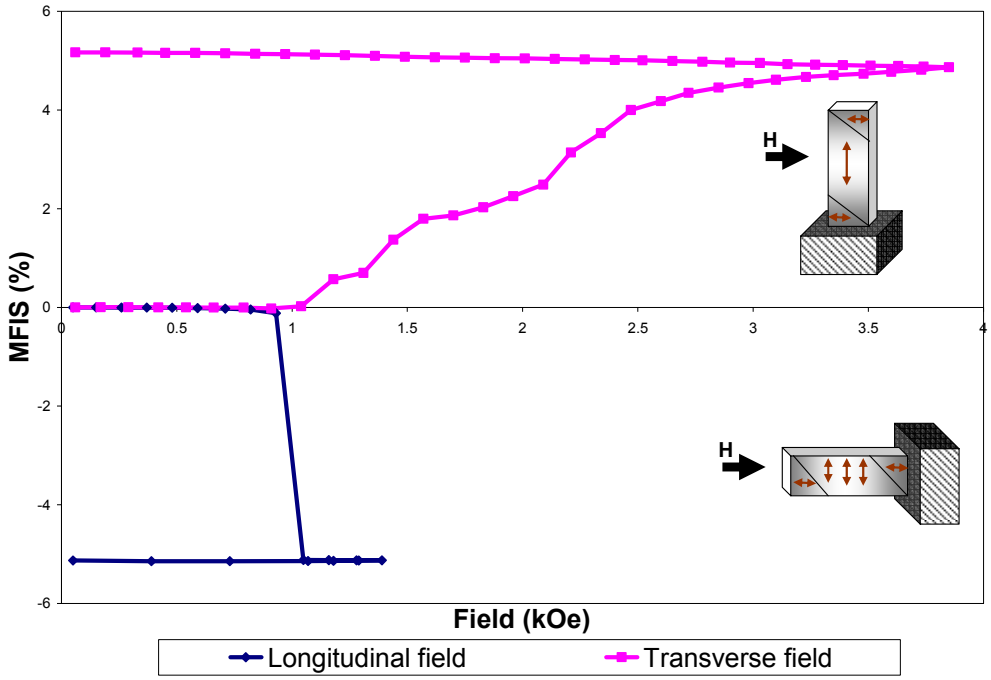

Figure 3-1: Magnetic field induced strain for sample TL8-1A under an applied field along its length (longitudinal field) and a field along its width (transverse field).

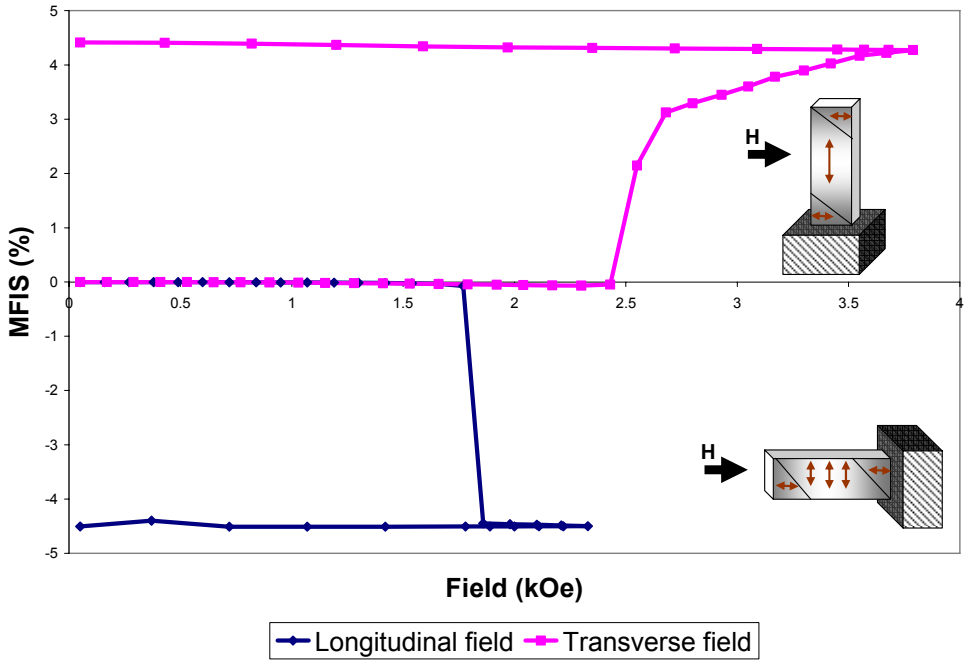

Figure 3-2: Magnetic field induced strain for sample TL8-3C under two different field directions: longitudinal field and transverse field.

So far, the demagnetization effects on the two samples with similar composition but different threshold fields are compared. Next, the demagnetization effect on the FSMA samples with the piezo assist is observed and discussed. As mentioned in Chapter 1, the piezoelectric assist has been shown to help reduce the threshold field [20, 38]. Therefore, in this experiment, the piezo assist is applied in order to reduce the threshold fields of the samples. The piezo assist allows us to study the demagnetization effect on the FSMA samples when their threshold fields are changed by the piezo assist.

A 33-mode piezoelectric stack is attached to one end of the sample such that the direction of the piezoelectric actuation is along the length direction; the samples are free at the other end. A sinusoidal voltage signal oscillating from zero to 30 V is applied across the piezoelectric stack. Even at low drive frequency and voltage, the stack can heat up quickly if driven continuously; therefore, a 10% duty cycle voltage signal is applied to allow the stack to be inactive and cool down for 90% of the operating time. The piezoelectric actuating frequency is varied from 0 Hz to 9 kHz.

The MFIS-vs.-field results with piezoelectric assist for sample TL8-1A under longitudinal and transverse fields are shown in Figure 3-3 and Figure 3-4, respectively. Under both fields, the initial threshold fields are reduced with piezoelectric assist by about 0.5 kOe. For the longitudinal field, MFIS also increases abruptly to its maximum in one step once the field reaches the threshold field, regardless of the magnitude of the threshold field. For example, for a threshold field of 1 kOe, a maximum strain is also achieved at 1 kOe, while, for a 0.5 kOe threshold field, a maximum strain also occurs at 0.5 kOe.

On the contrary, for the transverse field, MFIS behaves differently. Without the piezo assist, MFIS starts at the onset threshold field of 1 kOe and increases to a maximum strain of 4.5% at 3 kOe. With a 5 kHz piezo assist, MFIS starts at the lower onset threshold field of 0.5 kOe and increases to a maximum strain of 4.5% occurs at 3 kOe. Evidently, the onset threshold field is reduced by 0.5 kOe with the piezo assist of 30 $V_{p\text{-}p}$ and 5 kHz. However, for both with and without piezo assist, the maximum strain is completed at large fields ranging from 2.7 to 3.5 kOe. As a result, under transverse field, the maximum MFIS of sample TL8-1A appears to complete at a large magnetic field regardless of the change in the onset threshold field.

The results for TL8-3C are shown in Figure 3-5 and Figure 3-6 for the longitudinal and transverse fields respectively. MFIS under the longitudinal field for this sample behaves similar to sample TL8-1A. The piezo assist of 30 $V_{p\text{-}p}$ and 9 kHz reduces the onset threshold field to 1 kOe. MFIS increases to maximum in one step once the onset threshold field is reached, regardless of the threshold field values.

For the transverse field, the onset threshold field of 2.5 kOe is reduced to 1.5 kOe for 7 kHz piezo assist and 1 kOe for 9 kHz. For 7 kHz piezo assist, after the onset threshold field of 1.5 kOe, MFIS quickly increases to 3% at 1.7 kOe and slowly increases to maximum strain at 3 kOe. For the 9 kHz piezo assist, after the onset threshold field of 1 kOe, MFIS gradually increases to 3% at 1.7 kOe to overlap with the MFIS curve of 7-kHz piezo assist and slowly increases to maximum strain at the field of 3 kOe similar to the result with 7-kHz piezo assist.

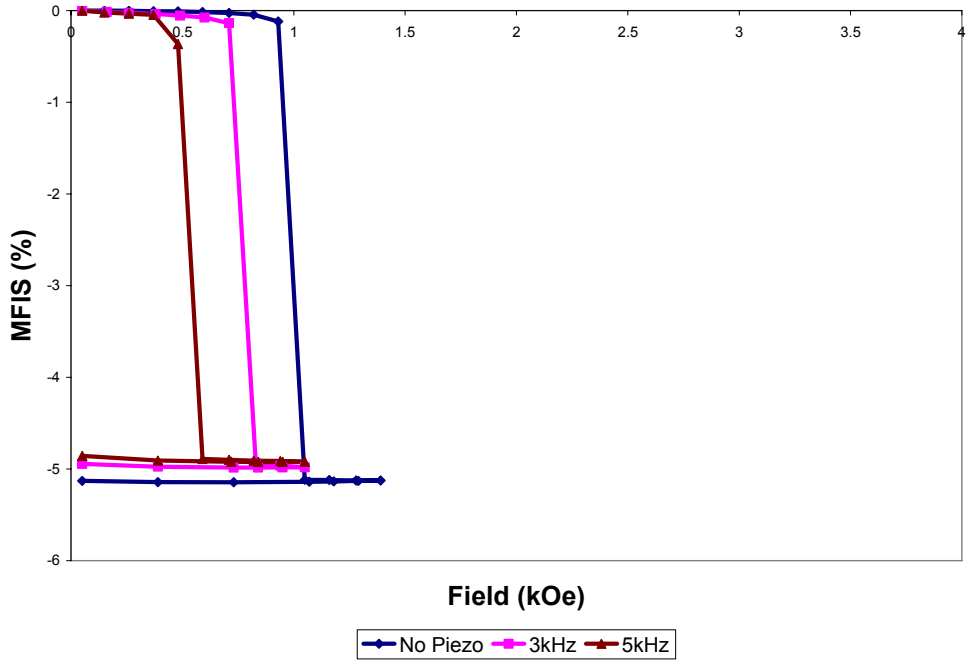

Figure 3-3: Magnetic field induced strain for sample TL8-1A under a longitudinal field. Piezoelectric assists actuating under 30 V_{p-p} and varying frequency (0, 3 and 5 kHz) are applied during the measurement.

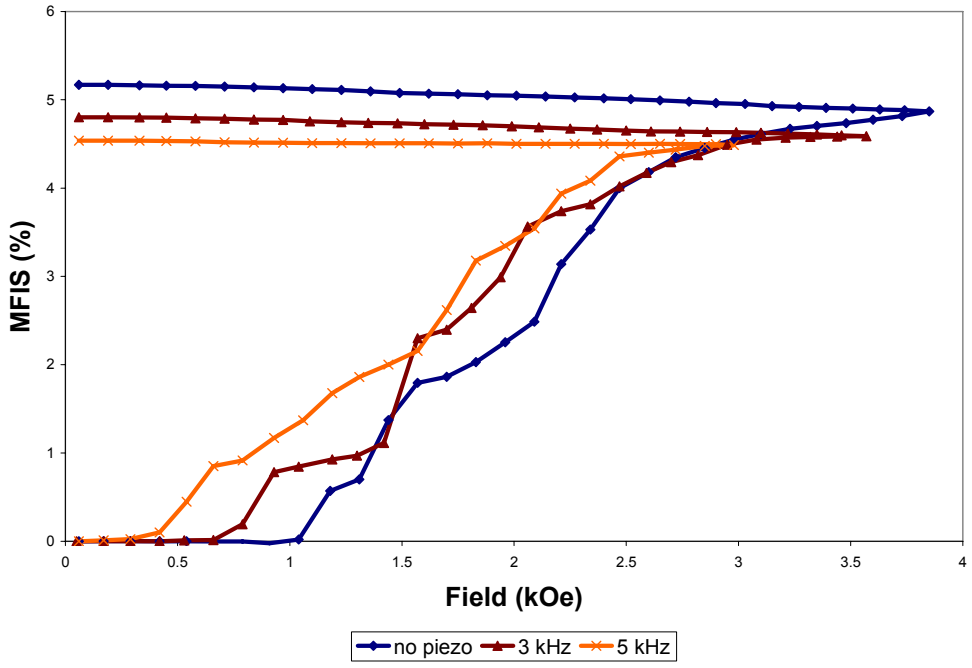

Figure 3-4: Magnetic field induced strain for sample TL8-1A under a transverse field. Piezoelectric actuation under 30 V_{p-p} and varying frequency (0, 3 and 5 kHz) are applied to assist MFIS during the measurement.

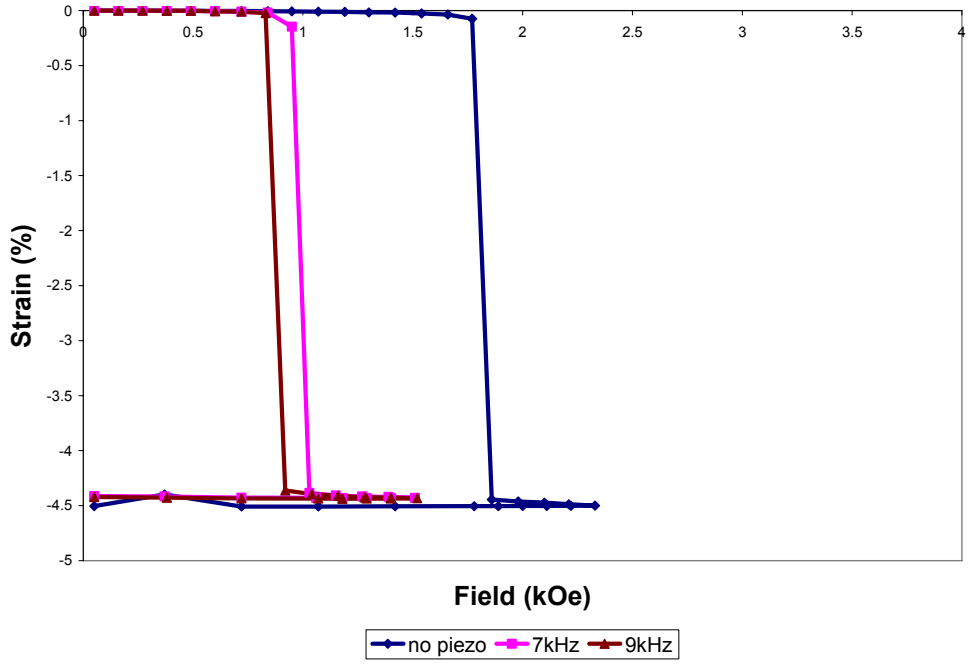

Figure 3-5: Magnetic field induced strain for sample TL8-3C under a longitudinal field. Piezoelectric assist actuating under 30 V_{p-p} and varying frequency (0, 7 and 9 kHz) are applied during the measurement.

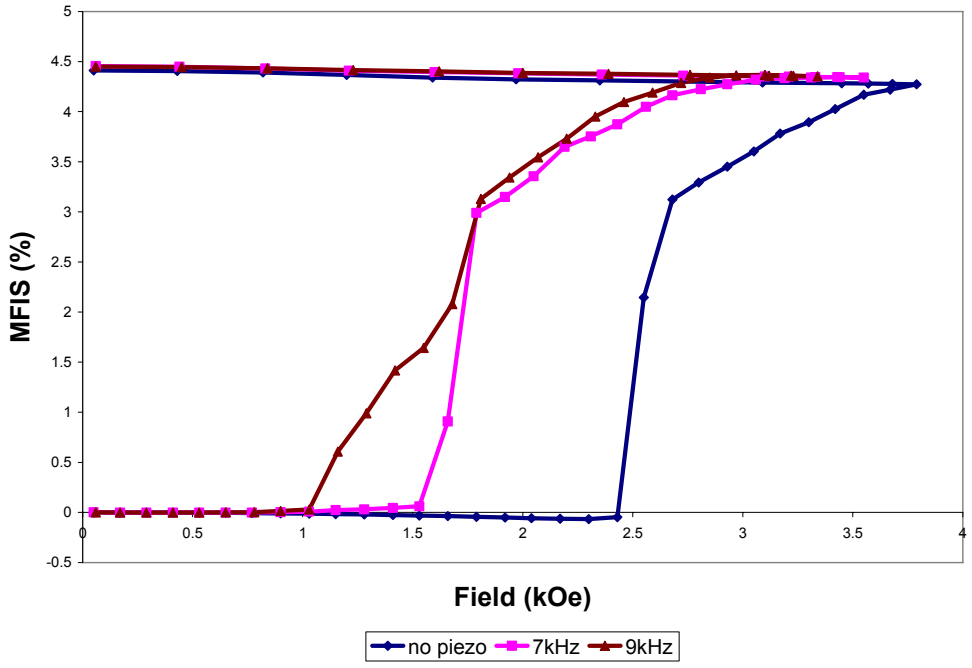

Figure 3-6: Magnetic field induced strain for sample TL8-3C under a transverse field. Piezoelectric actuation under 30 V_{p-p} and varying frequency (0, 7 and 9 kHz) are applied to assist MFIS during the measurement.

3.2 Free Energy Model with Demagnetization Effect

Full field-induced strain is achieved for smaller applied fields in the longitudinal geometry than in the transverse geometry. MFIS curves for the two different field directions are similar to the magnetization curves shown in Figure 1-18, which demonstrates the demagnetization effect on the magnetization process when the field is applied along different directions. In this section, the hypothesis that the demagnetization phenomenon is responsible for different growing rates of MFIS under varying field directions is explored.

Here, we review the simple free energy model of MFIS [17] and consider how it might be modified to account for magnetostatic effects. The demagnetizing field cannot be expressed with simple analytical forms for any shapes other than ellipsoids of revolution. Here we will present a first-order approximation to magnetostatics which brings the free energy model into better agreement with empirical ε-H data.

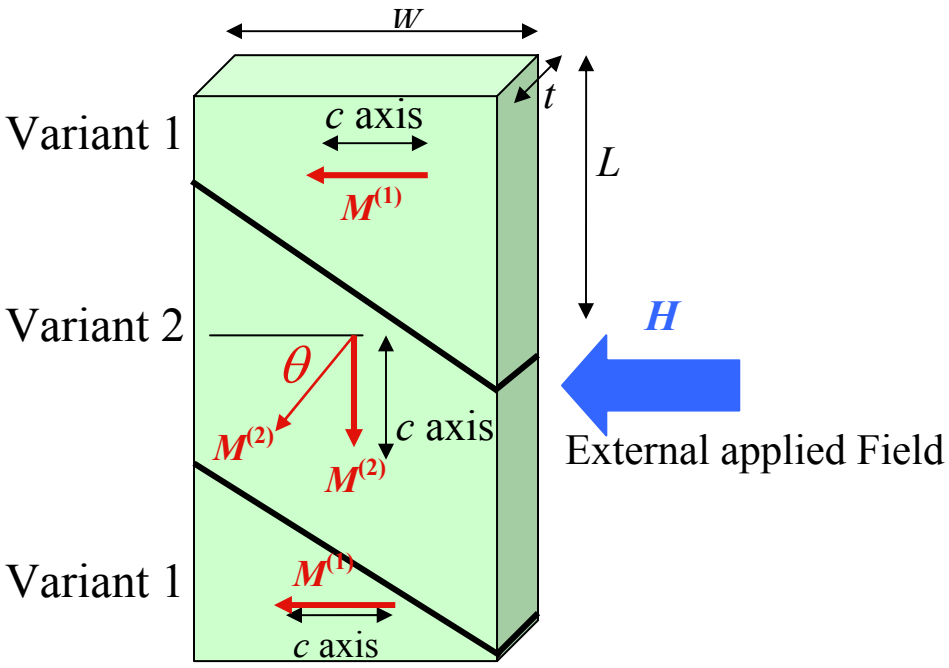

Figure 3-7: An illustration of an FSMA sample composed of two variant types with perpendicular easy axis directions: parallel to an external applied field (Variant 1) and perpendicular to the field direction (Variant 2). As the field increases, variant 1 will grow by moving twin boundary and result in MFIS.

To appreciate the demagnetization effect on this material system, a simple phenomenological free energy model of an FSMA sample composed of two twin variants, as shown in Figure 3-7, is considered and slightly modified by including the demagnetizing field. For simplicity, the new free energy expression, g, begins with Zeeman energy and the magnetocrystalline anisotropy terms, as shown below:

$$g = -f_1 \mu_o M_s H_i^{(1)} - f_2 \left(\mu_o M_s H_i^{(2)} \cos\theta + K_u \cos^2 \theta \right) \quad \textbf{Equation 3-1,}$$

where the first term represents Zeeman energy due to variant 1 (volume fraction f_1), the second and third terms are Zeeman energy and the anisotropy energy in variant 2, (volume fraction $f_2 = 1 - f_1$). The demagnetization field is incorporated into the internal field in the Zeeman energy terms. In the previous model, the internal field, H_i, is considered to be identical to the external field, H_{ext}. In this modification, the internal field is equal to the external field reduced by the demagnetizing field, H_d, $H_i = H_{ext} - H_d$. The demagnetizing field may be approximated as:

$$H_d = N^{(1)}(f_1) M_s, \text{ for variant 1} \quad \textbf{Equation 3-2},$$

$$H_d = N^{(2)}(f_2) M_s \cos\theta, \text{ for variant 2} \quad \textbf{Equation 3-3}.$$

where $N^{(1)}(f_1)$ and $N^{(2)}(f_2)$ are approximate demagnetizing factors for corresponding variants and they depend on the varaints' volume fractions; and the variant rearrangement results in a change in the geometric shape of each variant, which influences the corresponding shape factor. Next, the magnetization rotation in variant 2 is considered to be in equilibrium:

$$\frac{dg}{d\theta} = 0 = f_2 \left(\mu_o M_s H_{ext} \sin\theta - 2 \sin\theta \cos\theta \mu_o N^{(2)}(f_2) M_s^2 - 2 K_u \sin\theta \cos\theta \right) \quad \textbf{Equation 3-4},$$

such that cos θ_{eq} may be derived as a function of H_{ext}, volume fractions, f_i, and the other materials constants.

$$\cos\theta_{eq} = \frac{\mu_o M_s H_{ext}}{2\left(K_u + \mu_o N^{(2)}(f_2) M_s^2\right)}, \qquad \textbf{Equation 3-5.}$$

The total free energy density in Equation 3-1 can be minimized with respect to f_1 to obtain f_1 as a function of an external field to determine the equilibrium fractions of each variant. In order to calculate this free energy minimization, functional forms for $N^{(1)}(f_1)$ and $N^{(2)}(1\text{-}f_1)$ are required. Typically, the demagnetizing factor is strongly shape dependent and, therefore, the required functions are complex and approximate at best. The demagnetizing factor for a general ellipsoid can be approximated as Lt/W^2, where W is the length along the field direction, L and t are the other dimensions perpendicular to the field direction. For the sample considered in this analysis (Figure 3-7), the values of W and t can be approximated as constant, but L is proportional to f_1 (or $1 - f_2$). Therefore, as a first-order approximation, the demagnetizing factors are simply estimated to be linearly dependent on volume fractions: $N^{(1)}(f_1) = N_d f_1$ and $N^{(2)}(1\text{-}f_1) = N_d(1\text{-}f_1)$, where N_d is a demagnetizing factor of a sample with only a single variant of either type. Therefore, N_d is identical for a sample completely composed of either variant 1 or 2. The minimum free energy state must satisfy the equation:

$$\frac{\partial g}{\partial f_1} = 0 = -\mu_o M_s H_{ext}\left(1 - \cos\theta_{eq} + (1-f_1)\frac{\partial \cos\theta_{eq}}{\partial f_1}\right) + 2\mu_o N_d M_s^2 f_1 - 2\mu_o N_d M_s^2 (1-f_1)\left(\cos^2\theta_{eq} - (1-f_1)\cos\theta_{eq}\frac{\partial \cos\theta_{eq}}{\partial f_1}\right) - K_u\left(\cos^2\theta_{eq} - 2(1-f_1)\cos\theta_{eq}\frac{\partial \cos\theta_{eq}}{\partial f_1}\right), \qquad \textbf{Equation 3-6.}$$

It is difficult to separate f_1 out of the right-hand side of Equation 3-6 in order to express the function $f_1(H_{ext})$, because terms of both $\cos(\theta_{eq})$ and $\partial\cos(\theta_{eq})/\partial f_1$ are present. As a result, numerical software is required to solve for the equilibrium volume fraction under given external field. Alternatively, we may simplify the equation by assuming that $\cos(\theta_{eq})$ does not depend strongly on f_1. With this assumption, f_1 is given by:

$$f_1 = \frac{\mu_o M_s H_{ext}\left(1-\cos\theta_{eq}\right)+\left(2\mu_o N_d M_s^2 + K_u\right)\cos^2\theta_{eq}}{2\mu_o N_d M_s^2\left(1+\cos^2\theta_{eq}\right)}, \qquad \textbf{Equation 3-7.}$$

The function $f_1(h)$, where h is equal to $\cos(\theta_{eq})$, under varying N_d is plotted in Figure 3-8 below. When the demagnetizing factor is equal to 0.35, the model of Equation 3-7 with demagnetization effect shows a similar $f_1(h)$ behavior to the free energy model from [17]; variant 1 grows completely to 1 (resulting in MFIS of 6%) and then saturates. When the demagnetizing factor is lower, 6% MFIS can be achieved at lower field. On the other hand, when the demagnetizing factor is near its theoretical maximum of 0.5, variant 1 may never grow completely even at field equal or above the anisotropy field H_a.

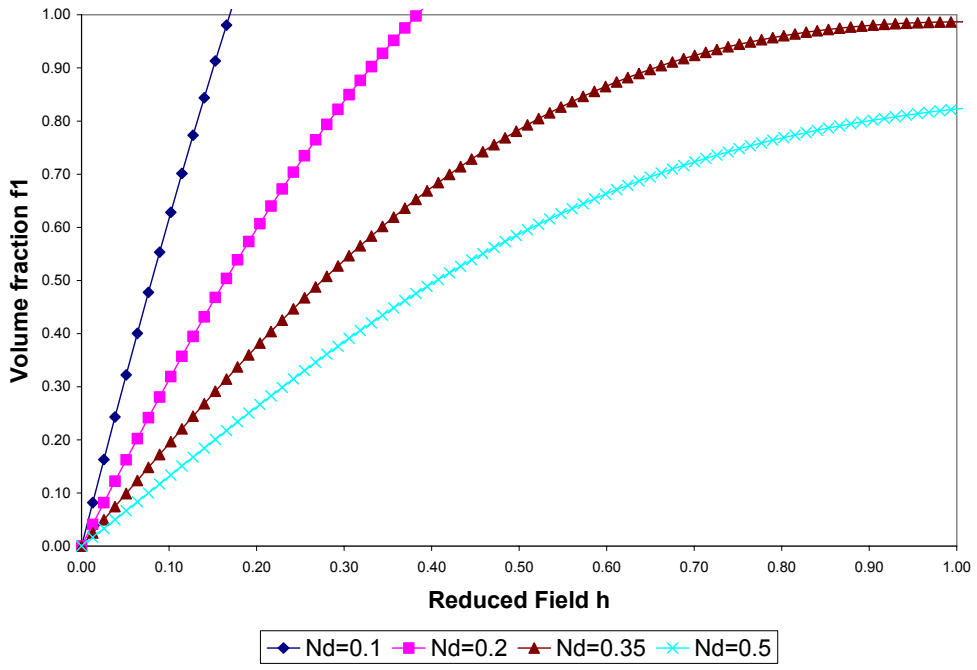

Figure 3-8: Volume fraction of variant 1 as a function of a reduced field h under varying demagnetizing factors. For other materials constants, K_u = 0.19 MJ/m^3 and M_s = 484 kA/m.

It should be noted that the predicted form of $f_1(h)$ shown above assumes defect-free single crystals in which twin boundary motion can be initiated once $H > 0$. A simple illustration of the defect-pinning effect is shown in Figure 3-9. A simple defect-pinning

effect may be included in the curve by introducing a threshold field required to overcome defect-pinning energy barriers. For $H > H_{th}$, the twin boundary should be able to move with relative ease up to its equilibrium value of f_1. In reality, defects are distributed randomly throughout the materials. Therefore, after the first defect-pinning is overcome, a twin boundary may move a distance then get pinned by another defect. Therefore, a threshold characteristic, where variant 1 grows slowly, and sometimes step-wise growth with increasing field may be observed in experimental measurements, as in Figure 3-4 and Figure 3-6.

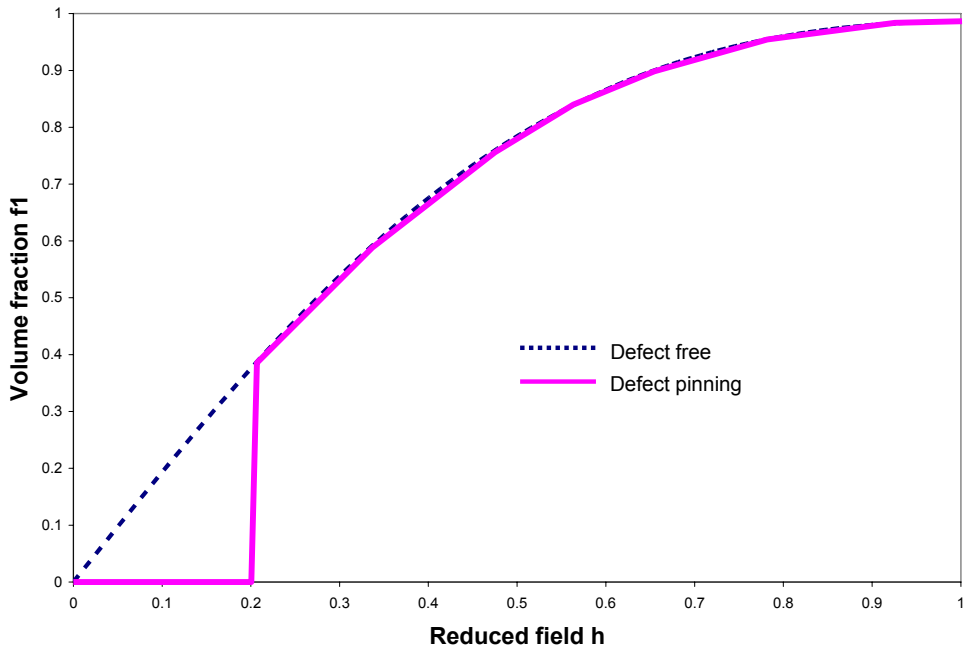

Figure 3-9: Comparison between the growth of variant 1 under applied field with and without defect pinning. The demagnetizing factor is 0.35. A reduced threshold field, required to overcome a defect-pinning, is assumed to be equal to 0.2.

3.3 Discussion

Both empirical data and a theoretical model have shown how the demagnetization effect significantly influences the growth of MFIS under external field. In this section,

the theoretical model will be used to facilitate the understanding of empirical results of MFIS behavior under two different field directions.

For the transverse field, both sample TL8-1A and TL8-3C have similar dimensions and, therefore, should have nearly equal demagnetizing factors. Moreover, the anisotropy energy should be the same for both samples because the compositions are similar. As a result, similar demagnetization effects on MFIS are observed in both samples (Figure 3-1 and Figure 3-2). In both figures, the maximum MFIS is attained at similar field of 3.5 kOe, even though the onset threshold fields are considerably different by 1.5 kOe. A difference in the threshold field may be explained by variation in defect-pinning strength, defect density and defect distribution inside the samples [16, 28].

The piezoelectric assist does decrease the threshold field by facilitating twin boundary motion to overcome the defect-pinning at lower field. However, the piezo assist does not have any influence on the demagnetization effect. As clearly shown in Figure 3-4, the threshold field of sample TL8-1A is reduced by 0.5 kOe, but a field of 3 to 3.5 kOe is required to achieve a maximum MFIS. A departure from the theoretical prediction may appear in the results for sample TL8-3C (Figure 3-6); the threshold field is reduced by as much as 1.5 kOe, while the maximum MFIS is achieved at approximately 3 kOe, 0.5-kOe lower than the original required field without piezo assist. As mentioned above, the demagnetizing factor strongly depends on the shape dimensions of both variant 1 and 2; therefore, a change of the demagnetizing factor as a function of variant volume fraction may be more complex than the linear relationship assumed here. As a result, a reduction in a threshold field by 1.5 kOe may actually cause a change in $N^{(1),(2)}(f_1)$.

The MFIS as a function of the transverse field as described by the free energy model is then plotted and compared to the empirical data for both samples (Figure 3-10 and Figure 3-11). The anisotropy energy used in the model curve is 0.16 MJ/m^3 and the saturation magnetization is 484 kA/m. The demagnetizing factor (N_d) used in the model is 0.18, which is about half of the typical demagnetizing factor of an ellipsoid-shape sample with a similar length/width ratio. From [41], a demagnetizing factor, for an ellipsoid-shape with a length-to-width ratio of 4 and a field applied along the width

direction, is approximately 0.4. However, in an ellipsoid, the magnetization field is uniform and, hence, a strong demagnetizing field is expected to be present uniformly throughout the sample. However, for a magnetized sample that is not an ellipsoid, N_d is not uniform and can only be approximated by volume-averaged fields. The N_d of a magnetized non-ellipsoidal FSMA sample is even more complicated, because, the variant rearrangement further modifies the demagnetizing field as illustrated in Figure 3-12. In Figure 3-12, at low fields, H_i is too small to rotate the magnetic moment in the unfavorable variant with an easy axis perpendicular to the field direction, but large enough to move domain walls in the favorable variant with an easy axis parallel to the field. A positive magnetic polarity is formed on the right side of the favorable variant and a negative polarity on the left side. The magnetic surface charge results in a small demagnetizing field opposing the applied field. It should be noted that we only consider the magnetic polarity that will result in the demagnetizing field opposing the applied field; therefore, the polarities at the top and bottom of the sample are not considered because they generate a demagnetizing field perpendicular to the applied field direction. For the intermediate field in Figure 3-12, the field is large enough to rotate the magnetic moments in the unfavorable variant and also to move twin boundaries for variant rearrangement to increase the volume fraction of the favorable variant. A positive magnetic pole density is formed at the right side and top of the favorable variants, while a negative polarity is formed at the left side and bottom of the favorable variant. The more-complex surface polarization results in a stronger demagnetizing field opposing the applied magnetic field. For the high field in Figure 3-12, the field is large enough to saturate the magnetic moments to align them in the field direction and to complete twin boundary motion. A positive magnetic surface charge is formed on the right side of the sample and a negative polarity on the left side. The surface polarization reaches maximum in this high-field case and results in the maximum demagnetization effect against the applied field. Clearly, the demagnetizing field increases nonlinearly with an increasing field.

The estimation of the volume-average N_d as a function of the applied magnetic field requires an extensive numerical simulation such as the finite-element method, which

is demonstrated in [46]. The actual demagnetization effect in a rectangular-shaped sample is expected to be smaller than that in an ellipsoid. For the two samples studied in this work, the volume-average N_d for a transverse field is estimated from the experimental data and the free energy model to be about half of the N_d in a uniformly-magnetized sample. With N_d of 0.18, the maximum MFIS is achieved at the field of 3 kOe. Once the threshold field is exceeded, the experimental MFIS in both samples seems to increase sharply to catch up with the predicted equilibrium curve. Then, the experimental data slowly increases with the field, once they approach the calculated equilibrium curve.

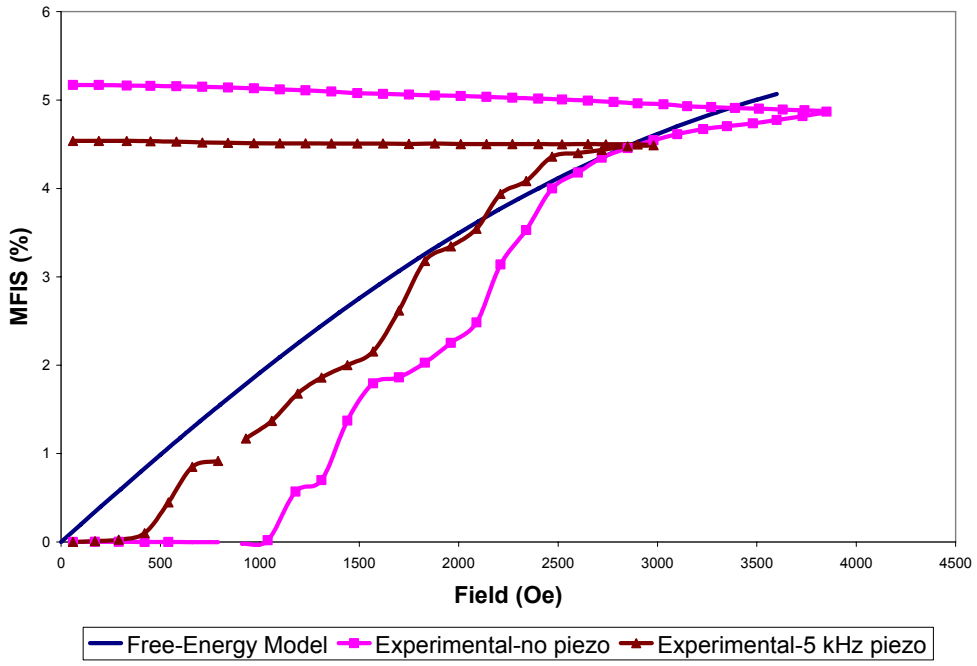

Figure 3-10: Comparison between MFIS according to the free-energy model with demagnetization effect and the experimental MFIS data for sample TL8-1A under a transverse field.

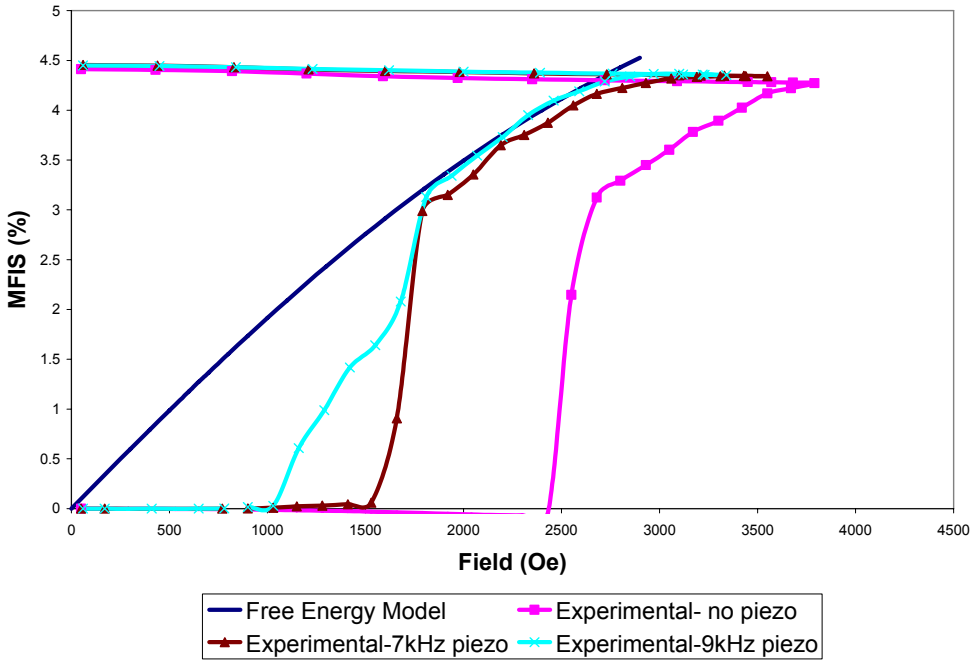

Figure 3-11: Comparison between MFIS according to the free-energy model with demagnetization effect and the experimental MFIS data for sample TL8-3C under a transverse field.

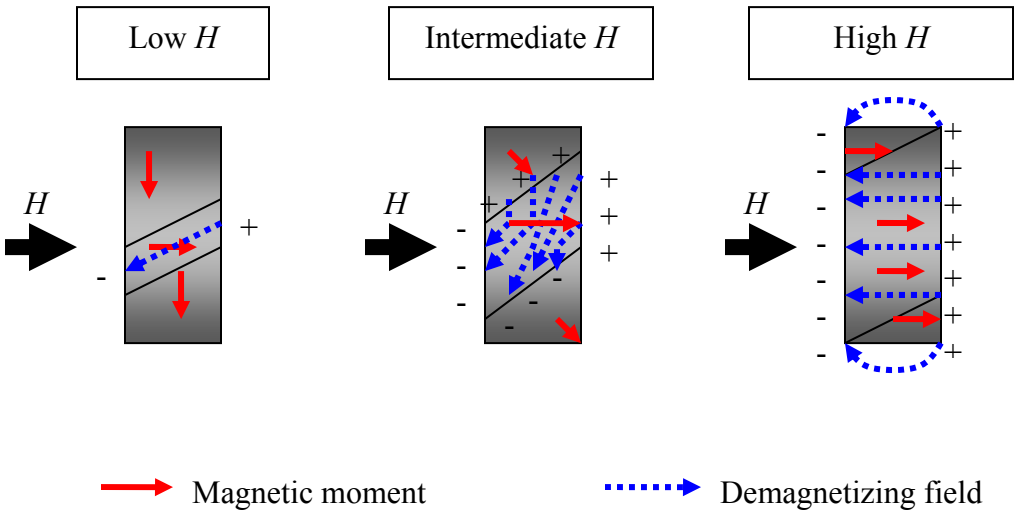

Figure 3-12: Illustration of evolutions of variant rearrangement, the magnetic moments and demagnetizing field inside a typical FSMA sample over increasing applied magnetic field.

For a longitudinal field, a similar comparison between the model and experimental results for sample TL8-1A is made in Figure 3-13. K_u and M_s are the same

as above. N_d for a magnetization along the length direction is 0.05, which is about half the magnitude of N_d in an ellipsoid. The model curve (Figure 3-13) shows that a maximum MFIS of 5% is reached at a low field of approximately 600 Oe due to a low N_d value. Without piezo assist, a required threshold field is about 950 Oe. Therefore, once the defect-pinning barrier is overcome, variant 1 grows completely in one step. When the piezoelectric assist reduces the threshold field, the field is still high enough to complete MFIS in one step. The minimum threshold field, to which the piezoelectric is able to decrease, is 500 Oe.

For a longitudinal field in sample TL8-3C, a similar behavior to sample TL8-1A is expected because the model is identical with the same N_d, K_u and M_s. The threshold field without piezoelectric assist is as large as 1.7 kOe, and the minimum threshold field reduction by piezoelectric is 500 Oe. Therefore, a one-step MFIS development is expected once the threshold field is attained.

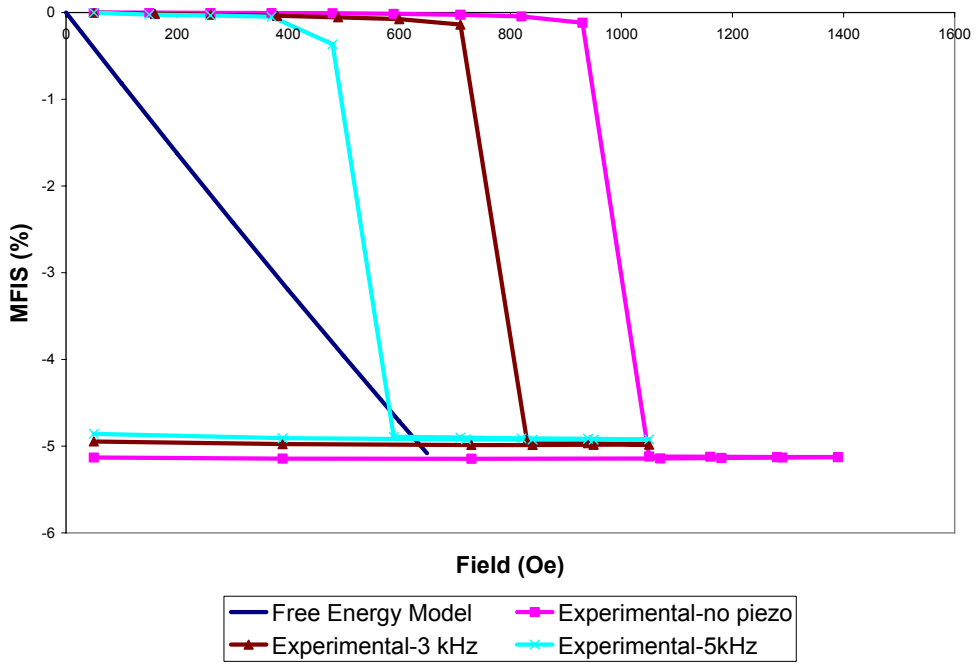

Figure 3-13: Comparison between MFIS according to the free-energy model with demagnetization effect and the experimental MFIS data for sample TL8-1A under an longitudinal field.

CHAPTER 4

PIEZOELECTRIC-ASSIST EFFECTS

Twin boundary motion in FSMAs may be induced by either the application of a magnetic field or a mechanical stress. Under application of a magnetic field, a difference in free energy between two variants, separated by a twin boundary, results in a stress on the twin boundary. When the magnetic stress is large enough to overcome the pinning centers coincident with a twin boundary, then twin boundary motion occurs. The magnetic field at which twin boundary motion commences is called the *threshold field*. Under application of a mechanical stress, the material may undergo plastic strain by mechanical stress-induced twin boundary motion. The yield stress is then called the *twinning-yield stress*.

In this chapter, the effects of piezoelectric assist on the mobility of twin boundary motion are reported and discussed. Specifically, the reductions of the threshold field and the twinning-yield stress, due to application of an acoustic wave generated by a piezoelectric transducer, are measured and analyzed. The experimental observations of piezo assist on FSMA actuation are analyzed and explained in the context of stress-wave theories.

4.1 Experimental Results

4.1.1 Threshold Field Measurement

MFIS of sample TL8-1A under a quasi-static field without external stress was measured under varying amplitude and frequency of piezo assist. Only a magnetic field along the sample's length direction was applied for the measurements. The sample was magnetically reset by applying a transverse field up to 8 kOe before every measurement. A 33-mode piezoelectric stack was attached to one end of the sample such that the direction of the sinusoidal-longitudinal acoustic waves was along the length direction (parallel to the field direction). Even at low drive frequency and voltage, the stack can heat up quickly if driven continuously; therefore, a 10% duty cycle voltage signal was applied to allow the stack to be inactive and cool down for 90% of the operating time. The piezoelectric actuating amplitude is proportional to the peak-to-peak voltage ($V_{p\text{-}p}$) applied across the stack (Figure 2-2). $V_{p\text{-}p}$ was varied from 10 to 50 V. The piezoelectric actuating frequency was varied from 200 Hz to 20 kHz depending on the applied $V_{p\text{-}p}$. For high $V_{p\text{-}p}$, the stack may heat up swiftly even at low frequency; as a result, the maximum frequency that could be used is lower for higher applied $V_{p\text{-}p}$.

Figure 4-1, Figure 4-2 and Figure 4-3 show some results of MFIS-vs.-field for sample TL8-1A at drive voltage of 10, 30 and 40 $V_{p\text{-}p}$, respectively. For 10 V, the maximum drive frequency can be as high as 22 kHz, while the temperature rise of the stack remains within 1 ^{o}C. The maximum frequency for 40 V is only 7 kHz. Threshold field data are extracted from these plots. The threshold field is defined to be an average of the fields at which the twin boundary motion begins and completes, as the MFIS grows to maximum in a one-step increment of the field. The plots of the threshold field as a function of piezoelectric-actuating frequency for given $V_{p\text{-}p}$ varying from 10 to 40 V are shown in Figure 4-4.

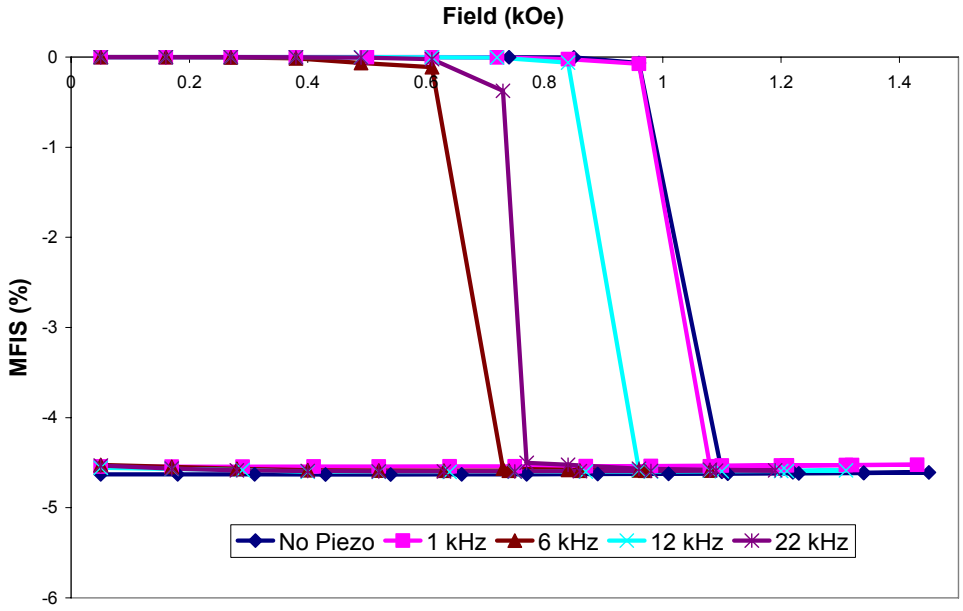

Figure 4-1: MFIS as a function of field under a piezoelectric-driven peak-to-peak voltage of 10 V and varying piezoelectric-actuating frequency, for sample TL8-1A.

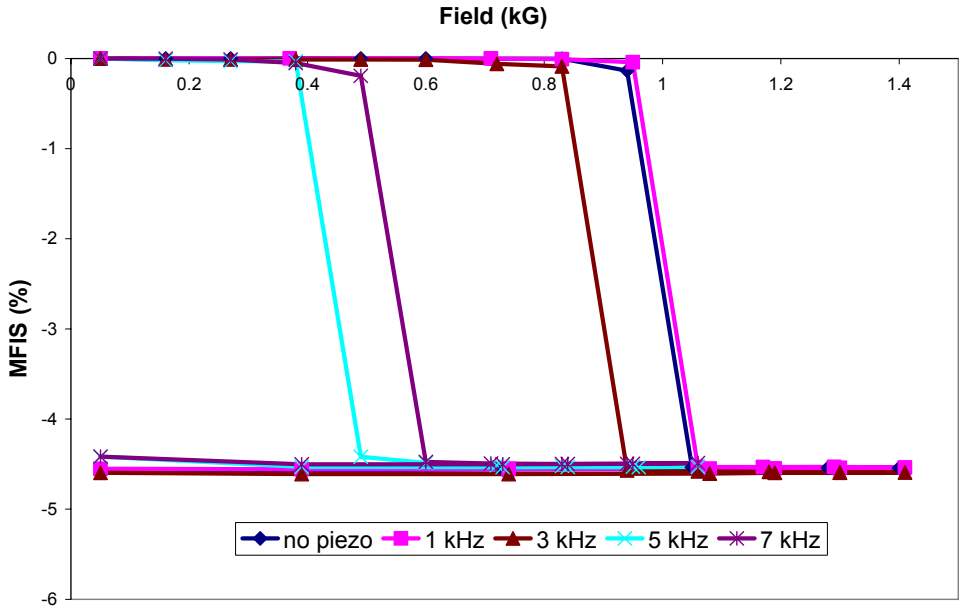

Figure 4-2: MFIS as a function of field under a piezoelectric-driven peak-to-peak voltage of 30 V and varying piezoelectric-actuating frequency, for sample TL8-1A.

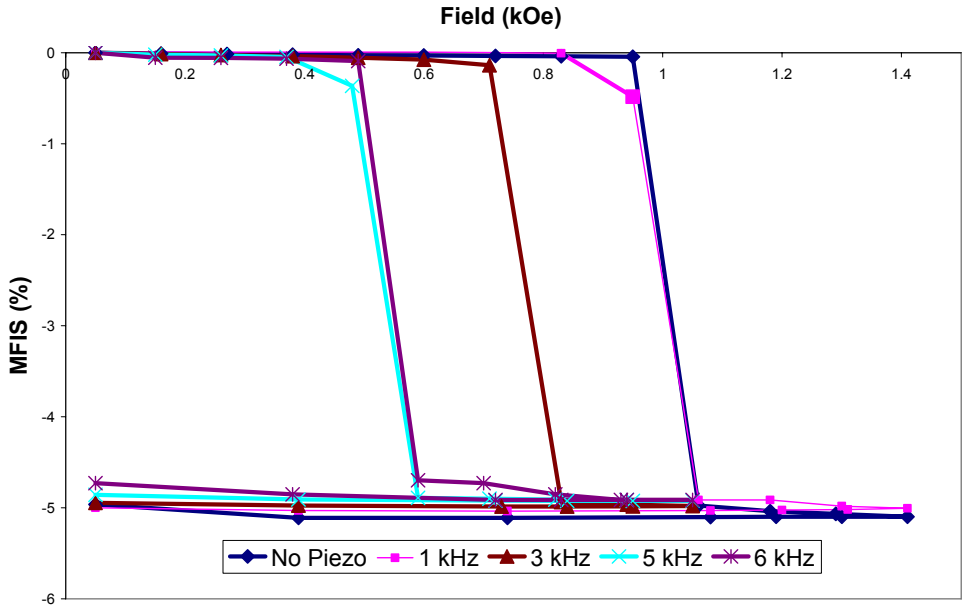

Figure 4-3: MFIS as a function of field under a piezoelectric-driven peak-to-peak voltage of 40 V and varying piezoelectric-actuating frequency, for sample TL8-1A.

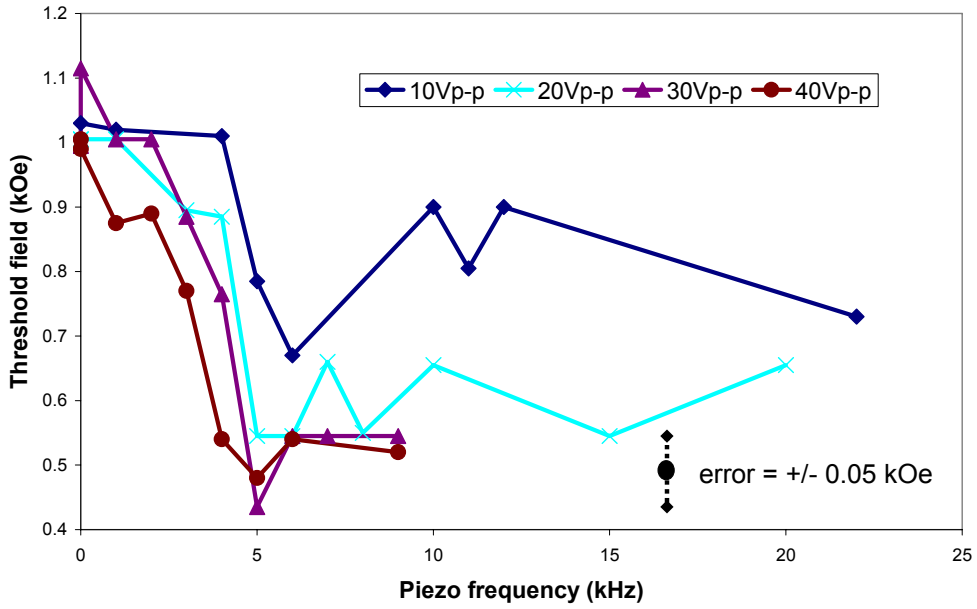

Figure 4-4: Threshold field of sample TL8-1A as a function of piezoelectric-actuating frequency for given peak-to-peak voltage applied across the piezoelectric stack.

From Figure 4-4, the initial threshold field of sample TL8-1A, measured with no piezo assist, is approximately 1 kOe. For 10-V piezoelectric assist, when the frequency increases from zero to 4 kHz, the threshold field reduces slightly. The threshold field appears to decrease considerably to a minimum value of approximately 0.7 kOe when the frequency is in the frequency range between 5 – 6 kHz. The total reduction in a threshold field at this frequency range is 0.3 kOe for a 10-V piezoelectric assist.

For higher piezo-actuating amplitudes, increasing frequency shows a substantial reduction of the threshold field. Similar to 10-V, the minimum threshold fields are shown in the region of 5 – 6 kHz. The maximum reductions for these peak-to-peak voltages are similarly in the region between 0.45 – 0.55 kOe. For 20-V, when the frequency is above 6 kHz, the threshold field does not decrease further and appears to fluctuate between 0.68 and 0.55 kOe. For 30-V and 40-V, increasing the piezo frequency beyond 6 kHz does not affect the threshold field much; it appears to be stable around 0.55 kOe.

A similar threshold field measurement was made for sample TL9-1A; however, only 30 $V_{p\text{-}p}$ piezo-assistance at varying frequencies is applied (Figure 4-5). The composition and dimension of this sample are slightly different from TL8-1A (see Table 2-1 and Table 2-2). The initial threshold field of this sample is twice as large as that of sample TL8-1A. At the maximum applied frequency of 9 kHz, a maximum threshold field reduction of about 1 kOe is observed.

The results for samples TL8-1A and TL9-1A seem to show a difference in the degree of the piezoelectric effect on good samples (low threshold field) and inferior ones (high threshold field). Clearly, the latter ones are deemed poorer, because they require a higher threshold field to achieve MFIS possibly due to high defect concentration (discussed in Section 1.5). For the low-threshold field sample TL8-1A, the piezoelectric assist reduces the threshold field by at most 0.5 kOe and does not decrease the field any further even at high frequency. On the other hand, for sample TL9-1A, the piezo assist reduces the field by 1 kOe at 9 kHz and it would be likely able to reduce the field further if higher frequency could be applied without overheating the sample.

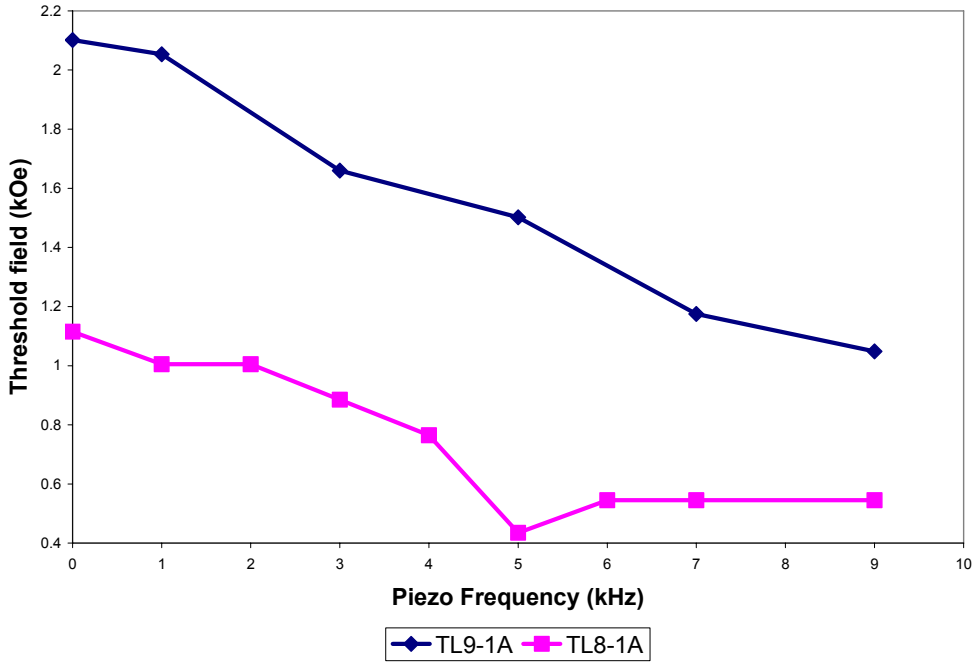

Figure 4-5: Threshold field as a function of piezoelectric-driven frequency at peak-to-peak voltage of 30 V for sample TL9-1A and TL8-1A.

4.1.2 Twinning-Yield Stress Measurement

Stress-strain data were taken on samples TL8-1A and TL9-1A. A compressive stress was then applied along the samples' length direction. The samples were magnetically set in an extended state by an applied transverse field of 8 kOe. The 33-mode piezoelectric stack was attached to one end of the sample; as a result, its actuation direction was along the sample length direction.

The sample stress-strain data for the samples TL8-1A and TL9-1A under different piezo-actuating parameters are displayed in Figure 4-6 and Figure 4-7 respectively. Sample TL8-1A has lower twinning-yield stress than sample TL9-1A by about a factor of 2, which agrees with the relative magnitudes of both samples' magnetic threshold fields. Typically, for an ideal plastic material, the plastic range of a stress-strain curve is perfectly flat, so full plastic strain can be obtained in a one-step increment of stress. Therefore, the twinning-yield stress is typically defined to be measured at the onset of strain. However, in practice as shown in the figures below, full plastic strain does not

complete in one-step. The stress magnitudes of the onset and full strains are observably different. This is due to the fact that there is a distribution of the strength of the obstacles that impede twin boundary motion. As a result, in this chapter, the twinning-yield stress is defined to be equal to a stress required to achieve a 2% strain. This defined twinning-yield stress magnitude should be comparable to the average strength of the defect pinning. The twinning-yield stresses without piezoelectric assist are then 0.4 and 0.7 MPa for samples TL8-1A and TL9-1A respectively. The piezoelectric assist evidently facilitates twin boundary motion because the twin yield-stress decreases with increasing piezo frequency. The twin-yield stresses are reduced by 0.2 and 0.4 MPa for TL8 an dTL9 accordingly.

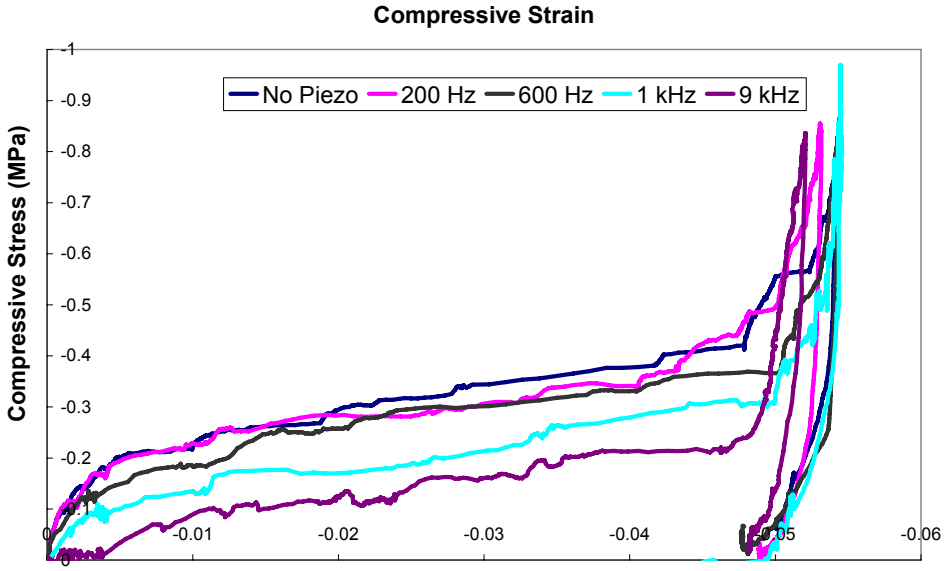

Figure 4-6: Stress-vs-strain data for sample TL81A under an application of piezoelectric actuation with 30 $V_{p\text{-}p}$ and varying frequency.

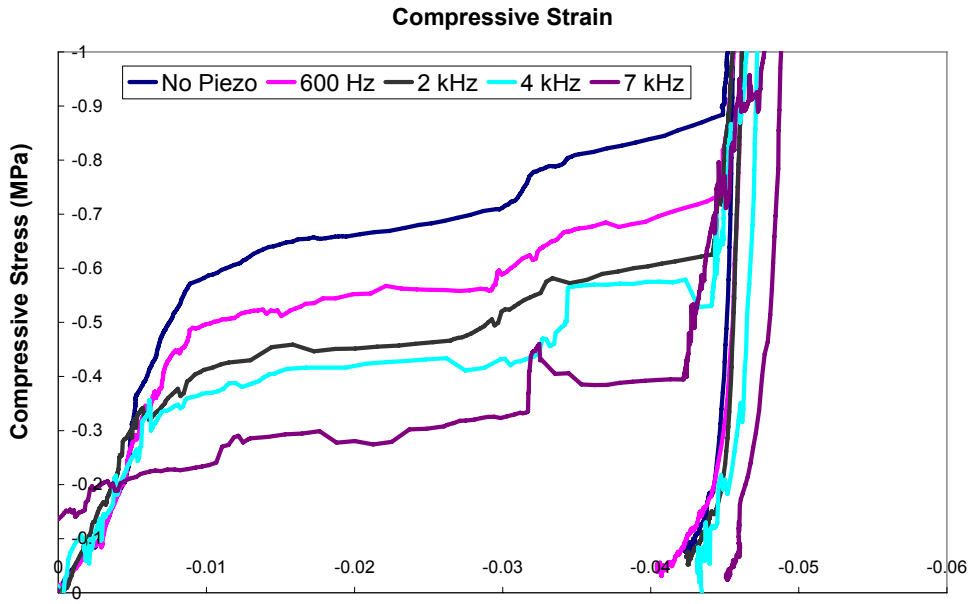

Figure 4-7: Stress-vs-strain data for sample TL9-1A under an application of piezoelectric actuation with 30 $V_{p\text{-}p}$ and varying frequency.

The reduction in twinning-stress under different piezo-actuating frequencies and voltages for samples TL8 and TL9 are plotted in Figure 4-8 and Figure 4-9 respectively. For sample TL8, at 10 $V_{p\text{-}p}$, the maximum stress reduction of 0.1 MPa is achieved in the region between 2 – 5 kHz and increasing frequency beyond 5 kHz does not have any further effect. For 30 $V_{p\text{-}p}$, most of the stress reduction of 0.2 MPa occurs by 1 kHz, then the twinning stress decreases gradually with increasing piezo frequency. For 50 $V_{p\text{-}p}$, the yield stress decreases steadily to 0.17 MPa up to 1 kHz; the yield stress remains essentially constant for frequencies higher than 1 kHz. The maximum reduction for 50 $V_{p\text{-}p}$ is 0.23 MPa.

For sample TL9-1A (Figure 4-9), the yield stress is also reduced fairly uniformly with piezo frequency by 0.1 MPa by 10 $V_{p\text{-}p}$ piezo-assistance. For 30 $V_{p\text{-}p}$, the yield stress decreases to 0.4 MPa at 1 kHz and then 0.3 MPa at 5 kHz. Increasing frequency beyond 5 kHz does not reduce the yield stress further. The maximum stress reduction is approximately 0.4 MPa. For 50 $V_{p\text{-}p}$, the stress decreases to 0.25 MPa at 3 kHz and then

fluctuates around 0.3 MPa as frequency increases to 5 kHz. The maximum stress reduction is 0.45 MPa.

It should be noted that, for 10 $V_{p\text{-}p}$, the maximum piezo-assist effects on both samples are similar, while, for $V_{p\text{-}p}$ above 10 V, a larger maximum stress reduction is observed in sample TL9-1A. This difference agrees with the observation on the magnetic threshold field that the piezo assist is exploited more effectively for inferior samples. For inferior samples with high defect concentration, the piezo assist helps to overcome the defect barrier to a large extent; this results in large reductions in the magnetic threshold field and the twinning yield stress. For superior samples, there are fewer and/or less potent defects for the piezo assist to neutralize; therefore, small reductions in the threshold field and the twinning stress are obtained.

It is noteworthy that the maximum piezo-assist effect takes place at different frequency levels for the *yield stress* and the *threshold field*. The piezo assist at high voltage has maximum effect on the threshold field at frequencies in the 4 – 5 kHz range, while the maximum yield-stress reduction is observed in the frequency range of 1 – 2 kHz. Yet, for 10 V, the piezo assist has a similar effect on both the threshold field and the yield stress; it slowly reduces the field or stress as frequency increases without reaching a minimum. For voltages above 10 V, both threshold field and the twinning stress do not decrease significantly with increasing frequency beyond 4 – 5 kHz.

The initial threshold field of sample TL9-1A is 2.1 kOe, which is approximately twice as high as that of sample TL8-1A (1 kOe). The corresponding twinning stress of sample TL9 (0.7 MPa) is also approximately twice as large as the stress of sample TL8 (0.4 MPa). Therefore, this empirical observation suggests that the equivalent stress output from the FSMA sample generated by a magnetic field of 1 kOe would be approximately 0.4 MPa. This measured magnetic equivalent stress agrees well with the calculated magnetic equivalent stress from [33]. The maximum reduction of the threshold field of sample TL8-1A with piezo assist is approximately 0.5 kOe, which should, therefore, be equivalent to a mechanical stress of 0.2 MPa. The maximum twinning-stress reduction for sample TL8-1A is measured to be 0.23 MPa, which is in good agreement with the equivalent stress stated above.

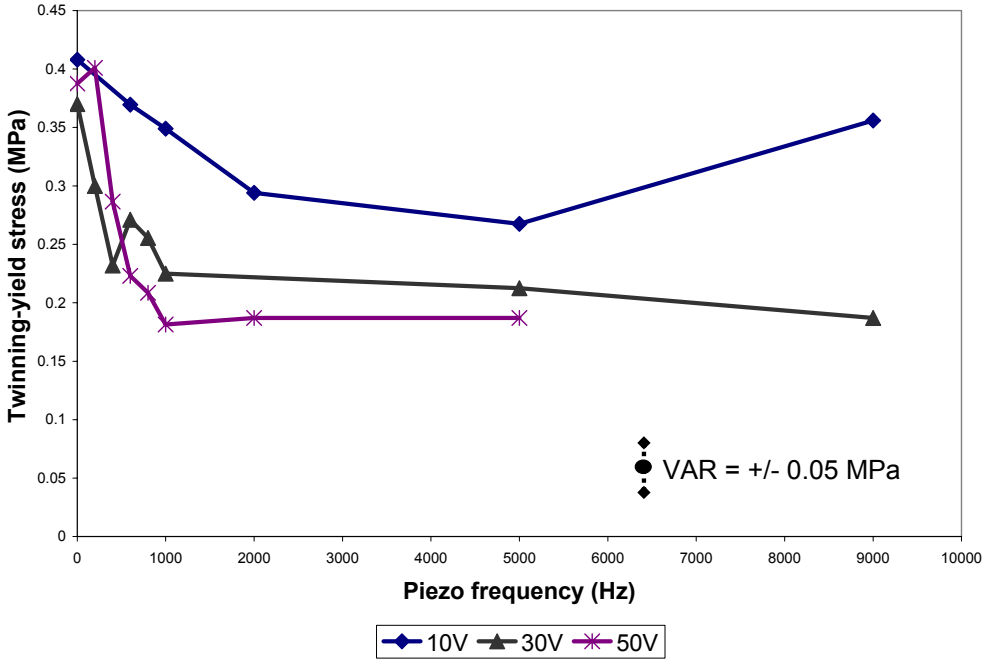

Figure 4-8: A reduction in the twinning-yield stress by piezoelectric assist with varying piezoelectric-actuating frequency and amplitude for sample TL8-1A.

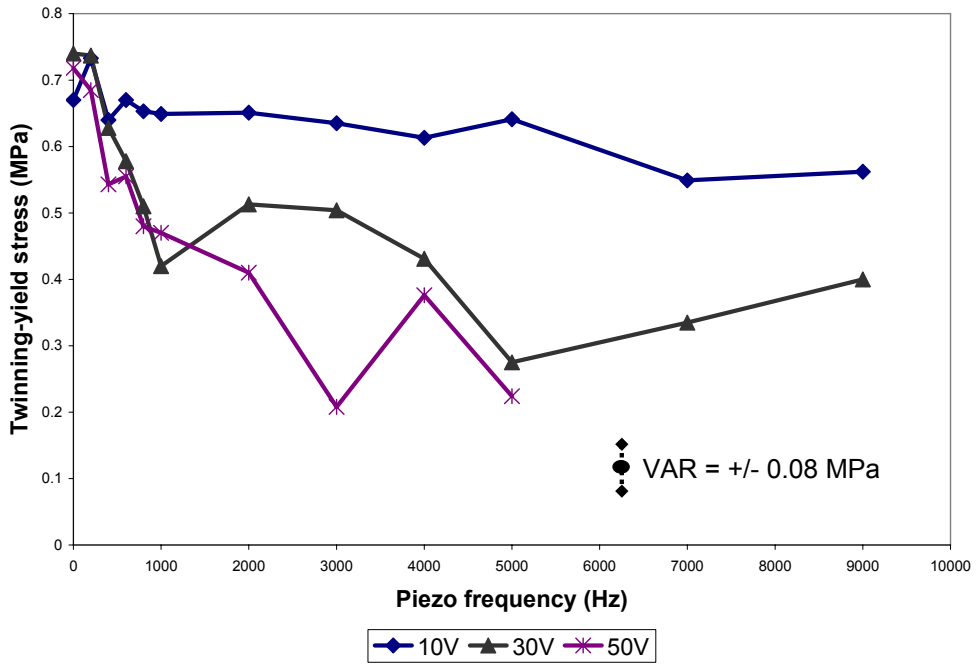

Figure 4-9: A reduction in the twinning-yield stress by piezoelectric assist with varying piezoelectric-actuating frequency and amplitude for sample TL9-1A.

4.2 Stress Waves in Solids

The results above suggest that the piezo assist delivers extra energy into the FSMA sample so that the twin boundary motion becomes easier to initiate. The extra energy from the piezoelectric vibration is believed to travel in a form of the longitudinal stress wave that is transmitted to the FSMA sample. In this section, the theory of stress waves in solid media is discussed to aid our understanding of the piezoelectric's role in enhancing twin boundary mobility.

4.2.1 Governing Wave Equation

The governing equation of wave propagation in solids can be derived by solving the basic equations of motion and elasticity [47-50]. Consider a small section, dx, in a thin bar with uniform thickness along the bar as shown in Figure 4-10.

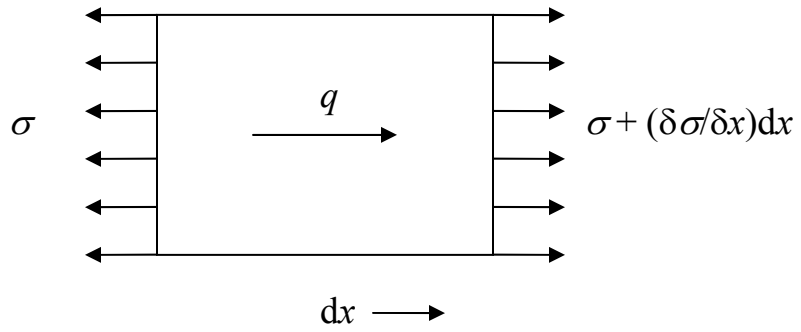

Figure 4-10: An illustration of stresses and body force distributions on a differential section of a thin rod of uniform thickness.

A dynamic stress field $\sigma(x,t)$ varying over distance and time is present in the rod. A body force density $q(x,t)$ may also be present. The longitudinal displacement is given by $u(x,t)$. The equation of motion in the x direction is then:

$$-\sigma A + \left(\sigma + \frac{\partial \sigma}{\partial x}\mathrm{d}x\right)A + qA\mathrm{d}x = \rho A\mathrm{d}x\frac{\partial^2 u}{\partial t^2}, \qquad \textbf{Equation 4-1,}$$

where ρ is a rod density and A is cross-sectional area of the rod. In the absence of the body force, the equation can be reduced to:

$$\frac{\partial \sigma}{\partial x} = \rho \frac{\partial^2 u}{\partial t^2}, \qquad \textbf{Equation 4-2.}$$

Assume the material behaves elastically following Hooke's law, $\sigma = E\frac{\partial u}{\partial x}$, Equation 4-2 can be written as:

$$\frac{\partial}{\partial x}\left(E\frac{\partial u}{\partial x}\right) = \rho \frac{\partial^2 u}{\partial t^2} \qquad \textbf{Equation 4- 3,}$$

if the rod is assumed to be homogenous, so E and ρ are uniform in the rod, the governing wave equation can be obtained as:

$$\frac{\partial^2 u}{\partial x^2} = \frac{1}{c^2}\frac{\partial^2 u}{\partial t^2}, \quad c = \sqrt{\frac{E}{\rho}}, \qquad \textbf{Equation 4- 4.}$$

The wave equation above corresponds to a longitudinal wave propagating along the rod with a sound velocity c, which depends on the material's elastic constant and density. The general solution of the wave equation may be written in the D'Alembert form:

$$u(x,t) = f(x-ct) + g(x+ct), \qquad \textbf{Equation 4- 5,}$$

where f and g are outgoing and incoming waves.

4.2.2 Acoustic Impedance

The D'Alembert solution contains two wave functions that propagate at the velocity c. The first term on the right hand side represents propagation along the positive x direction and the second term along the negative direction. The solution must be

further analyzed to learn about the stress wave along the bar at any moment of time. Consider a simple form of the solution with only a displacement function *g* that travels in the negative *x* direction. The slope of the displacement wave is the stress wave according to Hooke's law:

$$\sigma(x,t) = E\frac{\partial u}{\partial x} = Eg'(x+ct). \qquad \textbf{Equation 4- 6.}$$

The particle velocity in the bar is given by:

$$v(x,t) = \frac{\partial u}{\partial t} = cg'(x+ct), \qquad \textbf{Equation 4- 7.}$$

The relationship between stress and particle velocity is given from Equation 4-6 and 4-7 as:

$$\sigma(x,t) = \frac{E}{c}v(x,t) = \sqrt{\rho E}\,v(x,t) = Zv(x,t) \qquad \textbf{Equation 4-8.}$$

The stress magnitude is linearly proportional to the particle velocity. Z or $\sqrt{(\rho E)}$ is the acoustic impedance of the material [47, 48, 51]. Equation 4-8 can be viewed as an analogy to "Ohm's law" in electrical conduction, where σ and v are analogous to voltage and current respectively. One should understand the difference between the sound velocity *c* and particle velocity *v*; *c* is the velocity at which waves propagate and the wave information and energy are transmitted at this velocity. The sound velocity is typically higher than the particle velocity by several orders of magnitude. For a typical FSMA sample with *E* of 30 GPa[2] and density of 8000 kg/m^3, *c* is 1940 m/s, while the particle velocity for a stress pulse of magnitude 100 MPa is only 6.5 m/s.

[2] Here, we use the modulus of martensite inside the twins, not the effective modulus when twin boundaries are in motion.

4.2.3 Natural Frequency

Next, the natural frequency of a longitudinal vibration along a bar is considered by solving the wave equation (Equation 4-4). An analysis of free vibrations of a finite thin rod with one end free and the other end fixed at the wall is illustrated in Figure 4-11.

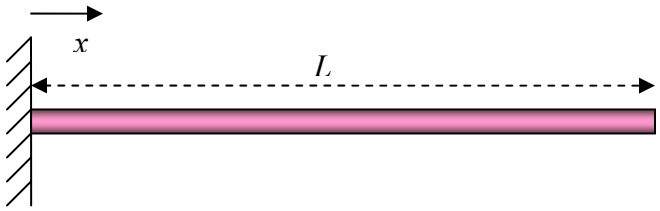

Figure 4-11: a finite rod with one end fixed at the wall

The boundary conditions corresponding to clamping at $x = 0$ and no stress at $x = L$ are:

$$u(0,t) = 0, \quad \frac{\partial u(L,t)}{\partial x} = 0 \qquad \textbf{Equation 4-9.}$$

Using the separation of variables with $u = Y(x)\psi(t)$, the solutions are in the forms: $\psi(t) = A \sin(\omega t) + B \cos(\omega t)$ and $Y(x) = C \sin(\beta x) + D \cos(\beta x)$, where $\beta^2 = \omega^2/c^2$. Then, apply the boundary conditions to the solutions, we obtain:

$$u(x,t) = \sum_{n=1}^{\infty} (A_n \sin \omega_n t + B_n \cos \omega_n t) \sin(\beta_n x),$$

$$\omega_n = c\beta_n = c\left(\frac{2n-1}{2}\right)\frac{\pi}{L}, \quad n = 1,2,3,... \qquad \textbf{Equation 4-10,}$$

where ω_n are the natural frequencies for this system. If a forced vibration frequency corresponds to a natural frequency, resonance occurs where the amplitude of the vibration of the specific natural mode dominates the response of the displacement shape.

For a typical dimension of FSMA samples used in this study, with a length of 1.5 cm, an elastic modulus of 30 GPa and a density of 8000 kg/m^3, the sound velocity is 1940

m/sec. The first resonant frequency of the longitudinal wave is 30 kHz and the second resonant frequency is 90 kHz. The normal modes for the first two longitudinal frequencies are illustrated in Figure 4-12. The longitudinal displacements along the rod are plotted on the vertical coordinate and the arrows give a direction of particle motion. Note that these frequencies are an order of magnitude greater than the piezo frequencies at which we observe significant reductions in H_{th} and σ_{tw}.

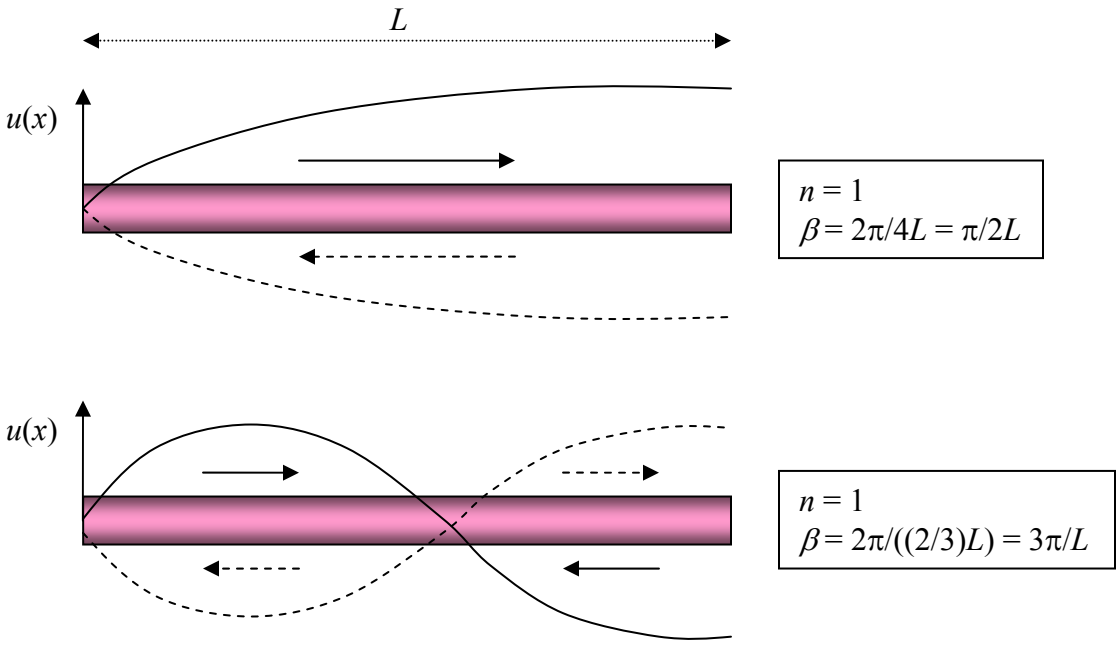

Figure 4-12: The first two modes of a rod with one fixed end. The arrows represent the directions of the particle motion; the dashed line is the particle motion half a period earlier or later. The amplitude of the longitudinal displacement is plotted along the vertical axis.

4.3 Discussion

4.3.1 Acoustic-Assisted Stress

In the experimental setup, an FSMA sample is attached to the piezoelectric at one end and free at the other end as shown in Figure 4-13. The 33-mode piezoelectric stack is driven by a sinusoidal voltage such that it actuates longitudinally. Typically, the

displacement amplitude of the piezoelectric is in the range of 1 – 7 microns. As a result, the piezoelectric actuation generates acoustic longitudinal waves in the sample. The setup should be similar to the structures discussed in the previous section, where the bar is fixed at one end and free at the other. Therefore, the resonant frequencies of the system in Figure 4-13 are the same as those in Figure 4-12. In the experiment, to avoid heating of the piezo stack, it was typically operated in the range of 500 – 10 kHz, which is much lower than the first natural frequency of longitudinal vibrations of the FSMA sample.

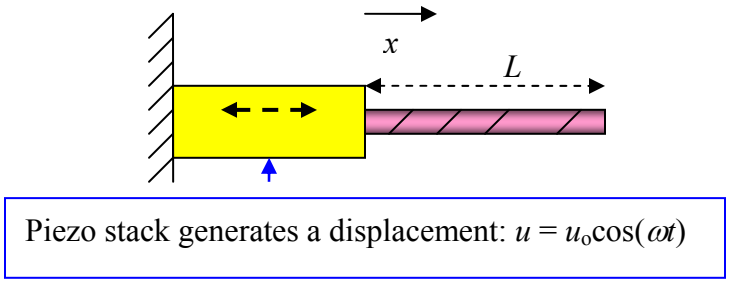

Figure 4-13: Experimental setup with piezoelectric stack attached to the bar sample. The stack is a displacement wave source.

We have calculated the first longitudinal resonance of the FSMA sample to be of order 30 kHz. Therefore, the maximum piezo effect occurring at 1 – 5 kHz observed in the experimental data for both the threshold field and twin-yield stress are not due to the natural frequency of longitudinal vibration in the FSMA. However, it is possible that the resonant frequency of the other vibration types (e.g. bending modes) might be responsible for the observed resonance. This will be discussed in detail in Sec. 4.5.

The operating drive frequency from the piezo is much smaller than that of the first resonant mode of an untwinned FSMA sample. One would expect that, at low drive frequency, the FSMA sample should not be affected much by the piezo vibration and only move back and forth in a rigid-body mode. However, the reduction in both threshold field and the twinning stress implies that the stress wave is actually transmitted into the sample to facilitate twin motion. We can estimate the magnitude of the stress

wave from this piezo assist even at low frequency from the dynamic "Ohm's law" in Equation 4-8. The stress magnitude increases as the product of the particle velocity and the acoustic impedance. For a piezo stack generating a dynamic displacement $u = u_o \cos(\omega t)$, the maximum particle velocity of the acoustic wave from the piezo is estimated to be $u_o\omega$, where u_o is a maximum actuating amplitude for a given $V_{p\text{-}p}$. Hence, the magnitude of the stress wave transmitted into the FSMA sample from the piezo stack should simply be linearly proportional to the drive frequency and $V_{p\text{-}p}$. Using this basic equation, we can obtain the expected stress magnitude as a function of $V_{p\text{-}p}$ and frequency as plotted in Figure 4-14. These calculated stresses range up to 4 MPa, depending linearly on piezo frequency.

The expected stress from piezo actuation may be viewed as an extra stress provided by the piezo stack to help reduce the twinning stress. Therefore, the measured twinning-stress reduction (from Figure 4-8 and Figure 4-9) is virtually equivalent to the calculated stress provided by a piezo assist (Figure 4-14). From the calculation, the extra stress magnitude is actually as high as 1.4 MPa for a piezo driven at 30 $V_{p\text{-}p}$ and 5 kHz; while, the maximum reduction of twinning stress in sample TL9-1A is only 0.4 MPa and 0.25 MPa for sample TL8-1A. It should be noted that Figure 4-14 shows the maximum possible stress magnitude by assuming that the FSMA sample is perfectly elastic and isotropic and the transmission of the stress wave from the piezo stack to the FSMA sample is perfect without any loss or reflection. In reality, the FSMA sample is strongly anisotropic with a tetragonal martensitic phase and also responds plastically when twin boundaries move. Therefore, the stress wave may be dispersed or reflected at the twin boundary regions significantly reducing its magnitude; hence, the actual stress generated in the FSMA is much less than the calculated values. Moreover, the calculated stress is the amplitude of the sinusoidal function; as a result, the instantaneous stress amplitude oscillates over time. This stress wave analysis actually gives us insight to the magnitude of the piezo assist effect on the FSMA actuation in the form of calculated stress. The calculated stress magnitude is in fairly good agreement with the empirical twinning-stress reduction. For 30 $V_{p\text{-}p}$ at 2 kHz, the calculated stress wave is 0.5 MPa, while the stress reduction in both samples TL8 and TL9 are 0.25 and 0.3 MPa correspondingly.

It should be noted that the stress-wave analysis predicts that higher $V_{p\text{-}p}$ should decrease the twinning stress at a given frequency. This prediction seems to agree for the 10 $V_{p\text{-}p}$ piezo assist (Figure 4-9), which results in a smaller twinning-stress reduction than observed in higher $V_{p\text{-}p}$ piezo assist cases. However, for $V_{p\text{-}p}$ above 10 $V_{p\text{-}p}$, the difference in the rate of the twinnin- stress reduction over frequency cannot be observed from the data. The piezo effects over increasing frequency actually look identical for 30 and 50 $V_{p\text{-}p}$. It is difficult to accurately measure a stress value to 0.1 MPa precision. The measurement error can be in the range between 0.1 – 0.5 MPa. With initial twinning stress as low as 0.35 MPa for sample TL8 and 0.7 MPa for TL9, the twinning-stress reduction measurement may not be precise enough to compare a rate of reduction over increasing frequency between the 30 and 50 $V_{p\text{-}p}$ cases. For example, with a 1 kHz increment, the calculated stress is increased by 0.2 and 0.5 MPa for 30 and 50 $V_{p\text{-}p}$ respectively; the magnitude of the stress is almost equal to the initial twinning stress for both samples and in the range of the possible measurement error.

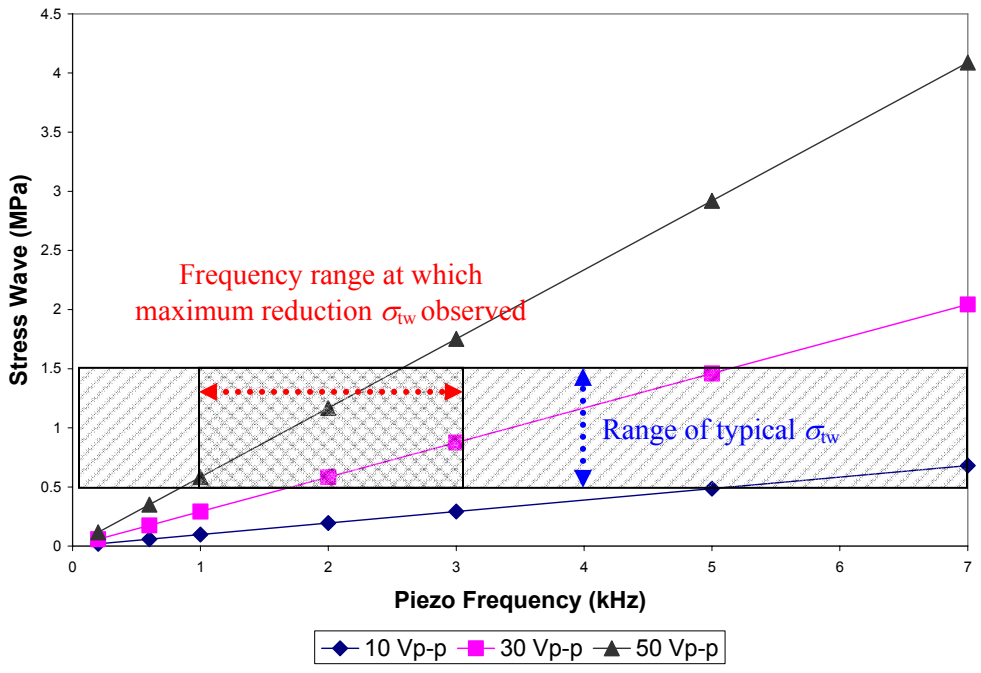

Figure 4-14: Calculated maximum stress wave as a function of piezo driven $V_{p\text{-}p}$ and frequency. These stress magnitudes are theoretically expected to be generated inside FSMA sample from a piezo stack actuation.

4.3.2 Frequency Dependence of Piezoelectric Stack

From the experimental data, the maximum reduction is achieved in the frequency range between 1 – 3 kHz for either sample; while, the extra stress is calculated to be 0.5 MPa for 50 $V_{p\text{-}p}$ at 1 kHz and for 30 $V_{p\text{-}p}$ at 2 kHz. The frequency is in the right range at which we observe the maximum twinning stress reduction and at higher frequencies the piezo assist does not have significant effect. Even though the empirical stress reduction is not expected to be as large as the calculated extra stress, one would expect that the piezo assist should continue decreasing the twinning stress or the threshold field to zero, as the piezo drive frequency increases. However, the data show that the piezo effect becomes insignificant beyond certain frequency range (between 1 – 5 kHz). The saturation of the piezo effect above about 5 kHz may be explained by a degraded piezo performance at high frequency.

Piezoelectric performance, especially actuation amplitude, is known to decrease when operating at higher frequency [52]. Some of the input energy is converted into heat instead of mechanical strain, which is evident by a rise in temperature associated with piezoelectric actuation at high frequency. We measured the displacement of the piezo stack used in this experiment over increasing frequency and the results are plotted in Figure 4-15. Clearly, the piezo stack's displacement decreases with frequency. The displacement is roughly independent of frequency below 2 kHz. Above 2 kHz, the displacement starts to decrease; the displacement drops dramatically at 3 kHz for 50 $V_{p\text{-}p}$. Then, the displacement steadily decreases with frequency. At 7 kHz, the displacement magnitudes for 10, 30 and 50 $V_{p\text{-}p}$ are close to one another.

Using the acoustic "Ohm's law" (Equation 4-8) and the empirical data of the piezo displacement-vs.-frequency, the approximate amplitude of the stress wave expected from the piezo stack actuation is calculated, shown in Figure 4-16. For the frequency below 2 kHz, the stress wave amplitude linearly increases with increasing frequency. For 2 – 5 kHz, the stress amplitude appears constant. Above 5 kHz, the calculated stress wave decreases with increasing frequency.

The calculation of the stress wave amplitude is based on assumptions that the sample is isotropic and perfectly elastic, while the FSMA sample is strongly anisotropic

and also responds plastically. Therefore, the actual stress generated in the FSMA may not exactly correspond to the calculated value; in fact, the actual stress is much less than the calculated one. However, the results in Figure 4-16 apparently account for a significant amount of the loss of piezo assist effect for frequency above about 7 kHz.

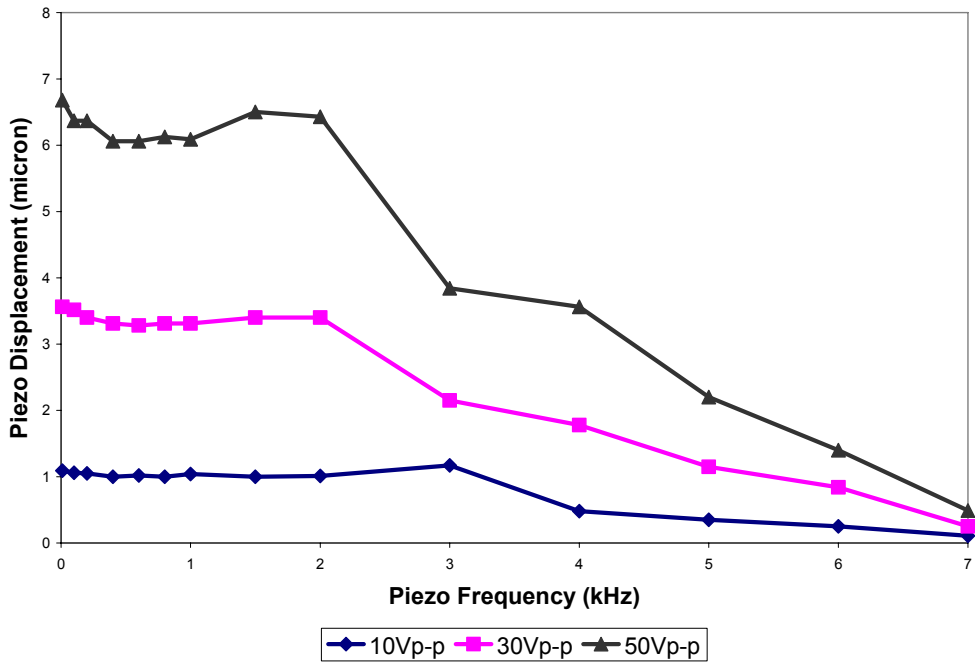

Figure 4-15: The displacement of the piezo stack as a function of drive frequency.

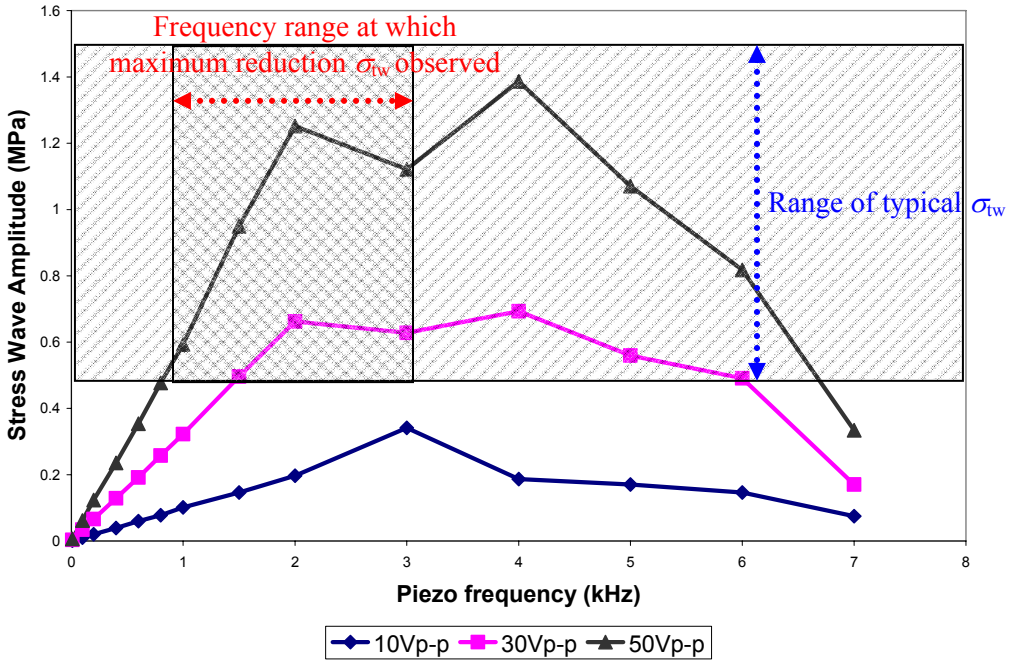

Figure 4-16: Calculated stress wave amplitude as a function of piezo driven $V_{p\text{-}p}$ and frequency. These stress wave magnitudes are calculated using the acoustic "Ohm's law" (Equation 4-8) and experimental data (Figure 4-15) above.

4.3.3 Local Acoustic-Assist Vibration

Another possible reason that the acoustic assist cannot reduce the twinning stress and threshold field completely to zero may be due to the sinusoidal drive function of the piezo actuation. As shown in [36] and [40], when the acoustic stress pulse from piezo actuation is pre-shaped such that the tensile stress is greater than the compressive stress or vice versa, the magnitude of the biased stress pulse can move a twin boundary in either direction. However, in this experiment, the piezo actuation is driven by a sinusoidal $V_{\text{p-p}}$ function, so the tensile and compressive waves are equally generated inside the samples. As a result, the piezo assistance in this case should be thought of as an alternating stress superimposed on the relatively static magnetic or mechanical stress. This local vibrating energy may be similar to the role of thermal vibration in facilitating dislocations or twin boundaries to overcome the defect barriers [53]. These local vibrations do impart additional energy and, as a result, the twinning stress decreases, because the required energy to overcome the barriers is reduced. However, they do not provide *work* in a

given direction to cause directed twin boundary motion unless an external work or bias stress is applied. For example, if no external compressive stress is applied on a FSMA sample, a sinusoidal acoustic actuation does not provide work and cannot move a twin boundary predominantly in any one direction by itself. Thermal vibration also has similar effect inasmuch as at higher temperature the twinning stress decreases. However, twin boundary motion is not expected to take place as temperature increases unless external stress is applied.

4.3.4 Plastic Waves

So far, our stress wave analyses are based on the assumption of linear elasticity. The magnitude and speed of the stress waves are calculated based on elastic properties of the FSMA crystals. In reality, FSMA crystals are strongly plastic in the presence of twin boundary motion. The twin-yielding stress can be as low as 0.4 MPa as observed in the experimental results. Stress waves below the twin-yield stress propagate with the speed of sound through the crystal. However, if the stress waves exceed the twin-yield stress, the stronger stress waves propagate more slowly at the speed of the plastic waves given by [47]:

$$c_{\mathrm{P}} = \sqrt{\frac{S}{\rho}} \qquad \textbf{Equation 4-11,}$$

where S is the plastic stiffness and ρ is the density of the material. Measured values of S for sample TL8-1A and TL9-1A are approximately 5 and 25 MPa, respectively and the density of FSMA is 8000 kg/m^3; c_{p} is then approximately 25 and 56 m/s for sample TL8-1A and TL9-1A respectively. The speed of plastic waves in FSMA is much slower than the calculated speed of elastic waves (1940 m/s) by two orders of magnitude. The plastic deformation does not occur uniformly in the FSMA crystal; the regions with twin boundaries are where plastic deformation can begin and the plastic waves can propagate. Also waves maybe reflected at twin boundaries due to the impedance mismatch across a twin boundary.

In the case of plasticity, the stress-strain relationship becomes nonlinear and complex. Sometimes the strain rates may play role; as a result, a visco-plastic response might be expected [48]. The plastic waves may possibly be attenuated while propagating through the crystal; a fraction of acoustic energy is converted into heat due to *internal friction*.

In this work, the stress waves were supplied to one end of the crystal. The stress waves, with stress lower than σ_{tw}, should be able to propagate to the other end of the crystal with minimal energy loss. However, the stress waves exceeding σ_{tw} should become plastic when they encounter twin boundaries in the crystal's portion closest to the piezo stack. The acoustic energy loss may be large resulting in minimal stress wave magnitude at the later portion of the crystal. It is possible that the piezo assist may have minimal, if any, effect on twin boundary motion in the portion of the sample beyond the first active twin boundary. A maximum stress reduction in FSMA crystals may be then limited by the energy loss due to the twin boundaries in the earlier portion of the crystal.

4.4 Finite-Element Method Analysis

The characteristics of wave propagation along a finite rod at frequencies much lower than the first natural frequency are investigated using finite-element tools. In the actual experimental setup, a 1.5-cm FSMA sample is attached to the piezoelectric stack at one end and free at the other end. The piezoelectric stack generates longitudinal displacement waves to the sample at relatively low frequency (~5 kHz). The magnitudes of longitudinal stresses along the bar generated by this longitudinal wave are calculated here using the finite-element methods. The FEM software used in this project is Automatic Dynamic Incremental Nonlinear Analysis (ADINA) [54, 55].

A 30 x 4 9-node element assemblage is constructed. The 2-D bar is 1.5 cm in length and 0.3 cm in width. The line on the left is fixed with no translation or rotation. A plane stress 2-D solid with a 0.1-cm thickness is assumed in this calculation. Figure 4-17 below shows the mesh structure used in ADINA.

The material is assumed to be isotropic and elastic. The assumptions may be inconsistent with the FSMA properties, which are tetragonal-type anisotropic and inelastic due to twinning motion. However, the anisotropic and inelastic problems are complex and require extensive understanding of FEM analysis. The purpose of this section is to provide an introductory insight to stress-wave propagation that allows us to have better understanding of the piezo-assistance.

In fact, the elastic assumption is valid to a certain level. The acoustic wave originating from the piezo stack is initially transmitted into the FSMA sample elastically. The incoming stress wave then propagates through the FSMA elastically until it meets a plastic region that may contain twin boundary. If the magnitude of the stress wave is large enough to move a twin boundary, the stress wave continues propagating as a plastic wave [47]. In the plastic region, some of the acoustic energy is reflected at the interface and some is transmitted and decays in the moving twin boundary, being converted into heat. Therefore, by considering elastic behavior in FEM analysis, we can actually study the initial wave propagation behavior and the magnitude of the stress provided into the samples.

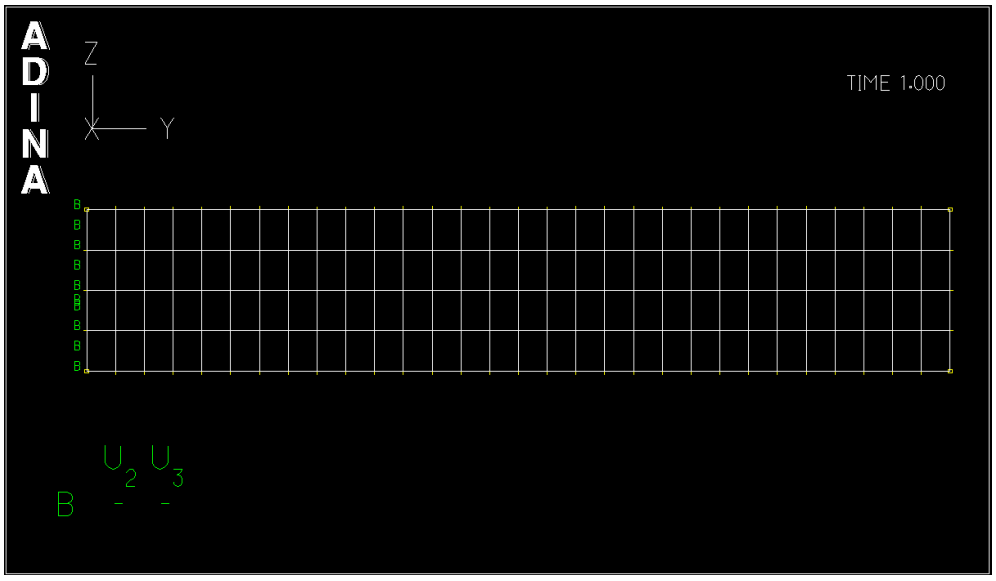

Figure 4-17: A 30x4 9-node element assemblage of FSMA sample with 1.6-cm length, 0.3-cm width and 0.1-cm depth. The assemblage is fixed with no translation or rotation on the left side and free on the other end.

Table 4-1: First fifteen natural modes of vibrations of a finite bar with one fixed end and free the other end. These natural modes include all types of vibrations including bending, transverse and longitudinal vibration. Modes in bold and italicized (3, 6, 8, 11 and 15) correspond to the natural longitudinal modes.

Natural Mode Number	Frequency (kHz)
1	3.578
2	19.74
3	***30.29***
4	47.91
5	80.8
6	***90.76***
7	116.2
8	***150.8***
9	152.4
10	188.1
11	***209.7***
12	213.9
13	227.9
14	240.9
15	***264***

4.4.1 Natural Mode Calculation

The natural-vibrational modes are calculated to obtain the natural frequencies, which include bending, transverse and longitudinal vibrations. Table 4-1 above lists the frequencies the first fifteen modes of the system. The modes in bold correspond to the longitudinal vibration modes. It is the longitudinal mode that results in the largest resolved shear stress across the twin boundary. The first and second natural modes for longitudinal vibrations for this analysis are the third and sixth overall modes in Table 1. The mode shapes, illustrated in Figure 4-18 below, show the original mesh and the deformed one for mode 1, 2, 3 and 6. The first two modes are pure bending type. Mode 3 is the first mode containing only longitudinal displacement, except for small transverse displacements due to the Poisson effect. Mode 6 also shows a response equivalent to the second natural longitudinal mode. Both mode 3 and 6 are identical to the ones shown in Section 4.2.3 and Figure 4-12.

It should be noted that the first overall mode at 3.6 kHz is the only mode below 15 kHz, which is in the same region that the piezo stack is operated. Maximum yield

stress/threshold field reduction is also observed at the frequency region between 2 – 5 kHz. Especially, for the threshold field, a possible resonant is observed in the threshold field reduction at 5 kHz where the threshold field is reduced to the minimum (Figure 4-4). The samples are attached to the piezo at one end and free at the other end. It may be possible that a small bending displacement of the samples results while being longitudinally vibrated by a piezo stack. The resonance of the bending vibration at this frequency region may magnify the small displacement into a significant amount of vibrational energy in the FSMA sample. This extra vibrational energy may help facilitate twin boundary motion and significantly reduce the twinning stress in the region of 2 – 5 kHz. This possible concept will be discussed more in Sec. 4.5.

4.4.2 Wave Propagation in Elastic Media

In ADINA, acoustic waves from the piezoelectric stack are considered as a prescribed sinusoidal displacement applied at the left end of the bar. The input drive frequency is 5 kHz and the longitudinal displacement amplitude is 3.5 micron corresponding to the amplitude for 30 $V_{p\text{-}p}$. At the interface between the piezo stack and the bar, Y-translation is allowed for a small prescribed displacement from piezoelectric actuation, while Z-translation and X-translation are constrained. The mesh element assemblage of this problem is shown in Figure 4-19 below.

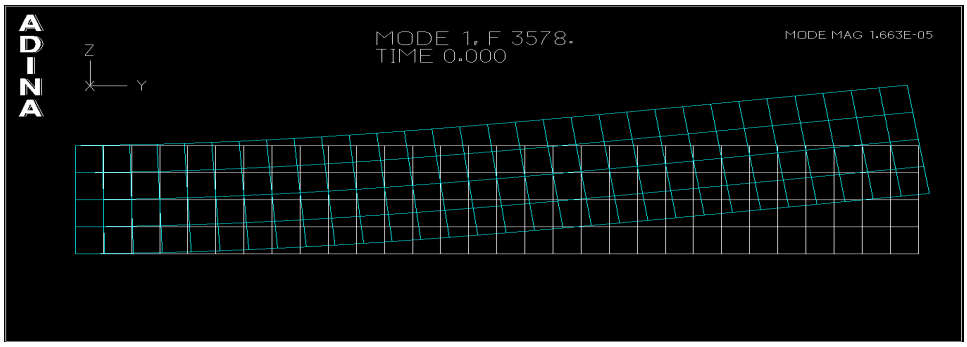

(A)

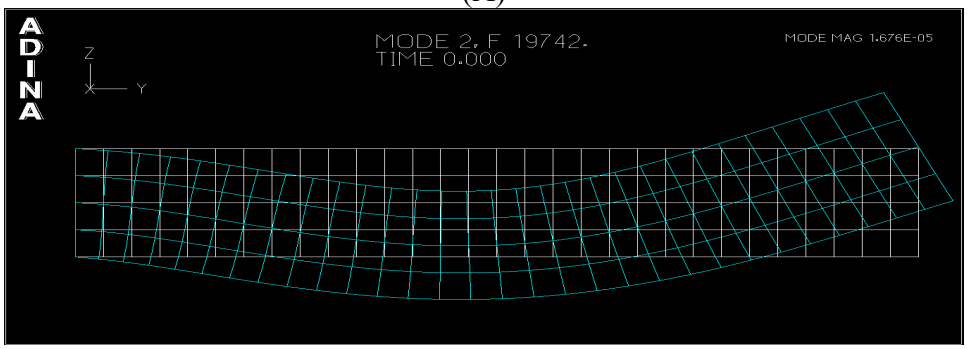

(B)

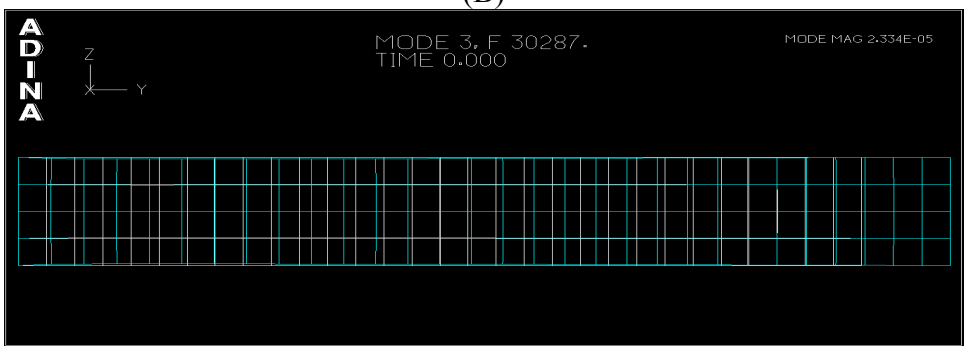

(C)

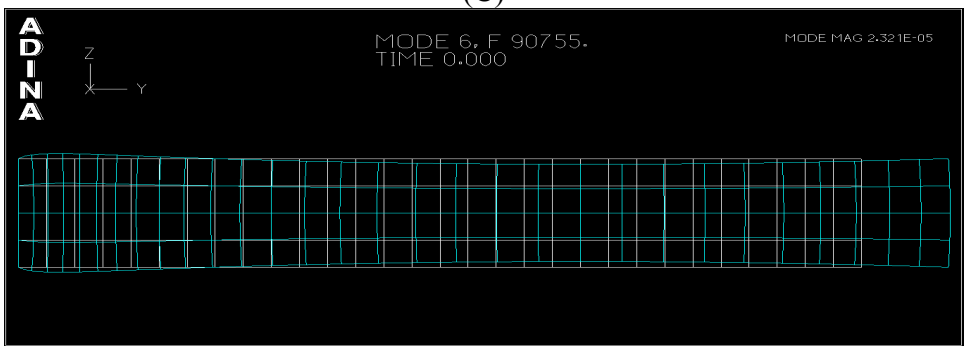

(D)

Figure 4-18: Natural mode shapes for (A) mode 1, (B) mode 2, (C) mode 3 and (D) mode 6. Each figure shows an original mesh (straight bar) and a deformed mesh for comparison. The lowest mode 1 is a bending type occurring at frequency of 3.6 kHz. Mode 3 corresponds to the first lowest natural mode of longitudinal vibration occurring at 30 kHz. Mode 6 at 90 kHz is the 2nd lowest natural mode of longitudinal vibration.

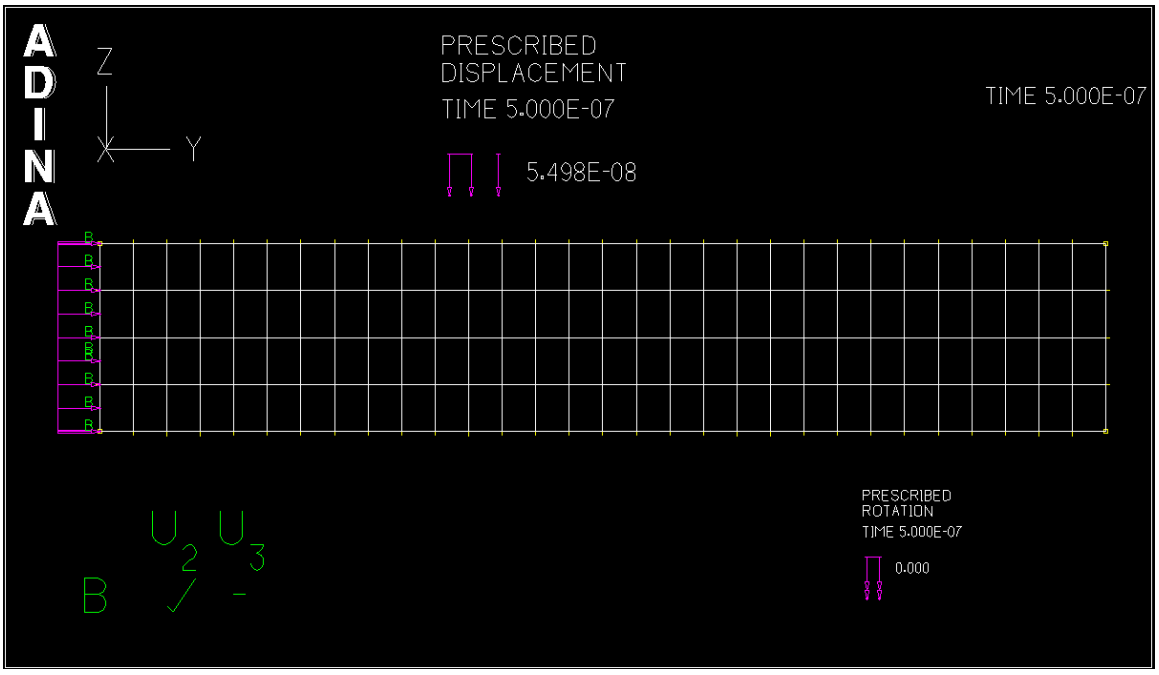

Figure 4-19: A mesh assemblage of FSMA bar. A prescribed displacement load is applied at the left side of the bar representing the interface between the piezo stack (where the displacement load is generated) and the FSMA sample. The longitudinal displacement varies as a sinusoidal function with 5 kHz frequency and 3.5 micron amplitude.

Figure 4-20 shows Y-displacement-vs.-time curves at three different points along the bar: (1) the interface between the piezoelectric and the bar, (2) the middle point of the bar and (3) the right end tip of the bar for the 5 kHz excitation. The displacement-vs.-time at the interface satisfies the boundary condition of the prescribed displacement at the interface showing a smooth sinusoidal response with amplitude of 3.5 micron and a period of 2×10^{-4} sec. For the middle and the tip of the bars, the average phase of the displacement is about the same as the displacement at $y = 0$. The displacement-vs.-time responses away from the interface are almost sinusoidal with similar period with a small signal at about $5 \times f_o$ superimposed (2^{nd} harmonic). The drive frequency is about ten times smaller than the first natural frequency for longitudinal vibrations; hence, the vibration mode is in the static region compared to the first natural frequency. The time for an acoustic wave to propagate from the interface to the tip is much shorter than the period of the wave. As a result, the average displacements at the middle and the tip of the

bar are similar to the displacement generated from the piezoelectric stack at all time. This may lead us to believe that the bar vibrates in a rigid-body mode. However, the ripples in the displacement curve imply that the displacements are not uniform throughout the bar.

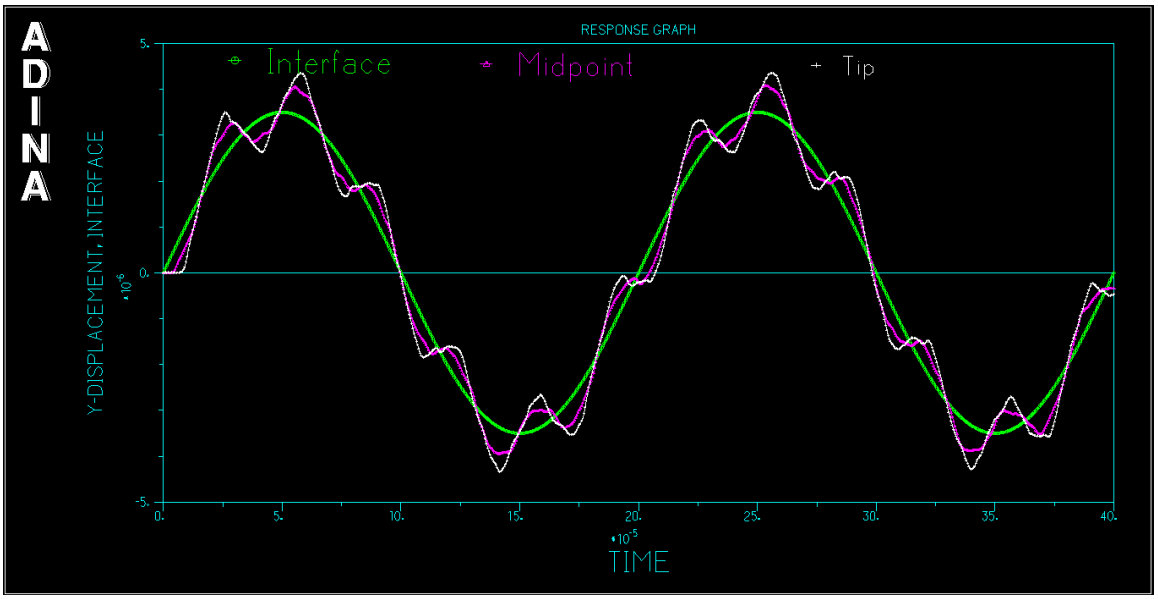

Figure 4-20: Y-displacement (m)-vs.-time (second) at the interface, middle and tip points of the bar for longitudinal-prescribed displacement at the interface of the bar.

The non-uniformity of the displacement along the bar is confirmed by a plot of the displacement over the bar length. In Figure 4-21, the Y-displacements along the Y-coordinate of the bar at sample times of 19 x 10^{-5}, 20 x 10^{-5}, 21 x 10^{-5} and 22 x 10^{-5} seconds are plotted. A displacement gradient is clearly present along the bar. The displacement gradients mean finite strains, which consequently imply that finite values of longitudinal stress should be present inside the bar (Equation 4-6). It should be noted that the boundary condition is satisfied at the free end of the bar where the slope of the displacement curves are always flat showing that the stress at the free end is zero at all time.

The stress magnitude resulting from the displacement wave from the piezoelectric is now considered. Figure 4-22 shows the longitudinal stress (stress YY) along the bar

Y-coordinate over sampling times = 6.5 x 10^{-5}, 19 x 10^{-5}, 21 x 10^{-5} and 34 x 10^{-5} seconds. Both compressive and tensile stresses are present at different times. The stress vanishes toward the right free end as expected.

Finally, in Figure 4-23, the longitudinal stress for the elements at the interface, where the maximum stress is expected, is plotted over time. The period of the stress wave is shorter than the period of the displacement wave. The maximum stress generated inside the bar is approximately 2.5 MPa. The stress calculated from the "Ohm's law" for 30 $V_{p\text{-}p}$ and 5 kHz is 1.5 MPa (Figure 4-14). Both values are within the same order of magnitude. These comparable results indirectly show that, for an operating piezo actuation with amplitude of 1 – 7 microns and frequency of 0 – 7 kHz, the expected magnitude of the acoustic-assistance elastic stress should be in the order of 0 – 2 MPa.

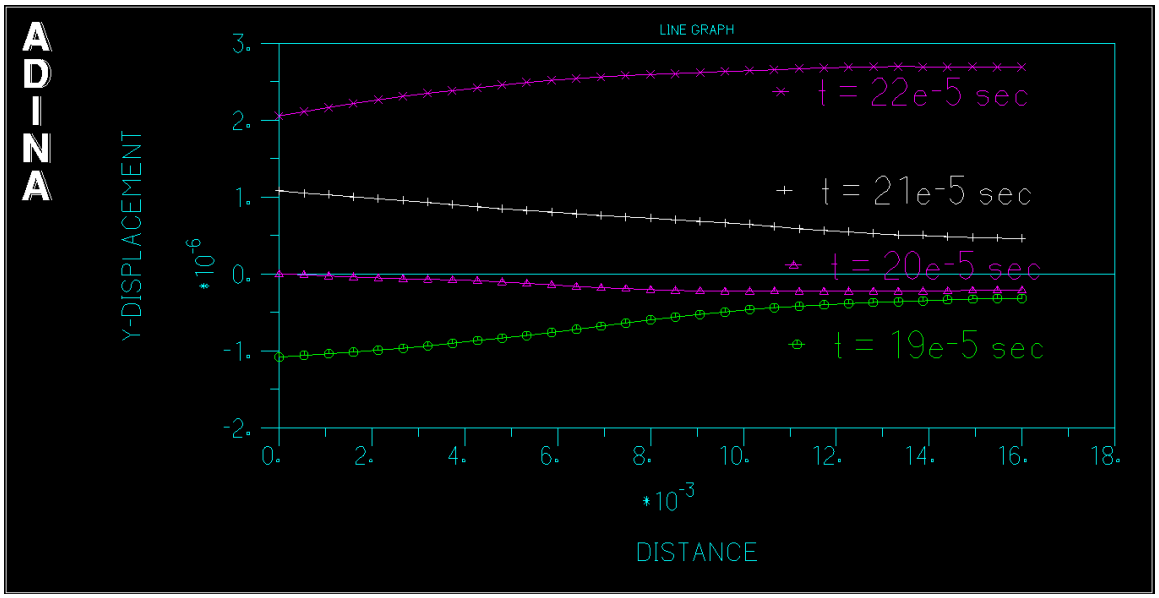

Figure 4-21: Y-displacement (m) along the Y-Cordinate distance (m) along the bar at different times.

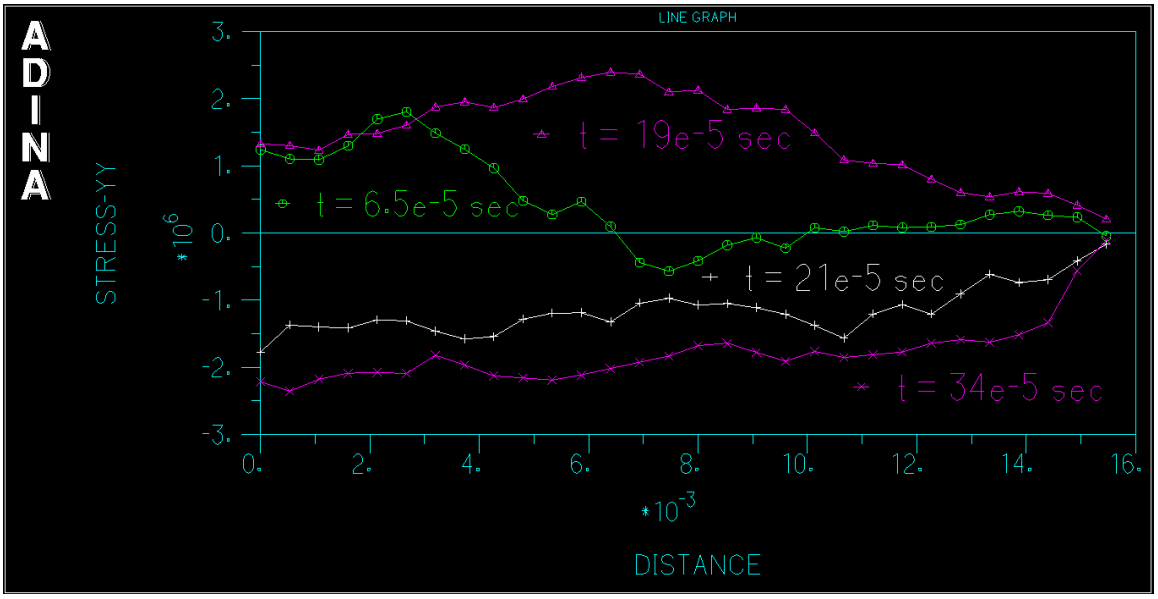

Figure 4-22: Calculated longitudinal stress (N/m^2) plotted against Y-Coordinate distance (m) along the bar at different times.

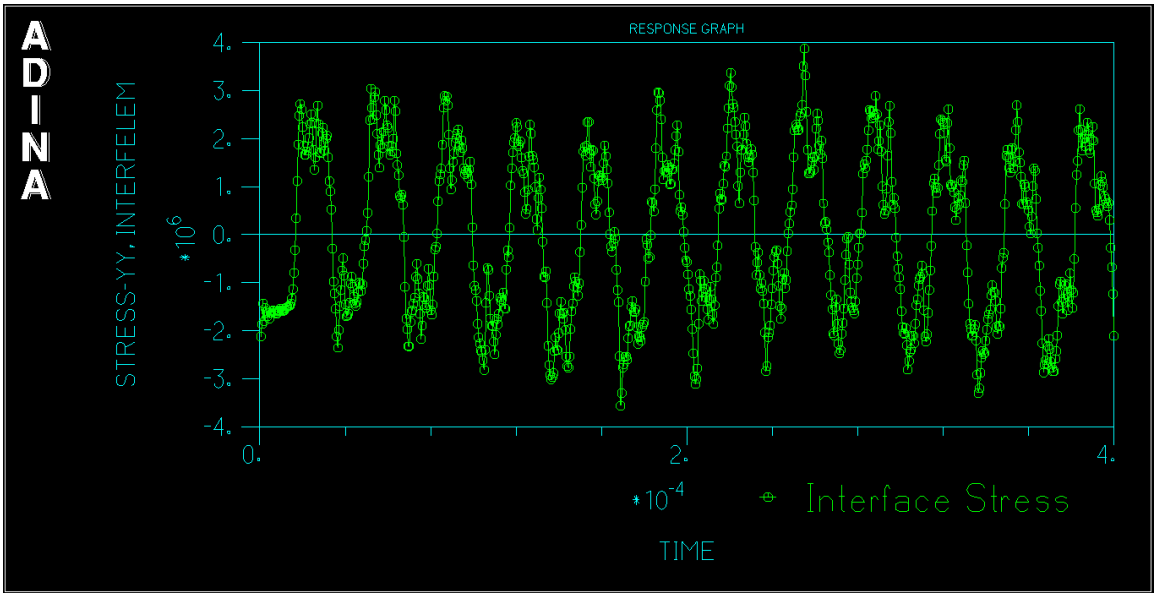

Figure 4-23: Calculated longitudinal stress (N/m^2), for the elements at the interface of the bar over time (second).

4.5 Transverse Acoustic-Assisted Magnetic Field Induced Strain

In the light of FEM analysis, there is the possibility that the bending mode may contribute to the stress wave magnitude as the first resonant frequency of the bending mode is in the region between 3 – 4 kHz. One may expect that a very small bending deflection may occur while the FSMA sample is longitudinally vibrated, as one end of the sample is left unconstrained. The small bending deflection might resonate significantly when the piezo frequency is in the region of the bending resonant frequency. Consequently, the resonant bending vibration may generate large bending stress to assist the twin motion. As a result, a new experiment was designed and conducted to investigate the possibility of the bending-mode contribution. A direct transverse-piezo assist is applied to investigate the possible outcome of the bending-mode resonant behavior.

A 15-mode piezoelectric stack was used in place of the longitudinal piezo stack to generate the shear stress waves directly to a FSMA sample. Similarly, the 15-mode piezo stack was attached to one end of sample TL9-1A. Epoxy was used instead of the superglue, because the shear waves were transmitted better with epoxy interface. The 15-mode stack was driven at 220 $V_{p\text{-}p}$, which is the maximum voltage limited by the amplifier power. The 220 $V_{p\text{-}p}$ results in a shear displacement of about 5 micron, which is comparable to the longitudinal displacement of the 33-mode longitudinal piezo stack driven at 30 $V_{p\text{-}p}$.

The piezo-assisted effects for the transverse and longitudinal waves are compared in Figure 4-24. The maximum reduction of the twin-yield stress by the transverse piezo assist is approximately 0.07 MPa, about six times smaller than the maximum reduction by the longitudinal piezo assist (0.45 MPa). For the transverse-assist result, no significant resonant characteristic is present in the observed frequency range; the twinning stress decreases slightly with increasing frequency and remains fairly constant at frequency above 1 kHz. The contribution of the bending vibration to the stress waves, if it actually exists, is clearly minimal compared to the stress wave from the longitudinal

vibration. The twinning-yield stress reduction with the longitudinal piezo assist should be predominantly due to the longitudinal stress waves.

The results in Figure 4-24 also imply that the longitudinal piezo assist is more effective to facilitate twin boundary motion than the transverse one, specifically for the FSMA sample with twin boundary planes oriented 45° to the base of the crystal (Figure 4-25). The stress responsible for twin boundary motion is the resolved shear stresses across twin boundary planes. Therefore, the most effective stress waves transmitted through the sample's cross-sectional base should resolve into maximum shear stresses waves along the 45° planes. Therefore, we need to obtain the normal and shear stresses acting on the planes inclined 45° to the base. This may be calculated by considering the *transformation equations* for plane stress that give the stresses oriented in a different direction [56].

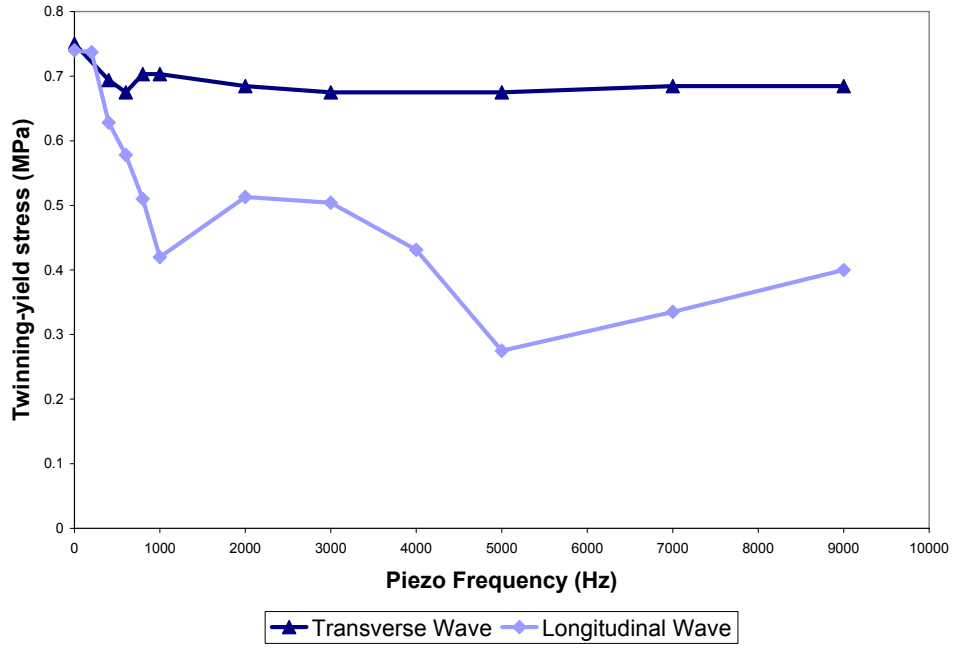

Figure 4-24: Comparison of the piezo-assisted effect between the 15-mode piezo stack (transverse acoustic actuation) and the 33-mode piezo stack (longitudinal acoustic actuation). The 15-mode piezo is driven at 220 $V_{p\text{-}p}$, which results in a shear displacement of 5 micron. The 33-mode piezo stack is driven at 30 $V_{p\text{-}p}$ giving a longitudinal displacement of approximately 4 micron.

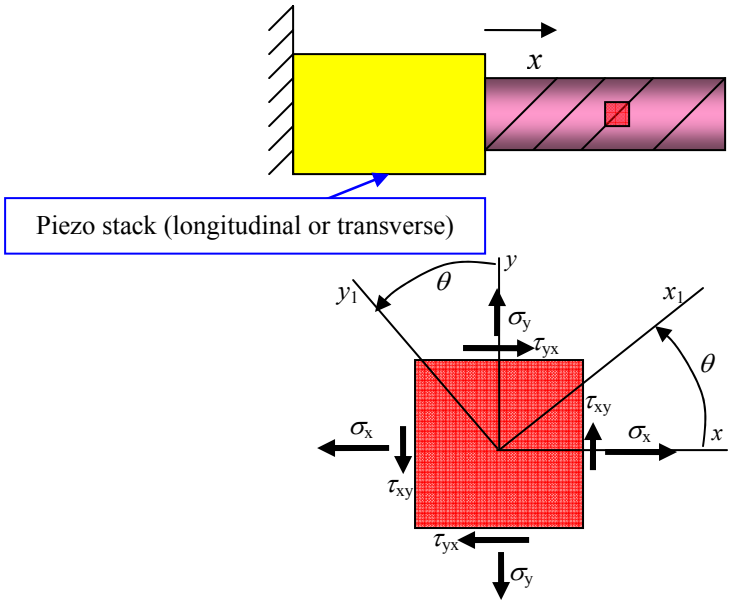

Figure 4-25: Top: An illustration of a FSMA sample with a piezo stack attached at the sample base. Twin boundaries are shown inside the sample oriented 45° to the base of the sample. Lower: An infinitesimal plane-stress element subjected to normal and shear stresses. The stress element represents the state of stress at any point in the sample body.

We consider a plane-stress element shown in the lower panel of Figure 4-25. The stress element is subjected to the plane stress in the *xy* plane: normal stresses (σ_x, σ_y) and shear stresses (τ_{xy}). Following the method of Gere, we can then derive the normal and shear stresses in the x_1y_1 coordinates rotated counterclockwise through an angle θ with respect to the *xy* coordinates as:

$$\sigma_{x_1} = \frac{\sigma_x + \sigma_y}{2} + \frac{\sigma_x - \sigma_y}{2}\cos(2\theta) + \tau_{xy}\sin(2\theta) \qquad \textbf{Equation 4-12}$$

$$\sigma_{y_1} = \frac{\sigma_x + \sigma_y}{2} - \frac{\sigma_x - \sigma_y}{2}\cos(2\theta) - \tau_{xy}\sin(2\theta) \qquad \textbf{Equation 4-13}$$

$$\tau_{x_1y_1} = -\frac{\sigma_x - \sigma_y}{2}\sin(2\theta) + \tau_{xy}\cos(2\theta) \qquad \textbf{Equation 4-14.}$$

If only uniaxial stress σ_x acts on the *xy* element, the corresponding transformation equations are:

$$\sigma_{x_1} = \frac{\sigma_x}{2}(1+\cos(2\theta)), \quad \tau_{x_1y_1} = -\frac{\sigma_x}{2}\sin(2\theta)$$ **Equation 4-15.**

The maximum shear stress can then be obtained at $\theta = 45^o$ from the uniaxial stress. For the case with pure shear applied at $x = 0$, the corresponding transformation equations can be obtained as:

$$\sigma_{x_1} = \tau_{xy}\sin(2\theta), \quad \tau_{x_1y_1} = \tau_{xy}\cos(2\theta)$$ **Equation 4-16.**

The maximum biaxial stresses ($\sigma_{x_1}, \sigma_{y_1}$) occur at $\theta = 45^o$; however, the shear stress is equal to zero.

The transformation equations show that, for uniaxial or biaxial stress, the planes of maximum shear stress occur at at $\theta = 45^o$; for pure shear, the maximum shear stresses occur at at $\theta = 0^o$ and the shear stresses become zero at at $\theta = 45^o$.

Longitudinal stress waves impart uniaxial tensile/compressive stresses into the sample normal to the base of the sample. Therefore, the maximum shear stresses can be obtained along the 45^o planes. On the contrary, the transverse stress waves transmit shear stresses onto the sample base. These shear stresses transform into biaxial stresses ($\sigma_{x_1}, \sigma_{y_1}$) and zero shear stress along the 45^o planes. Therefore, the analysis of the transformation equations clearly confirms that the longitudinal stress waves are the most efficient stress type to optimally enhance the twin motion of the twin boundaries oriented 45^o to the base.

CHAPTER 5

STRESS-BIASED FIELD-INDUCED STRAIN WITH PIEZOELECTRIC ASSIST

The previous chapter outlines the experimental data that characterize the effect of a piezo assist on MFIS or stress-induced strain in Ni–Mn–Ga single crystals. The piezo assistance provides a direct improvement in the FSMA actuation performance by significantly reducing the twinning stress or the threshold field, which is critical to reduce the size of an FSMA actuator with a given output.

So far, the piezo effect has been studied on the MFIS or mechanically-compressive strain under *free* conditions; for example, neither an external stress during MFIS nor a magnetic bias field during mechanical compression is present during measurement. In the presence of an external mechanical stress, the magnetic stress, limited by the anisotropy energy, must be larger than the sum of the external stress and twinning stress so that MFIS may occur: $K_u \geq (\sigma_{tw} + \sigma_{ext})\varepsilon_o$. Likewise, the magnitude of the magnetic stress reduced by the twinning stress indicates the potential stress output that can be achieved by MFIS actuation. The stress output is also an important property for active materials; therefore, it is desirable to reduce σ_{tw} as much as possible.

We have seen that sinusoidal acoustic waves provide extra help in the form of local *energy* delivered to twin boundary, not directed output *work*; therefore, one may not expect the piezo-assistance to provide extra output stress from the system. However, the piezo assist has been shown to facilitate the twin boundary motion and reduce the twinning stress such that the saved magnetic energy may provide the extra stress output. This indirect effect is to be explored in this chapter.

The sequence of this chapter is different from the previous two chapters. At this point, we sufficiently understand the piezo effect to the extent that we are confident to predict the outcome or improved performance that the piezo assist may provide. So, this chapter will begin with literature reviews on the results and discussion of stress-biased field-induced strain without acoustic assist. With the understanding of the piezo-assist effect, we may predict how the results will be improved by the piezo assistance. Finally, the actual experimental data of the MFIS under biased stress with and without piezoelectric assist will be shown and discussed to confirm our understanding of the piezo-effect on the MFIS in FSMA materials.

5.1 Reversible Strain under Magnetic Field and Bias Stress

Under free conditions, a full 6% MFIS can be achieved when the applied transverse field is large enough to overcome twin-boundary pinning barriers. But, because twin boundary motion is a mode of plastic deformation, it is not reversed upon removal of the field. To reset an FSMA sample back to zero strain requires an external reset mechanism such as an external compressive load applied along the axis that expanded under the action of the transverse field. This external load must be larger than the twinning stress in order to plastically compress the FSMA samples via twin boundary motion. However, to achieve a full reversible strain with an external load applied, the magnetic energy must be larger than the combination of the twinning stress and external bias stress. This is best illustrated in Figure 5-1 below. At very low external stress (e.g., curve 1 in Figure 5-1), a 4.5% MFIS is achieved with the minimum threshold field of 1.9 kOe. Because the external stress is very small, the strain is irreversible and remains at 4.5% as the field decreases to zero. When the magnitude of the external-compressive stress is below |–0.7| MPa (curve 2), only a small reset strain is observable; the strain decreases to 4% at zero field. With increasing external stress, the threshold field clearly increases and the maximum strain induced by magnetic field also decreases. This shows that the extra mechanical energy contributed by the bias stress requires a larger magnetic

energy to move the twin boundary. For the external stress above |–0.9| MPa (curve 3), the reset strain becomes significant. The external stress of |–1| MPa (curve 4) can compressively reset the sample back to zero strain. Then at the stresses above |–1| MPa, the maximum MFIS decreases significantly and the stress can fully reset the sample. This equal two-way strain is defined as "reversible strain", which is used commonly in this chapter. Finally, at very large stress (above –2 MPa, curve 5), very small MFIS is achieved even at high field; moreover, the threshold field increases to as high as 5 kOe. Hence, the reversible strain is also small because there is no strain for the mechanical load to reset.

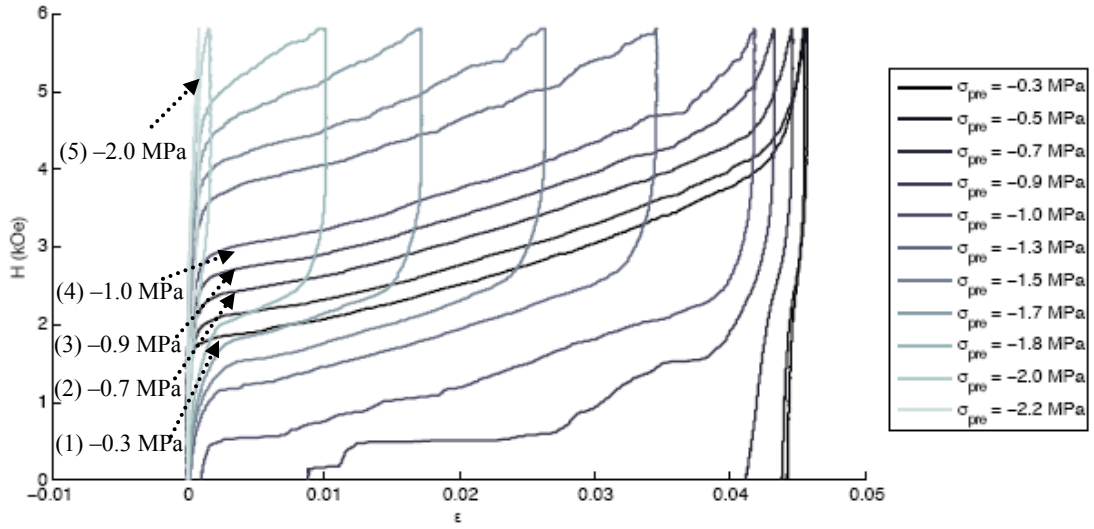

Figure 5-1: Magnetif-field induced strain under different constant external stress. The transverse field results in a positive strain. The external load is constantly applied perpendicular to the field to compresses the sample as the field decreases [57].

Clearly, it is difficult to achieve a full reversible strain close to the theoretical martensitic strain of 6% (or 4.5% for the exact sample used for data in Figure 5-1). Without external stress, there is no restoring force to reset the sample. Yet, with external stress, it is possible to get large reversible strain if the magnetic energy is sufficient to overcome both twinning and external stresses; the bias stress results in a higher threshold field and smaller MFIS. However, the magnetic energy applied to move the twin

boundary is limited by the magnetic anisotropy energy. If the total of twinning and external stress is higher than the stress imparted by the anisotropy energy, a large 6% theoretical reversible strain cannot be achieved.

The simple macroscopic condition for a large reversible strain is discussed and explained in [58-61]. To induce the full one-way strain magnetically, the following condition must be satisfied:

$$\frac{K_u}{\varepsilon_o} > \sigma_{tw} + \sigma_{ext}, \qquad \textbf{Equation 5- 1,}$$

where K_u is a magnetic anisotropy constant and ε_o is the martensitic-transformation strain. Then, to fully reset the sample at zero field, the applied stress, σ_{ext}, must at least be equal to σ_{tw}. Therefore, to achieve a full reversible strain, the condition,

$$\frac{K_u}{\varepsilon_o} > 2\sigma_{tw}, \qquad \textbf{Equation 5- 2,}$$

must be satisfied.

This condition basically implies that it is desirable to obtain an FSMA material with a large magnetic anisotropy and a very low twinning stress. However, a large anisotropy will require the application of a large magnetic field to achieve full magnetization. Therefore, to achieve a full reversible strain at relatively low magnetic field, the best method is to reduce the twinning stress. However, it is not yet known how to control the twinning stress systematically. The twinning stress is strongly dependent on the twinning structures and purity of the material, which is strongly affected by the material treatment history, such as heat treatment or mechanical training [59].

One may reduce the twinning stress by operating the FSMA actuation at elevated temperature, as the thermally-activated process of twin boundary motion is enhanced at higher temperature. Moreover, the material stiffness acts as a resistance to twin-boundary motion. The elastic constants for a Ni–Mn–Ga sample in a single-variant state have been reported to decrease as the sample is heasted below the austenite start temperature as shown in Figure 5-2 [62, 63]. Therefore, with a reduction in the stiffness

at higher temperature, the twin-boundary mobility should increase accordingly. However, the magnetic anisotropy of a tetragonal martensitic Ni–Mn–Ga sample also decreases with increasing temperature as shown in Figure 5-3 [64, 65]. As a result, the maximum magnetic driving force, limited by K_u, is diminished at higher temperature.

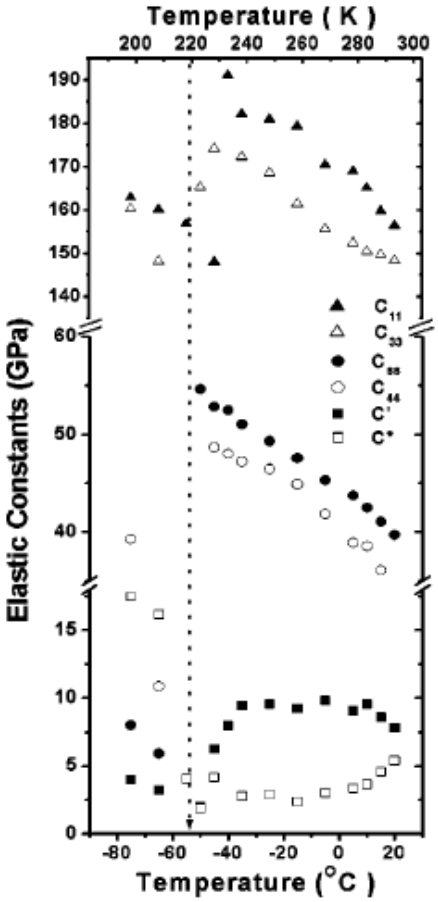

Figure 5-2: Temperature dependence of six elastic constants for $Ni_{0.50}Mn_{0.284}Ga_{0.216}$ in a martensitic single variant state. The vertical dotted line marks the intermartensitic phase transition [62, 63].

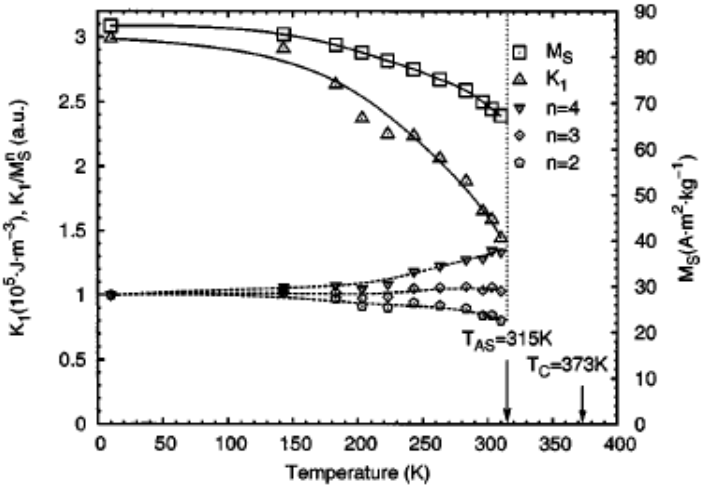

Figure 5-3: Magnetization (M_s) and magnetic anisotropy (K_1) of a five-layered tetragonal martensitic Ni–Mn–Ga sample. A dotted vertical line marks the martensite-to-austenite transformation temperature. Lower curves show the ratio of $K_1/(M_s)^n$ for n = 2, 3 and 4 [65].

It has been shown [20, 37] that a small acoustic energy with an appropriate polarization, applied to the Ni–Mn–Ga single crystal with a piezo stack actuator, reduces the threshold field and the external reset stress. This should facilitate a full reversible strain at low field. Consequently, the stress-biased magnetic-induced strain with and without piezo assist is investigated to expand our understanding of this benefit of the piezo assist on the stress and strain output during cyclic FSMA actuation.

5.2 Results and Discussion

The stress-biased field-induced strain of sample TL9-1A is measured. It should be noted that a maximum possible twinning strain for sample TL9-1A as measured in the previous chapter is 0.045. As shown in Figure 2-4, a cyclic transverse field, driven at 0.01 Hz from 0 to +/-5 kOe, is applied along the sample's width direction. A constant compressive load is applied to one end of the sample perpendicular to the field direction. A 33-mode piezo stack is attached at the other end to generate a longitudinal vibration along the sample length. The displacement of the sample under the cyclic field and

varying constant bias stress is measured with and without piezo assist. A piezo actuation of 40 $V_{p\text{-}p}$ and 7 kHz is applied for piezo-assistance.

Figure 5-4 shows the results of stress-biased field-induced strain under different constant external stresses. The reversible-strain behavior is expected for sufficiently high external stress as discussed in the previous section. With no bias stress, the magnetically-induced strain starts to grow at –1.9 kOe (a) and completes to 0.04 (b), which is slightly smaller than the expected full strain of 0.045 for this sample, at approximately –3 kOe. As the field returns to zero, the displacement is not reversed (c) as there is no restoring force. When the field is increased to 5 kOe, there is no further twin boundary motion because most of the variants already have their favorably-oriented easy axis along the field direction (d). So, the one-way MFIS is 0.04 but the reversible strain is zero. When the constant external stress increases to 0.6 MPa, the threshold field is clearly increased to approximately –3 kOe due to the extra magnetic stress required for overcoming the external stress for twin motion. A full strain of 0.044 is achieved at –5 kOe. As the field goes to zero, the external stress slightly resets the displacement from 0.044 to 0.041. Therefore, when the field increases to 5 kOe, only 0.003 of reversible field-induced strain is observed. For 0.75 MPa, the threshold field increases to –3.5 kOe and the maximum magnetically-induced strain is 0.033; the magnetic stress from a 5-kOe field is not large enough to overcome both twinning stress and 0.7-MPa biased stress to induce a full strain. As the field returns to zero, the external load starts to reset the sample when the field reduces to approximately –2 kOe level and then complete resetting is achieved just before reaching 0 kOe. Because the sample is fully reset such that all active variants have easy axes parallel to the stress direction (perpendicular to the field direction), when the field is driven to 5 kOe, the 3.3% MFIS occurs again and a similar resetting process by the external load also occurs as the field decreases to zero. Therefore, both MFIS and reversible strain are identically 0.033. Finally, at 1.05 MPa, the external stress is so large that the threshold field is as high as 4.8 kOe and the MFIS is only 0.005. So, both MFIS and reversible strain are equally 0.005. Clearly, for an external stress above 1.05 MPa, we would expect to observe neither MFIS nor reversible strain, because the magnetic stress is too small to move the twin boundary against the external load.

Next, the results with piezo assist are shown in Figure 5-5 and the behavior contrasted with the same sample as shown in Figure 5-4 (without piezo assist). The piezo assist dramatically improves the performance of FSMA actuation. At zero stress, the threshold field (at which twins start to move) is reduced from –1.9 to –0.7 kOe. Yet, the maximum MFIS is still attained at –3 kOe due to a demagnetization effect, which is consistent with the discussion in Chapter 3. The reversible strain is zero because no reset force is applied. A dramatic improvement on both MFIS and reversible strain is clearly observed for a 0.6-MPa external stress. The threshold field is –2 kOe, which is significantly improved when compared to –3 kOe without piezo assist. The full strain is now 0.045 which is equal to the maximum full twinning strain for this sample. More importantly, with piezo assist, a 0.6-MPa stress can fully reset the sample to its original dimensions, starting to reset the sample at –2.5 kOe and completing it at –1 kOe. Both maximum MFIS and reversible strain are equally 0.045. For both 0.75-MPa and 1.05-MPa stresses, the piezo-assist actuation aids the magnetic field to induce twin motion against the external load and defect-pinning barriers. The full MFIS of 0.045 is achieved in both cases. The reversible strain with piezo assist is increased to full strain of 0.045 as compared to the reversible strain measured without piezo assist.

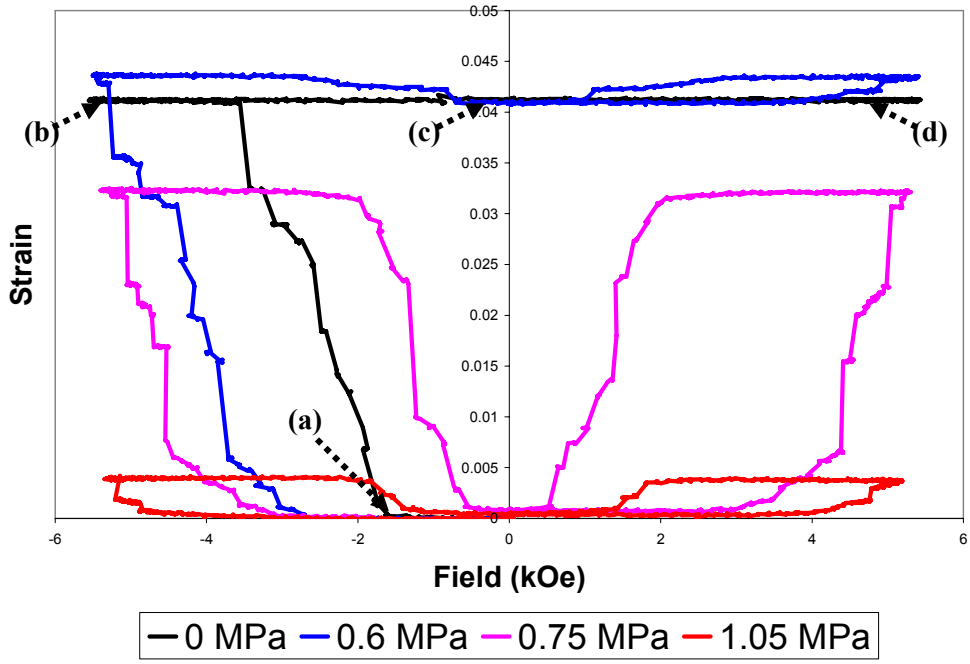

Figure 5-4: Strain as a function of magnetic field under different constant external stress for sample TL9-1A. No piezo assistance is applied.

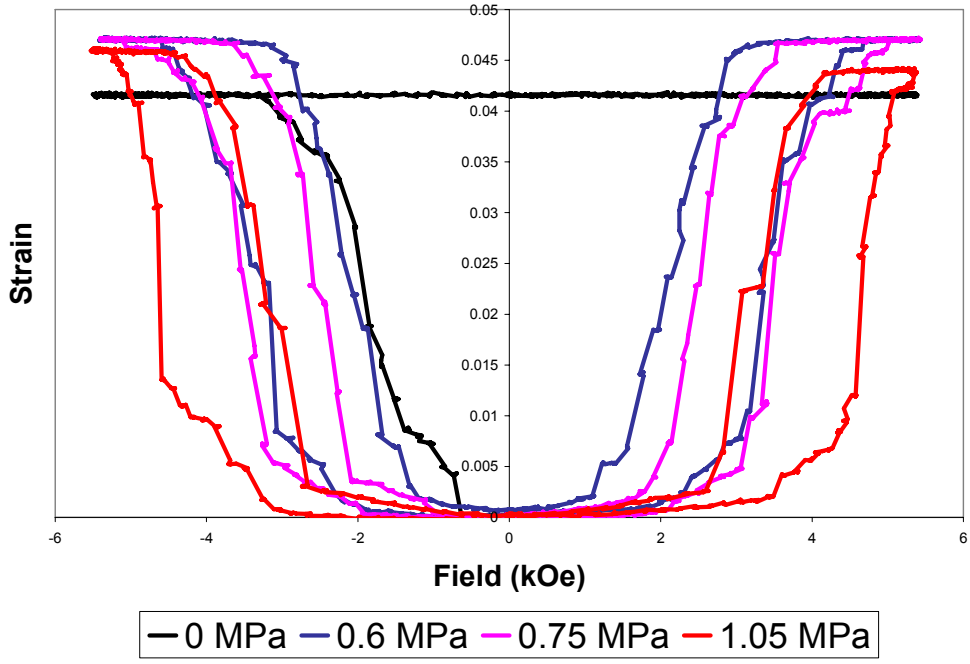

Figure 5-5: Strain as a function of magnetic field under different constant external stress for sample TL9-1A. 40 Vp-p and 7 kHz of piezo-assist actuation is applied during measurement.

Plots of the maximum one-way strain and reversible strain as a function of a constant bias stress are shown in Figure 5-6 and Figure 5-7 respectively. Both figures clearly show that the piezo assistance increases the strain outputs of FSMA actuation. In Figure 5-6, without piezo assist, the maximum *one-way* strain begins to drop for $\sigma_{ext} \geq$ 0.6 MPa and is negligible for $\sigma_{ext} \geq 1$ MPa. With piezo assist the strain begins to drop for $\sigma_{ext} \geq 1.1$ MPa and is negligible only for $\sigma_{ext} \geq 1.5$ MPa.

As shown in Figure 5-7, the maximum *reversible* strain from this sample without piezo assist is 0.033, occurring when the external stress is 0.75 MPa. The operating-stress range with a substantial strain is in between 0.6 and 1 MPa. For the operating stress below 0.6 MPa, the external stress is too low to reset the sample; above 1 MPa, the magnetic stress is too small to induce strain. With application of piezo assist, the possible operating range of stress output extends from 0.3 to around 1.5 MPa. The full reversible strain is achievable from 0.4 to 1.05 MPa. Beyond 1.05 MPa, the strain decreases with external stress and drops to zero at 1.7 MPa. The expansion of the operating range to higher external stresses indicates that the piezo assist significantly increases the efficiency of FSMA devices in delivering mechanical energy, $\sigma_{out}\varepsilon_{out}$.

These results illustrate that the benefits of piezo assist consist not only of a reduced twinning stress and lower threshold field, but also of generating higher stress output for FSMA actuation. Presumably, with the extra acoustic energy from piezo assist, a greater fraction of the magnetic energy input can be used to contribute to twin boundary motion against larger blocking stress. Similarly, in the resetting process when the field is decreasing, a constant external stress can begin and complete resetting the sample more easily at higher field.

Consequently, with piezo assist, the twin boundary motion induced either magnetically or mechanically takes place at lower threshold field and reset occurs more easily (at higher field); hence, a significant reduction in the hysteresis during cyclic actuation can evidently be observed. The hysteresis behavior signifies a reduction in energy loss during the cyclic actuation process. Obviously, the energy loss is due to the necessity to overcome the defect-pinning barriers for twin motion. The defect barriers

are reduced by piezo assist actuation, so the energy loss also decreases with the piezo assist.

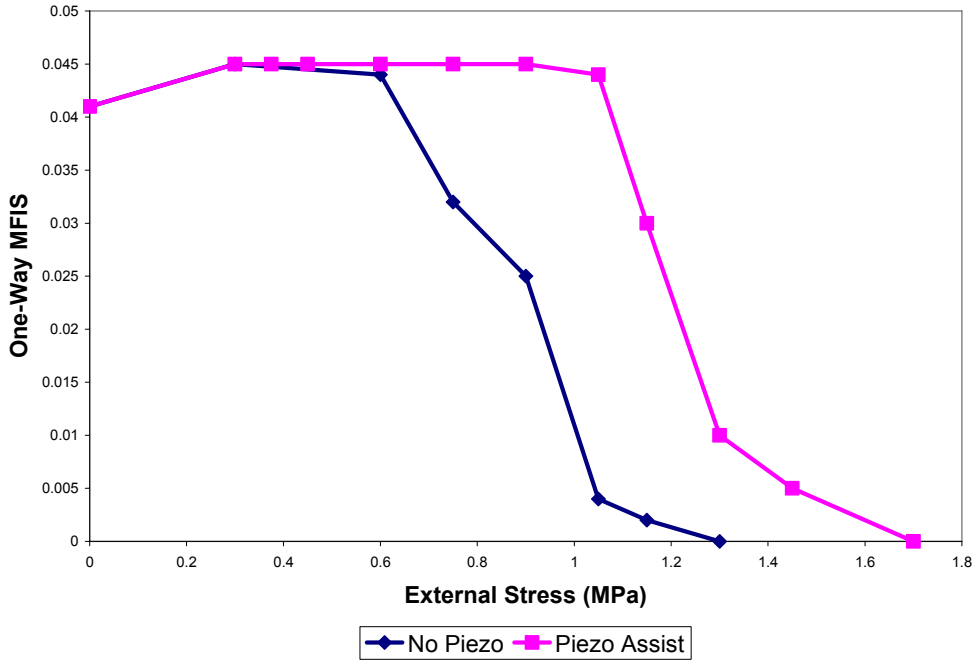

Figure 5-6: Maximum magnetic-field induced strain as a function of a constant bias stress. The two plots show comparison of the piezo effect on the strain output.

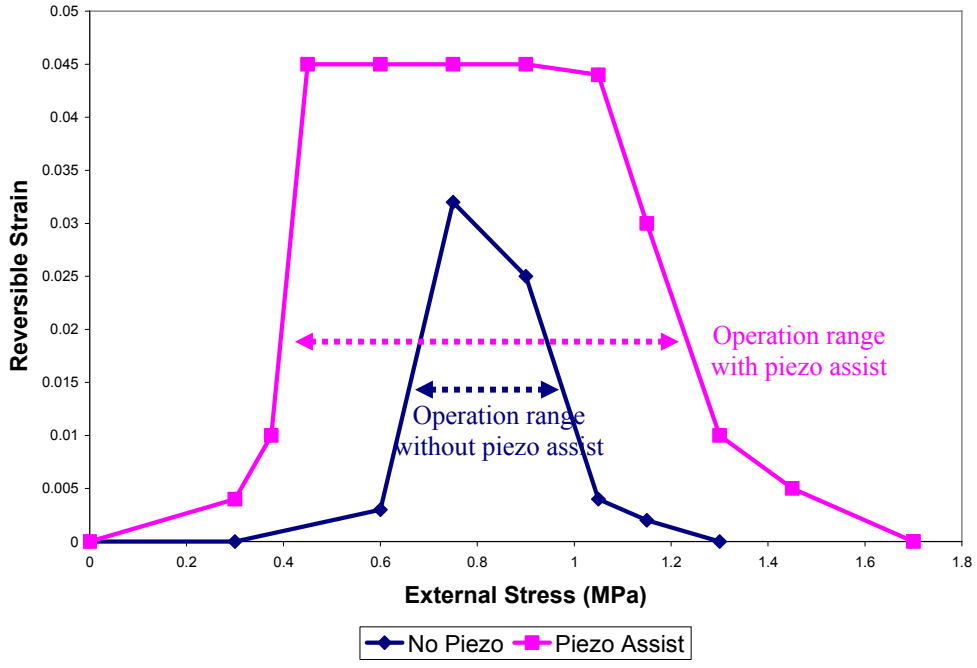

Figure 5-7: Reversible strain as a function of a constant external stress with and without piezoelectric assist.

5.3 Magneto-Stress Results and Model

The relationship between the magnetic energy applied to an FSMA and its stress output is of interest in this section. From the measurement of stress-biased field-induced strain, the applied field induces twin boundary motion inside an FSMA sample to do work against the opposing external stress and σ_{tw}. Alternatively, the external stress may be considered as a measure of the stress output generated by the actuation of the FSMA under applied field.

The plots of the external stress as a function of the applied field at which 2% MFIS is attained are shown in Figure 5-8. The plots indicate the magnitude of the field required to induce 2% strain for given constant stress. Because some of the magnetic energy is needed for overcoming defect barriers to twin boundary motion, a minimum magnetic field of about 2.5 kOe is required to induce 2% strain when no external stress is applied in the absence of piezo assist. With piezo assistance, the minimum-required field is reduced to 1.9 kOe. Then, for higher stress output, a larger field is required for 2% strain. Piezo-assisted actuation reduces the field required to achieve a given strain and stress output. For example, without piezo assist, a 5.1-kOe field is required for generating a 2% strain with 0.9-MPa stress output. With piezo assist, a 4.4-kOe field is required to achieve similar strain and stress output. The magnitude of an increase in the stress output of the piezo-assist FSMA actuation appears to be constant at 0.3 MPa for any given field. The slope of both plots with and without piezo seems to be relatively the same.

The maximum energy density of FSMA crystals is expected to be equal to K_u, which is approximately 160 kJ/m^3. Without piezo assist, the setup of FSMA actuation in this work provides a maximum energy density output of approximately 26 kJ/m^3 (at 3.3% strain and 0.8-MPa stress output), which is equivalent to 16% energy efficiency. With piezo assist, the maximum energy density output from this actuation becomes 47 kJ/m^3 (at 4.5% strain and 1.05-MPa stress output), which is 29% energy efficiency. The energy efficiency of this experimental setup improves by 80% with piezo assistance.

The free-energy model is discussed here to explain the relationship between the magnetic energy and its equivalent mechanical stress output. As we have shown, the driving force for MFIS in an FSMA is the difference in magnetic free energies for twin variants with perpendicular magnetic easy axis direction during the magnetization process. The large free-energy difference arises from high magnetic anisotropy. The maximum driving force is also limited by the anisotropy energy. From the free energy model including only Zeeman energy and anisotropy energy, the magnetic driving energy density F_{mag} may be derived from the derivative of the free energy expression (Equation 3-1) as:

$$F_{mag} = -\frac{\partial g}{\partial f_1} = 2K_u h\left(1-\frac{h}{2}\right),$$
$$h = \cos\theta = \frac{H}{H_a}, \quad H_a = \frac{2K_u}{\mu_o M_s},$$

Equation 5- 3.

The standard definition of the reduced field, $h = \cos\theta$ (the cosine of the magnetization angle in the unfavorable variant, Figure 3-7), is used in here. The value of h is equal to one for $H \geq H_a$; therefore, the maximum magnetic driving energy density F_{mag} can never exceed K_u even at very high very field. It should be noted that the demagnetization effect is not yet considered in Equation 5-3.

The magnetic driving energy density is then equated to the mechanical force, $\sigma\varepsilon_o$, to obtain a magneto-stress relationship, where the ε_o is a martensitic strain $(1 - c/a)$. The field H is replaced by $H_{ext} - H_{2\%}$, where H_{ext} is the external applied field and $H_{2\%}$ the field at which 2% MFIS is achieved under zero bias stress (~ 2.5 kOe). In this way, we consider only the part of the field used in generating strain output. The magnetic stress as a function of applied field (Model 1) is then plotted in comparison with the empirical data (without piezo assistance), shown in Figure 5-9. From the figure, in both empirical data and model calculation, the magnetic stress is sub-linearly proportional to the applied field. However, the magnetic stress calculated from the model appears to be larger than the empirical one without piezo assist for any given field. The model seems to overestimate the magnetic stress value. The demagnetization effect might be responsible for the deviation. The demagnetization effect is then considered for calculating the

magnetic driving force, based on the discussion in Section 3.2. The magnetic driving energy density F_{mag} and the reduced field $\tilde{h}$ may be rewritten as:

$$F_{mag} = -\frac{\partial g}{\partial f_1} = 2K_u \tilde{h}\left(1 - \frac{\tilde{h}}{2}\right),$$
$$\tilde{h} = \cos\theta = \frac{H}{H_a}, \quad H_a = \frac{2\left(K_u + \mu_o N_d M_s^2\right)}{\mu_o M_s},$$

Equation 5-4.

The source of the magnetic driving force for twin motion is mainly governed by the magnetocrystalline anisotropy K_u. However, $\tilde{h}$, which is proportional to the magnetization angle, is a function of both K_u and the demagnetizing factor, N_d. The magnetization rotation becomes more difficult with both the magnetocrystalline anisotropy and shape anisotropy inhibiting the rotation process; $\tilde{h}$ is smaller than h for a given H value. By using the same values of the demagnetization factor (N_d = 0.18, M_s = 484 kA/m) as used in Section 3.3, the stress output is plotted against the magnetic field in Figure 5-9 (Model 2). The magnetic stress calculated from the model including demagnetization appears to be closer to the empirical data (without piezo assist) as opposed to the magnetic stress from the free energy model without the demagnetization considered. The demagnetization effect works against the magnetization rotation process and reduces the effective $\tilde{h}$ for a given applied field; the reduction results in a lower magnetic stress output for a given applied field. It is unclear at this point what additional factors may be responsible for the difference between the data and Model 2 in Figure 5-9.

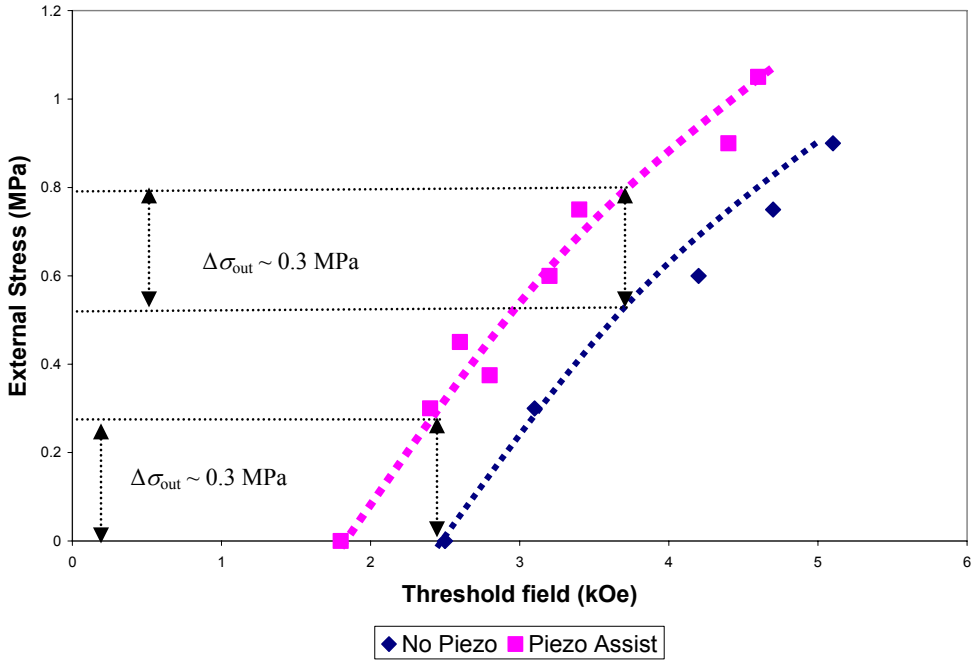

Figure 5-8: Plots of an applied external stress-vs-threshold field for a cyclic actuation at 0.01 Hz. The threshold field is defined to be the field at which a 2% strain is attained. The external stress is an applied compressive stress blocking the field-induced actuation. Two results are plotted in the graph: with and without piezo-assist actuation.

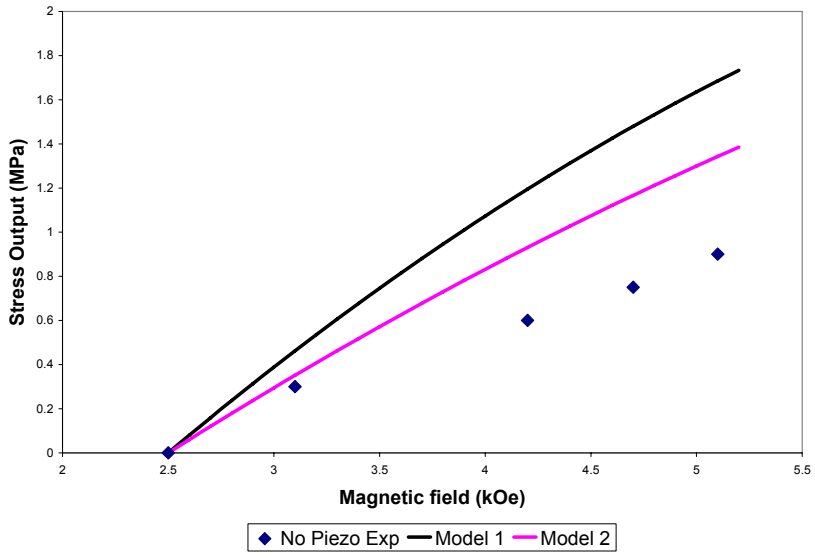

Figure 5-9: Stress output as a function of applied field. "No Piezo Exp" plot is from the experimental data without piezo assist. Model 1 is from a simple free energy model including Zeeman and Anisotropy energy (Equation 5-3). Model 2 is based on the free energy model in Model 1 with the demagnetization effect consideration.

CHAPTER 6

SUMMARY, CONCLUSIONS AND FUTURE WORK

6.1 Summary

Ni–Mn–Ga based FSMAs have been established as a promising class of active materials with strains much larger than piezoelectric or magnetostrictive actuators. However, FSMAs still have several characteristic shortcomings that may limit their potential applications. To address their limitations, this work is focused on two major areas: (1) reducing the threshold field for FSMA actuation and (2) increasing the stress output from the actuator while maintaining a large strain output. This thesis demonstrates the beneficial effects on the threshold field of adding a high-frequency, low-amplitude acoustic assist during FSMA actuation. Three different experimental apparatuses were designed and built to study the magnetic, mechanical and magneto-mechanical responses of the Ni–Mn–Ga single crystals. The magnetic-response study provides insights into the demagnetization and piezo-assisted effects on the threshold field. The mechanical-response measurement shows the piezo-assisted effect on the twinning-yield stress. Finally, the magneto-mechanical response measurement allows the study of the dependence of stress and strain outputs of cyclic FSMA actuations on both the demagnetization and piezo-assisted effects.

To study the demagnetization effect, MFIS was measured for the Ni-Mn-Ga single crystal samples (TL8-1A and TL8-3C), which have similar compositions and

dimensions. These measurements were done under two different orientations of an applied field: (1) parallel and (2) transverse to the long sample dimension. Demagnetization theory dictates that the magnetization proceeds more easily under a longitudinal field than a transverse field. All of our empirical observations are consistent with this theory. For sample TL8-1A, under a longitudinal field, MFIS increases abruptly to full strain once the threshold field of 1 kOe is achieved. On the other hand, MFIS starts to show up after the threshold field of 1 kOe is reached and, then, slowly increases with the transverse field and only reaches maximum at the field of 3.5 kOe. For sample TL8-3C, under a longitudinal field, the threshold field to initiate twin boundary motion is 1.7 kOe and a full MFIS completes abruptly at a similar field of 1.7 kOe. Under a transverse field, the initial threshold field is 2.4 kOe and it requires a large field of 3.5 kOe to achieve a full strain.

The piezoelectric assist decreases the threshold field by facilitating twin boundary motion. However, the piezo assist does not have any influence on the demagnetization effect. With the piezo-assist, MFIS begins to grow at an onset threshold field of approximately 0.5 kOe and 1 kOe for sample TL8-1A and TL8-3C, respectively. Under a longitudinal field, MFIS abruptly increases to full strain at a similar field for both samples. However, under a transverse field, a field of approximately 3.3 kOe is still required to achieve the full MFIS for both samples, even though the initial threshold field is reduced by 0.5 and 1 kOe for sample TL8-1A and TL8-3C respectively.

A simple phenomenological free-energy model, considering Zeeman energy, magnetocrystalline anisotropy and an approximate form to express the demagnetizing field, is used to explain the demagnetization effect on the MFIS of a defect-free FSMA sample consisting of two twin-variant types with perpendicular *c* axes. The demagnetizing factor N_d is assumed to be linearly dependent on the volume fraction of the two twin variants in the FSMA sample. The model predicts that, when N_d is equal to 0.35, MFIS initially increases linearly with increasing magnetic field and a full MFIS can be achieved at the effective anisotropy field H_a. When N_d is below 0.35, a full MFIS can be obtained at lower field. On the other hand, when N_d is above 0.35, a full MFIS may never be completely achieved even at the field equal or above H_a.

From [41], a demagnetizing factor N_d, for a prolate ellipsoid with a length-to-width ratio of 4 and a field applied along the width direction, is approximately 0.4; N_d for a field applied along the length direction of an ellipsoid-shape with a similar aspect ratio is 0.1. For the dimensions of the samples used in this work (length-to-width ratio of 4), the model estimates N_d to be 0.18 and 0.05 for the longitudinal and transverse field accordingly. As a result, a full MFIS can be achieved in both samples at the field lower than H_a; however, a larger field is required for a full MFIS for a transverse field due to the higher demagnetizing factor. The values of N_d calculated from our data for the FSMA samples are about half of the corresponding magnitudes of the ellipsoid-shape samples. In an ellipsoid, the magnetization field is uniform and, hence, a strong demagnetizing field is expected to be present uniformly throughout the sample. However, for a magnetized sample that is not an ellipsoid, N_d is not uniform and can only be approximated by volume-averaged fields. The demagnetizing factor of a non-ellipsoidal FSMA sample is even more complicated because the variant rearrangement further modifies the demagnetizing field. Therefore, in reality, the dependence of N_d on the variant rearrangement is complex and strongly non-linear.

The piezo-assist effect on MFIS, under varying piezo drive frequencies and voltages, on not only the threshold field but also on twinning-yield stress was studied for samples TL8-1A and TL9-1A. A longitudinal piezo actuation was applied to FSMA samples from a 33-mode piezo stack to assist twin boundary motion. The piezo-assist effect was known to enhance field-induced twin boundary motion [37]. But how it facilitated twin boundary motion was not understood and the piezo-assist effect on the mechanical twinning-yield stress had not been measured. In this work, the reductions of the threshold field H_{th} and the twinning-yield stress σ_{tw} of the Ni–Mn–Ga single crystal by an application of acoustic waves generated by a piezo stack were studied quantitatively. As has been reported by [37], we observe the degree of the piezo-assist effect on good samples (low H_{th} and σ_{tw}) to be smaller than that on inferior ones (high H_{th} and σ_{tw}). For sample TL8-1A with lower H_{th} and σ_{tw}, the maximum reductions of H_{th} and σ_{tw} are 0.5 kOe and 0.23 MPa, respectively. For sample TL9-1A with higher H_{th} and

σ_{tw}, the corresponding values are 1 kOe and 0.45 MPa. The piezo assist is exploited more effectively in inferior samples. At large defect strength and/or concentration, the piezo assist helps to overcome the defect barrier to a large extent, which results in large reduction in H_{th} and σ_{tw}. For superior samples with low defect concentration, there are fewer and/or weaker defects for the piezo assist to neutralize; therefore, small reductions in H_{th} and σ_{tw} are obtained.

For the 10 $V_{p\text{-}p}$ piezo assist, the maximum twinning-stress reduction is smaller than the reduction resulting from higher $V_{p\text{-}p}$ piezo assist. For both sample TL8-1A and TL9-1A, the maximum reduction in both H_{th} and σ_{tw} appears in the frequency range between 1 – 5 kHz. For piezo drive frequencies above 5 kHz, H_{th} and σ_{tw} do not decrease further with increasing piezo frequency and remain relatively constant at their minimum values.

The reduction in both threshold field and the twinning stress implies that the piezo transmits a stress wave into the sample to facilitate twin motion. The theory of stress waves in solid media and FEM analysis were discussed to estimate the stress wave magnitudes from the piezo assist. The key assumption, used in both analyses, is that longitudinal stress waves propagate in an elastic and isotropic solid media. The stress-wave theory dictates that the magnitude of the stress waves generated from the piezo actuation is proportional to the product of piezo drive frequency and amplitude. The calculated amplitude of the stress waves for piezo drive frequency of 5 kHz and amplitude of 3.5 micron is 2.5 MPa from FEM analysis and 1.5 MPa from the stress-wave theory. Even though different, both values are of the same order of magnitude. These comparable results indirectly show that, for an operating piezo actuation with amplitude of 1 – 7 microns and frequency of 0 – 7 kHz, the expected magnitude of the acoustic-assistance *elastic* stress in *isotropic* solids should be in the order of 0 – 2 MPa.

From the calculation, the stress magnitude provided by the piezo stack driven at 50 $V_{p\text{-}p}$ and 2 kHz is actually as high as 1.2 MPa; while, the maximum reduction of twinning stress observed in sample TL9-1A is only 0.4 MPa and 0.25 MPa for sample TL8-1A. The stress-wave theory estimates the maximum possible stress magnitude by assuming that the FSMA sample is perfectly elastic and isotropic and the transmission of

the stress wave from piezo stack to the FSMA sample is free of any loss or reflection. In reality, the FSMA sample is strongly anisotropic with a tetragonal martensitic phase and also responds plastically with twin boundary motion. Therefore, the stress waves may be dispersed or reflected at the twin boundary regions significantly reducing their magnitude; hence, the actual stress generated in the FSMA by the piezo could be much less than the calculated values. This stress wave analysis actually gives us insight into the magnitude of the piezo assist effect on the FSMA actuation in the form of calculated stress. The calculated stress magnitude is in fairly good agreement with the empirical twinning-stress reduction for lower drive amplitude and frequency. For 30 $V_{p\text{-}p}$ drive at 2 kHz, the calculated stress wave is 0.5 MPa, while the stress reduction in both samples TL8 and TL9 are 0.25 and 0.3 MPa correspondingly.

Even though the empirical stress reduction is not expected to be as large as the calculated stress, one would expect that the piezo assist should continue decreasing the twinning stress or the threshold field, as the piezo drive frequency increases, because the stress amplitude by piezo was derived to be linearly proportional to the piezo drive frequency. However, the data show that the piezo effect becomes insignificant beyond a frequency in the range between 1 and 5 kHz. The absence of an increase in piezo effect at frequencies above 5 kHz may be explained by a degraded output displacement of the piezo at high frequency. The displacement of the piezo stack actuation decreases with increasing frequency above approximately 2 kHz. Using the piezo displacement as a function of frequency, the elastic stress wave amplitude can be estimated. For frequencies below 2 kHz, the stress wave amplitude increases linearly with increasing frequency. For 2 – 5 kHz, the stress amplitude appears roughly constant. Above 5 kHz, the calculated stress wave decreases with increasing frequency (Figure 4-16).

The other possible reason that the acoustic assist cannot reduce the twinning stress and threshold field completely to zero may be due to the sinusoidal form of the piezo actuation. The piezo actuation is driven by a sinusoidal $V_{p\text{-}p}$ function, so the tensile and compressive waves are equally generated inside the samples. As a result, the piezo assistance in this case should be thought of as a signal superimposed on the quasi-static magnetic or mechanical stress. These local vibrations impart additional energy to the

twin boundaries and, as a result, the twinning stress decreases, because the energy required to overcome the barriers is reduced. However, they do not provide *work* to cause twin boundary motion unless external work is applied. Unless external compressive stress is applied on a FSMA sample, a sinusoidal acoustic actuation produces no net work and, hence, cannot move a twin boundary by itself.

The FEM analysis shows that the first resonant frequency of the bending mode of a body having similar elastic modulus, density and geometrical dimensions to the FSMA samples used in this work, is in the range of 3 – 4 kHz, which is in the frequency region over which acoustic energy enhances MFIS. Consequently, a 15-mode shear piezo stack was used in place of a 33-mode piezo stack in order to generate transverse waves to the FSMA sample. This shear-mode setup allows a direct observation of the acoustic assist possible by a resonant bending mode. However, the results show no resonant characteristic of σ_{tw} reduction in the aforementioned frequency range. The maximum twinning stress reduction is only 0.05 MPa, only one-tenth of the corresponding value achieved by the longitudinal piezo assist.

Thus, it is more likely that the stress responsible for twin boundary motion is the resolved shear stress across twin boundary planes due to longitudinal waves. Transformation equations for plane stress show that, for uniaxial or biaxial stress, the planes of maximum shear stress occur at at $\theta = 45^{o}$; for pure shear, the maximum shear stresses occur at at $\theta = 0^{o}$ and the shear stresses become zero at at $\theta = 45^{o}$. Longitudinal stress waves impart uniaxial tensile/compressive stresses into the sample normal to the base of the sample. Therefore, the longitudinal piezo assist appears to be more effective to facilitate twin boundary motion than the transverse one, specifically for the FSMA sample with twin boundary planes oriented 45^{o} to the base of the crystal.

The magneto-mechanical response of cyclic FSMA actuation of sample TL9-1A, driven at 0.01 Hz, was studied with and without piezo assist. Only a 33-mode longitudinal piezo stack was used for piezo assistance in this case. The threshold field required for deforming the crystal is clearly reduced by the piezo-assistance. Both the operating stress and the strain outputs of the FSMA actuation are clearly enhanced by the

piezo-assist effect. Without the piezo-assistance, the maximum reversible strain of the FSMA actuation is 3% and appears only over the limited stress range between 0.7 and 0.8 MPa. With the piezo-assistance, the maximum reversible strain increases to 4.5% and appears in a broader range of stress output between 0.4 and 1.05 MPa (Figure 5-7). The magnitude of an increase in the stress output due to the piezo-assisted FSMA actuation appears to be constant at 0.3 MPa for any given field (Figure 5-8). The reduction in the twinning-yield stress due to the acoustic-assistance obviously improves the FSMA cyclic actuation performance; the unused magnetic energy can potentially be utilized to work against a larger external stress.

The desirable condition for high strain and stress output from FSMA actuation is to obtain an FSMA material with a large K_u and low σ_{tw}. However, a large K_u will require the application of a large magnetic field, which consequently requires large electromagnet coils. Therefore, the other alternative method to achieve a full reversible strain for given stress, at relatively low magnetic field, is to reduce σ_{tw}.

Three potential methods may be exploited to reduce σ_{tw} of FSMA crystals. First, minimizing impurity concentration is one possible method to obtain low-σ_{tw} FSMA; however, to date, it is not yet known how to control systematically the concentration of those impurities that most strongly impede twin boundary motion. Crystal-growth processes to improve the quality and purity of FSMA crystals are still under development by Ames Laboratory. Second, σ_{tw} may be reduced by operating the FSMA actuation at elevated temperature, as the thermally-activated process of twin boundary motion is enhanced at higher temperature. However, the magnetic anisotropy of a tetragonal martensitic Ni–Mn–Ga sample also decreases with increasing temperature. As a result, the maximum magnetic driving force, limited by K_u, is diminished at higher temperature. Finally, as shown in this work, the stress and strain output of low-quality FSMA samples can be significantly improved with the use of the piezo assist. The piezo assist reduces σ_{tw} without affecting the magnetic stress from K_u. A smaller fraction of the magnetic energy is needed to overcome σ_{tw} and the unused energy can be utilized to work against the external load.

The free-energy model has been discussed to explain the relationship between the magnetic energy and its equivalent mechanical stress output. The magnetic driving energy density or magnetic stress is first calculated from the free-energy model without considering the demagnetizing effect. From both empirical data and the model calculations, the magnetic stress is sub-linearly proportional to the applied field. However, the magnetic stress calculated from the free-energy model appears to be larger than the empirical one without piezo assist for any given field. The demagnetizing effect was then considered for calculating the magnetic driving energy density. The magnetic stress calculated from the model including the demagnetizing effect appears to be closer to the empirical data (without piezo assist) as opposed to the magnetic stress from the free energy model without the demagnetizing effect considered. The demagnetizing effect likely impedesthe magnetization rotation process and reduces the internal field for a given applied field; the reduced internal field results in a lower magnetic stress output for a given applied field.

6.2 Conclusions

The demagnetizing field due to the field generated by surface poles in a magnetic sample strongly dictates the maximum applied field needed for a full MFIS. The demagnetizing field decreases the effective internal field inside the FSMA sample; as a result, for a given external field, the magnetic driving force is reduced by the demagnetizing field. For a small demagnetizing factor (longitudinal field), a full MFIS can be achieved at an external field as low as 0.5 kOe. However, for a high demagnetizing factor (a transverse field), a full MFIS can be achieved at the required external field as high as 3.5 kOe. The extra required field of 3 kOe significantly increase the size of the FSMA actuator. Therefore, it is important in the design that the dimensions of the FSMA samples are optimally designed to minimize the demagnetization effect.

The piezo assist on FSMA actuation can be understood as a form of an extra, bipolar stress wave that, coupled with a lower-frequency drive stress or magnetic field,

facilitates twin boundary motion. For a given drive frequency and amplitude, the stress-wave theory provides an estimate of the expected stress-wave magnitude from piezo actuation. However, the actual stress waves generated in the FSMA are still limited by the inelastic and anisotropic nature of the FSMA sample. Moreover, the stress amplitude generated by the piezo is maximum at the piezo-attached end of the sample and decreases to zero at the free end to satisfy the boundary conditions. Therefore, the actual stress-wave magnitude is lower than the magnitude estimated from the stress-wave theory.

The effectiveness of the piezo assistance in enhancing twin boundary motion increases with increasing drive frequency up to a limiting frequency of 2 – 5 kHz. Above 2 kHz, the piezo displacement decreases with increasing frequency; as a result, the amplitude of the stress waves remains constant with increasing frequency and begins to decrease at frequencies above 7 kHz.

The piezo actuation, driven by a sinusoidal $V_{p\text{-}p}$ function, generates both tensile and compressive waves of equal magnitude inside the FSMA samples. These vibrations do impart additional energy and, as a result, the twinning stress decreases, because the low-frequency (magnetic or mechanical) drive energy required to overcome the barriers is reduced. However, acoustic waves do no net *work* to cause twin boundary motion unless an external bias field or stress is applied.

For FSMA samples with twin planes oriented 45^{o} to the base of the crystals, the longitudinal stress waves are the most effective type to facilitate twin boundary motion. Longitudinal stress waves impart uniaxial tensile/compressive stresses to the sample normal to the base of the sample, which result in the maximum shear stresses along the 45^{o} twin planes. On the contrary, transverse stress waves are the least effective type, because the resulting shear stresses along the twin planes are equal to zero.

For cyclic actuation, the stress and strain output can be significantly improved with the piezo assist. The reduction in the twinning-yield stress due to the acoustic-assistance obviously improves the FSMA cyclic actuation performance; the unused magnetic energy can be utilized to work against a larger external stress.

The magnetic stress, calculated from the free-energy model, appears to be larger than the empirical one without piezo assist for any given field. The demagnetization

effect is shown to be responsible for much of the deviation. The demagnetization effect requires that a larger external field be applied to achieve magnetization rotation.

6.3 Future Work

6.3.1 Minimal-Demagnetization FSMA Actuator

The demagnetizing effect strongly dictates the maximum field required to achieve a full MFIS and also affects the stress output of the cyclic actuation. It is important that the dimensions of the FSMA single crystals are optimally designed to minimize the demagnetizing effect; as a result, a full MFIS and large stress output can be obtained at smaller field than in crystals of other dimensions. This optimized-dimension design is expected to indicate that the field be applied normal to a small-area face of the crystal, and/or that the crystal dimension parallel to the field be large. However, there is a limit beyond which this long crystal length parallel to the field will increase the reluctance of the magnetic drive circuit and require excessive drive current. Thus, the crystal dimension must be optimized together with the magnetic drive.

6.3.2 Relationship between Demagnetizing Factor and FSMA Variant Structure

The demagnetizing factor is strongly dependent on the evolution of the variant rearrangement of the FSMA samples. In this work, the phenomenological model, used to explain the demagnetizing effect, assumes a linear relationship between the demagnetization factor and the variant volume fraction. In reality, the relationship is quite complex and highly non-linear. To improve the model to better explain the empirical observation, an analytical or numerical treatment of the demagnetization factor as a function of the variant-rearrangement structure is required. A technique such as the finite-element method might be useful to calculate the actual demagnetization factor and predict the MFIS as a function of the magnetic field more precisely. If an optimal twin

structure (twin boundary density) for low magnetostatic energy could be determined, it may be possible to train and process crystals to better meet this standard.

6.3.3 Plastic Stress Waves Consideration

In this work, the stress-wave theory considers elastic stress waves traveling inside isotropic media. The stress-wave theory estimates the magnitudes of the stress waves from piezo assist for given frequency and amplitude in an isotropic-elastic solid. However, the stress waves in FSMA become plastic once the stress magnitude is higher than the twinning-yield stress. To better estimate the actual stress wave magnitudes expected from the piezo-assisted actuation, the stress waves need to be considerer under plastic conditions. In this case, the stress-strain relationship becomes nonlinear and possibly strain-rate dependent; as a result, a visco-plastic response might be expected. The plasticity consideration requires more complex mathematical methods than the wave equation considered in this work.

6.3.4 Acoustic Stress-Pulse Assisting MFIS

The sinusoidal stress waves used in this study continuously impart both tensile and compressive waves to FSMA samples. In practice, FSMA actuators are typically extended in one direction transverse to the magnetic field and then compressively reset by the mechanical stress. Therefore, it should be more effective to apply an acoustic stress wave that is pre-shaped with different rise time and fall time such that the tensile stress is greater than the compressive stress as the magnitude of the field increases (and vice versa as the magnitude of the field decreases). For example, tensile acoustic pulses should be applied during the crystal extension, and compressive acoustic pulses should be applied during resetting the crystal. In this way, the piezo-assisted effect can be optimally utilized.[3]

[3] Note, the acoustic signal must be applied normal to crystal faces that do not deform under twin boundary motion. Therefore, they must be applied along the extension axis.

6.3.5 High-Purity Ni–Mn–Ga Single Crystal

For low-quality FSMA (high twinning stress), a significant fraction of the magnetic energy is used to overcome twining stress; the rest is used for working against external load. As discussed in this work, to maximize the stress and strain output of FSMA actuators, the twinning stress should be minimized. Therefore, a high-purity FSMA single crystal with low defect concentration is critical for reaching the highest performance levels in FSMA actuators.

BIBLIOGRAPHY

1. Ullakko, K. *Large stroke and high-strength actuator materials for adaptive structures*. in *Proceeding of SPIE*. 1996.
2. Ullakko, K., P.G. Yakovenko, and V.G. Gavriljuk. *New developments in actuator materials as reflected in magnetically controlled shape memory alloys and high-strength shape memory steels*. in *Proceeding of SPIE*. 1996.
3. James, R.D. and M. Wuttig. *Alternative smart materials*. in *SPIE*. 1996.
4. Ullakko, K., et al., *Large magnetic-field-induced strains in Ni2MnGa single crystals.* Applied Physics Letters, 1996. **69**(13): p. 1966-1968.
5. Ullakko, K., et al., *Magnetically controlled shape memory effect in Ni2MnGa intermetallics.* Scripta Materialia, 1997. **36**(10): p. 1133-1138.
6. Wu, G.H., et al., *Giant magnetic-field-induced strains in Heusler alloy NiMnGa with modified composition.* Applied Physics Letters, 1999. **75**(19): p. 2990-2992.
7. James, R.D., R. Tickle, and M. Wuttig, *Large field-induced strains in ferromagnetic shape memory materials.* Mat. Sci. Eng. A, 1999. **273-275**: p. 320-325.
8. Tickle, R. and R.D. James, *Magnetic and magnetomechanical properties of Ni2MnGa.* Journal of Magnetism and Magnetic Materials, 1999. **195**(3): p. 627-638.
9. Murray, S.J., et al., *6% magnetic-field-induced strain by twin-boundary motion in ferromagnetic Ni-Mn-Ga.* Applied Physics Letters, 2000. **77**(6): p. 886-888.
10. Murray, S.J., et al., *Giant magnetic-field-induced strain in Ni-Mn-Ga crystals: Experimental results and modeling.* Journal of Magnetism and Magnetic Materials, 2001. **226**: p. 945-947.

11. Henry, C., *Dynamic actuation properties of Ni-Mn-Ga ferromagnetic shape memory alloys*. 2002, Massachusetts Institute of Technology: Cambridge MA.
12. Sozinov, A., et al., *Giant magnetic-field-induced strain in NiMnGa seven-layered martensitic phase.* Applied Physics Letters, 2002. **80**(10): p. 1746-1748.
13. Marioni, M.A., R.C. O'Handley, and S.M. Allen, *Pulsed magnetic field-induced actuation of Ni-Mn-Ga single crystals.* Applied Physics Letters, 2003. **83**(19): p. 3966-3968.
14. Webster, P.J., *Heusler Alloys.* Contemp. Phys., 1969. **10**: p. 559-577.
15. O'Handley, R.C. and S.M. Allen, *Chemical order/disorder and field-induced twin rearrangement in Ni-Mn-Ga ferromagnetic shape memory alloys*, in *Unpublished proposal to NSF*. 2004, Massachusetts Institute of Technology: Cambridge, MA.
16. Marioni, M., *Pulsed magnetic field-induced twin boundary motion in Ni-Mn-Ga*. 2003, Massachusetts Institute of Technology: Cambridge, MA.
17. O'Handley, R.C., et al., *Phenomenology of giant magnetic-field-induced strain in ferromagnetic shape-memory materials (invited).* Journal of Applied Physics, 2000. **87**(9): p. 4712-4717.
18. O'Handley, R.C., *Model for strain and magnetization in magnetic shape-memory alloys.* Journal of Applied Physics, 1998. **83**(6): p. 3263-3270.
19. Murray, S., *Magneto-mechanical properties and applications of Ni-Mn-Ga ferromagnetic shape memory alloy*. 2000, Massachusetts Institute of Technology: Cambridge, MA.
20. Peterson, B.W., et al., *Acoustic assisted, field-induced strain in ferromagnetic shape memory alloys.* Journal of Applied Physics, 2004. **95**(11): p. 6963-6964.
21. James, R.D. and M. Wuttig, *Magnetostriction of martensite.* Philosophical Magazine a-Physics of Condensed Matter Structure Defects and Mechanical Properties, 1998. **77**(5): p. 1273-1299.
22. O'Handley, R.C., et al. *Field-induced strain in ferromagnetic shape memory alloys: from macroscopic to microscopic models*. in *The Fourth Pacific Rim International Conference on Advanced Materials and Processing*. 2001: The Japan Institute of Metals.

23. O'Handley, R.C., et al., *Model for temperature dependence of field-induced strain in ferromagnetic shape memory alloys.* Materials Science and Engineering a-Structural Materials Properties Microstructure and Processing, 2006. **438-440**: p. 445-449.
24. Likhachev, A.A. and K. Ullakko, *Magnetic-field-controlled twin boundaries motion and giant magneto-mechanical effects in Ni-Mn-Ga shape memory alloy.* Physics Letters A, 2000. **275**(1-2): p. 142-151.
25. Likhachev, A.A., A. Sozinov, and K. Ullakko, *Different modeling concepts of magnetic shape memory and their comparison with some experimental results obtained in Ni-Mn-Ga.* Materials Science and Engineering a-Structural Materials Properties Microstructure and Processing, 2004. **378**(1-2): p. 513-518.
26. Likhachev, A.A., A. Sozinov, and K. Ullakko, *Modeling the strain response, magneto-mechanical cycling under the external stress, work output and energy losses in Ni-Mn-Ga.* Mechanics of Materials, 2006. **38**(5-6): p. 551-563.
27. O'Handley, R.C., et al. *Microscopic considerations for models of ferromagnetic shape memory actuation*. in *Proceeding of SPIE*. 2002.
28. Marioni, M.A., S.M. Allen, and R.C. O'Handley, *Nonuniform twin-boundary motion in Ni-Mn-Ga single crystals.* Applied Physics Letters, 2004. **84**(20): p. 4071-4073.
29. Mullner, P. and K. Ullakko, *The force of a magnetic/electric field on a twinning dislocation.* Physica Status Solidi B-Basic Research, 1998. **208**(1): p. R1-R2.
30. Ferreira, P.J. and J.B. Vander Sande, *Magnetic field effects on twin dislocations.* Scripta Materialia, 1999. **41**(2): p. 117-123.
31. Hirth, J.P., in *The Relationship between the structure and mechanical properties of metals*. 1963. p. 217.
32. Richard, M., *Systematic analysis of the crystal structure, chemical ordering, and microstructure of Ni-Mn-Ga ferromagnetic shape memory alloys*. 2005, Massachusetts Institute of Technology: Cambridge, MA.

33. Rajasekhara, S. and P.J. Ferreira, *A dislocation model for the magnetic field induced shape memory effect in Ni2MnGa.* Scripta Materialia, 2005. **53**(7): p. 817-822.
34. Reed-Hill, R.E. and R. Abbaschian, *Physical Metallurgy Principles*. 3rd ed. 1994, Boston: PWS Publishing Company.
35. Hertzberg, R.W., *Deformation and fracture mechanics of engineering materials*. 4th ed. 1996: John Wiley and Sons.
36. Chambers, J., *Design and Characterization of Acoustic Pulse Shape Memory Alloy Actuators*. 2005, Massachusetts Institute of Technology: Cambridge, MA.
37. Peterson, B., *Acoustic Assisted Actuation of Ni-Mn-Ga Ferromagnetic Shape Memory Alloys*. 2006, Massachusetts Institute of Technology: Cambridge, MA.
38. Peterson, B., in *Unpublished thesis proposal*. 2003, Massachusetts Institute of Technology: Cambridge, MA.
39. Chambers, J. *Characterization of piezoelectricly induced actuation of NiMnGa single crystal*. in *Proceedings of SPIE*. March 2005.
40. Simon, J., *Transverse Acoustic Actuation of Ni-Mn-Ga Single Crystals*. 2007, Massachusetts Institute of Technology: Cambridge, MA.
41. O'Handley, R.C., *Modern Magnetic Materials: Principles and Applications*. 2000, New York: John Wiley & Sons, Inc.
42. Lacheisserie, E.T., D. Gignoux, and M. Schlenker, *Magnetism: I - Fundamentals*. 2002: Kluwer Academic Publishers Group MA.
43. Bozorth, R.M., ed. *Ferromagnetism*. 1993, IEEE Press.
44. Schlagel, D.L., et al., *Chemical segregation during bulk single crystal preparation of Ni-Mn-Ga ferromagnetic shape memory alloys.* Journal of Alloys and Compounds, 2000. **312**(1-2): p. 77-85.
45. *Piezoelectric stack technical specifications*, Piezo Systems, Inc. (www.piezo.com): Cambridge, MA.
46. Kiefer, B., et al. *Application of a magnetic SMA constitutive model in the analysis of magnetomechanical boundary value problems*. in *Proceeding of SPIE*. 2006.
47. Kolsky, H., *Stress Waves in Solids*. 1963, New York: Dover Publications.

48. Graff, K.F., *Wave Motion in Elastic Solids*. 1975, New York: Dover Publications, Inc.
49. Tiersten, H.F., *Linear Piezoelectric Plate Vibrations: Element of the Linear Theory of Piezoelectricity and the Vibrations of Piezoelectric Plates*. 1969, New York: Plenum Press.
50. Kaufman, A.A., A.L. Levshin, and K. Larner, *The role of wave propagation in the motion of an elastic body.* European Journal of Physics, 2004. **25**(2): p. 257-268.
51. Hixson, E.L., *Chapter 10: Mechanical Impedance*, in *Harris' Shock and Vibration Handbook*. 2002, McGraw Hill: New York.
52. Uchino, K., *Ferroelectric Devices*. 2000, New York: Marcel Dekker, Inc.
53. Hull, D. and D.J. Bacon, *Introduction to Dislocations*. 1984, New York: Pergamon Press.
54. Bathe, K.-J., *Finite Element Procedures*. 2005, New Delhi: Prentice Hall of India Private Limited.
55. *ADINA Online Manual: ADINA Theory and Modeling Guide, Volume I: ADINA Solids & Structures*. 2005, ADINA R&D, Inc., MA.
56. Gere, J.M., *Mechanics of Materials*. 5th ed. 2001: Brooks/Cole Thomson Learning.
57. Simon, J., J. Kostamo, and R. Techapiesancharoenkij, *Unpublished experimental data report*. 2007, Massachusetts Institute of Technology: Cambridge, MA.
58. Heczko, O. and L. Straka, *Giant magneto-elastic strain - magnetic shape memory effect.* Czechoslovak Journal of Physics, 2004. **54**: p. D611-D614.
59. Heczko, O., *Magnetic shape memory effect and magnetization reversal.* Journal of Magnetism and Magnetic Materials, 2005. **290**: p. 787-794.
60. Straka, L. and O. Heczko, *Reversible 6% strain of Ni-Mn-Ga martensite using opposing exterrical stress in static and variable magnetic fields.* Journal of Magnetism and Magnetic Materials, 2005. **290**: p. 829-831.
61. Straka, L., O. Heczko, and S.P. Hannula, *Temperature dependence of reversible field-induced strain in Ni-Mn-Ga single crystal.* Scripta Materialia, 2006. **54**(8): p. 1497-1500.

62. Dai, L., J. Cui, and M. Wuttig. *Elasticity of austenitic and martensitic NiMnGa*. in *Proceedings of SPIE, Smart Structures and Materials*. 2003.
63. Dai, L.Y., J. Cullen, and M. Wuttig, *Intermartensitic transformation in a NiMnGa alloy.* Journal of Applied Physics, 2004. **95**(11): p. 6957-6959.
64. Heczko, O., et al., *Temperature dependence of magnetic anisotropy in Ni-Mn-Ga alloys exhibiting giant field-induced strain.* Journal of Applied Physics, 2002. **91**(10): p. 8228-8230.
65. Straka, L. and O. Heczko, *Magnetic anisotropy in Ni-Mn-Ga martensites.* Journal of Applied Physics, 2003. **93**(10): p. 8636-8638.